

Mapping Sensorimotor Function and Controlling Upper Limb
Neuroprosthetics with Electrocorticography

by
Matthew S. Fifer

A dissertation submitted to Johns Hopkins University in conformity with the
requirements for the degree of Doctor of Philosophy

Baltimore, Maryland

September, 2015

© 2015 Matthew S. Fifer
All Rights Reserved

Abstract

Electrocorticography (ECoG) occupies a unique intermediate niche between microelectrode recordings of single neurons and recordings of whole brain activity via functional magnetic resonance imaging (fMRI). ECoG's combination of high temporal resolution and wide area coverage make it an ideal modality for both functional brain mapping and brain-machine interface (BMI) for control of prosthetic devices. This thesis demonstrates the utility of ECoG, particularly in high gamma frequencies (70-120 Hz), for passive online mapping of language and motor behaviors, online control of reaching and grasping of an advanced robotic upper limb, and mapping somatosensory digit representations in the postcentral gyrus. The dissertation begins with a brief discussion of the framework for neuroprosthetic control developed by the collaboration between Johns Hopkins and JHU Applied Physics Laboratory (JHU/APL). Second, the methodology behind an online spatial-temporal functional mapping (STFM) system is described. Trial-averaged spatiotemporal maps of high gamma activity were computed during a visual naming and a word reading task. The system output is subsequently shown and compared to stimulation mapping. Third, simultaneous and independent ECoG-based control of reaching and grasping is demonstrated with the Modular Prosthetic Limb (MPL). The STFM system was used to identify channels whose high gamma power significantly and selectively increases during either reaching or grasping. Using this technique, two patients were able to rapidly achieve naturalistic control over simple movements by the MPL. Next, high-density ECoG (hdECoG) was used to

map the cortical responses to mechanical vibration of the fingertips. High gamma responses exhibited a strong yet overlapping somatotopy that was not well replicated in other frequency bands. These responses are strong enough to be detected in single trials and used to classify the finger being stimulated with over 98% accuracy. Finally, the role of ECoG is discussed for functional mapping and BMI applications. ECoG occupies a unique role among neural recording modalities as a tool for functional mapping, but must prove its value relative to stimulation mapping. For BMI, ECoG lags microelectrode arrays but hdECoG may provide a more robust long-term interface with optimal spacing for sampling relevant cortical representations.

Primary Reader: Nathan E. Crone, M.D.

Secondary Reader: Nitish V. Thakor, Ph.D.

Acknowledgements

I would like to offer my sincerest gratitude to my advisor, Dr. Nathan Crone, and my thesis committee members, Dr. Nitish Thakor and Dr. Stan Anderson. Thank you for sharing your world-class expertise with me and for providing me with invaluable support and feedback throughout my Ph.D.

I would like to thank my fellow students and colleagues at Johns Hopkins for the friendship, support, and intellectual camaraderie that made my Ph.D. such a good experience. To members—past and present—of Crone Lab and the BCI Group, thank you for your guidance and input. You have not only profoundly shaped and contributed to this thesis work, but have also made coming to work fun.

To my friends and family, thank you for your support and persistent interest in my work. Thank you for your understanding when my studies kept me away, and thank you for being a source of emotional nourishment during the last leg of my educational journey. You have made the Baltimore area feel like home.

To Allison, Audrey, and Anna: thank you for being the best little sisters that a big brother could ask for. I wish I could have been around more in your last years at home, but I have cherished every single day that I have been able to spend with you. I'm extremely proud of all of you and look forward to watching you continue to grow into the smart, beautiful, amazing women that I have always known you would be.

To Mom and Dad: thank you for enabling me to go to college and for convincing me to pursue a Ph.D. Thank you for never accepting less than my best,

and for understanding when my best just wasn't enough. Thank you for being great sounding boards on all issues and for remaining, somehow, genuinely interested in hearing about my studies. Knowing that I am making you proud has been a constant source of inspiration, not infrequently a lone beacon of encouragement at times when I wondered whether I belonged in the program.

Last, and most importantly, I would like to thank my amazing wife and the love of my life, Erin. You have been a rock throughout all the unpredictable schedules, the ups and downs of the Ph.D. process, the stress of each milestone, and the general uncertainty about our future plans. Thank you for challenging me and loving me; please don't ever stop. I love you so much!

Dedication

I dedicate this thesis to my godparents, Uncle Bill and Aunt Fran. Thank you for helping me to get my start in this field, and for believing in me. I hope that I am making you proud. I would also like to dedicate this thesis to my grandfather, Floyd Ritchie. You have made it possible for two generations of your family to pursue their educations, and thus, their dreams. Thank you for everything that you have done for us and me.

Summary and Organization of Dissertation

In this dissertation, I will describe my efforts to map sensorimotor function and control neuroprosthetics with human electrocorticography. Each of the first four chapters has been developed into a manuscript for publication. The fifth chapter is a summary of my thoughts on the future of electrocorticography for functional mapping and neuroprosthetics, and is meant to conclude the efforts described in this thesis. The five chapters are each described briefly below.

Chapter 1. The approach to ECoG-based neuroprosthetics taken by our team, which includes clinical and engineering teams at Johns Hopkins University and an engineering team at the Johns Hopkins University Applied Physics Laboratory, is discussed. A brief background for the ECoG neuroprosthetics project at the start of the thesis is presented, in addition to preliminary data describing our team's ability to decode movement kinematics from ECoG signals. This chapter also presents a description and a schematic of our system which streams neural and kinematic data, performs neural decoding, and streams movement commands to either a virtual or physical Modular Prosthetic Limb (MPL).

Chapter 2. The design and validation of a system for online ECoG-based spatial-temporal functional mapping (STFM) is described. High gamma amplitude is extracted in real-time from streaming ECoG signals, and the features from each channel are statistically compared to brief periods of rest before each cue. The results of these analyses can be visualized in real-time. This system was found to be

more sensitive and more specific than stimulation mapping via a region of interest approach which estimated functional roles based on classical anatomical boundaries.

Chapter 3. A version of the system described in Chapter 1 is used to provide online ECoG-based control over reaching and grasping of the Modular Prosthetic to two human subjects. The STFM system from Chapter 2 is used to identify channels whose high gamma activity robustly increases during movements and is selective for either reach or grasp. Using these tools, the two subjects are able to rapidly gain *independent* neural control over reaching and grasping of the prosthetic limb.

Chapter 4. A high-density ECoG (hdECoG) array is used to map the cortical representations of mechanical vibration of a human subject's fingertips. A strong somatotopic gradient is seen in the postcentral gyrus between thumb (inferiorly) and little finger (superiorly), especially in the high gamma power. The high gamma power is robust enough to be observed and classified with near perfect accuracy in single trials. Low frequency power and smoothed amplitude exhibit much weaker, and more disordered, somatotopy than the high gamma power.

Chapter 5. The thesis is concluded with a discussion of ECoG's current and likely future place amongst other prominent functional mapping and brain-machine interface tools, including microelectrode arrays, functional magnetic resonance imaging, electroencephalography, and electrocortical stimulation. The future of ECoG for clinical adoption over microelectrode arrays (for brain-machine interface) and electrocortical stimulation (for functional mapping) receive particular attention. Extensions of the three major projects described in Chapters 2-4 are also discussed.

Contents

Abstract	ii
Acknowledgements	iv
Dedication	vi
Summary and Organization of Dissertation	vii
Table of Contents	ix
List of Figures	xiv
List of Tables	xxii
1 Toward electrocorticographic control of a dexterous upper limb prosthesis: building brain-machine interfaces	1
1.1 Abstract	1
1.2 Introduction	2
1.3 Neural Data Acquisition	4
1.4 ECoG-Based BMI System Implementation	7
1.5 Results	12
1.6 Future Directions	15
1.7 Study Acknowledgements	18
2 Spatial-Temporal Functional Mapping (STFM) with Online Spectral Analysis of Electrocorticography	19
2.1 Abstract	19
2.2 Introduction	20
2.3 Materials and Methods	24

2.3.1	Patient and Clinical Settings	24
2.3.2	Experimental Testing and Event Markers	25
2.3.3	Electrode Localization	26
2.3.4	Online Data Acquisition and Analysis	27
2.3.5	Online Spectral Feature Extraction	28
2.3.6	Online Statistical Analysis	30
2.3.7	Raster Visualization	33
2.3.8	Brain Map Visualization	33
2.3.9	Offline Time-Frequency Analysis	34
2.3.10	ECoG Maps vs. Electrical Stimulation Maps	34
2.3.11	Region of Interest Analysis	35
2.4	Results	38
2.4.1	Spatial-Temporal Functional Mapping can be Performed	
	Online	38
2.4.2	Spatial-Temporal Functional Maps are Task-Specific	42
2.4.3	Micro-ECoG vs. Macro-ECoG Responses: Similarities and	
	Differences	45
2.4.4	ECoG Maps vs. Electrical Stimulation Maps	46
2.5	Discussion	48
2.6	Study Acknowledgements	58
3	Simultaneous Neural Control of Simple Reaching and Grasping	
	with the Modular Prosthetic Limb using Intracranial EEG	59
3.1	Abstract	59

3.2	Introduction	60
3.3	Methods	62
3.3.1	Subject Info	63
3.3.2	Neural Signal Acquisition	64
3.3.3	Experimental Procedures	65
3.3.4	iEEG Electrode Evaluation	67
3.3.5	BMI Model Training	68
3.3.6	JHU/APL Modular Prosthetic Limb	69
3.3.7	Online Testing	71
3.3.8	Quantitative Evaluation of Control	71
3.4	Results	73
3.5	Discussion	78
3.6	Study Acknowledgements	83
4	Overlapping Spatiotemporal Representations of Finger	
	Vibrations in the Postcentral Gyrus at 3 mm Scale in a Human Subject	84
4.1	Abstract	84
4.2	Introduction	85
4.3	Methods	89
4.3.1	Subject Info and Neural Signal Acquisition	89
4.3.2	Experimental Tasks	90
4.3.3	Event-Related Potential and Spectral Estimation	91
4.3.4	Finger Classification Analyses	93
4.4	Results	94

4.4.1	Somatotopy of Spectral Features and Event-Related Potentials	95
4.4.2	Timing of Activation	98
4.4.3	Single Trial Responses	100
4.4.4	Temporally Restricted Decoding Analyses	102
4.4.5	Comparing High Gamma Responses to Vibration and Movement-Related Sensation	104
4.5	Discussion	106
4.6	Study Acknowledgements	111
5	Long-Term Outlook of Electrocorticography for Functional Mapping and Brain-Machine Interface	112
5.1	Abstract	112
5.2	Electrocorticography: An Evolving Modality	112
5.2.1	Different Types and Scales of ECoG Implants	112
5.2.2	ECoG Technology Developments and hdECoG	114
5.2.3	Features of the ECoG Signal and the Emerging Dominance of the High Gamma Band	117
5.3	Alternative Techniques for Recording Neural Activity for Mapping and Brain-Machine Interface	122
5.3.1	Microelectrodes: Spike Firing Rates and Local Field Potentials	122
5.3.2	Functional Magnetic Resonance Imaging	127
5.3.3	Electroencephalography	129

5.4	Functional Mapping via ECoG Recordings vs. Electrocortical Stimulation Mapping	131
5.5	The Near Future of ECoG for Functional Mapping and Brain-Machine Interface	136
5.5.1	Extensions of this Thesis	136
5.5.2	Next Steps for Clinical ECoG-Based BMIs	139
	Bibliography	143
	Vita	178

List of Figures

- 1.1 MPL Photographs and Schematic. Pictures of the JHU/APL MPL (A) full limb, (B) a zoomed-in picture of the hand portion of the MPL, (C) a schematic showing the controllable joints proximal to the palm, and (D) a schematic showing the controllable and passive joints of the hand. © 2014 IEEE, included from (Fifer et al., 2014). 3
- 1.2 A schematic of an ECoG brain-machine interface (BMI). The configuration depicted involves acquisition of ECoG signals from electrodes placed on a human brain (left and top), their computational analysis and modeling (right) to drive a prosthetic limb (bottom). © 2012 IEEE. 4
- 1.3 Stylized and photographic examples of ECoG arrays. (left) Electroencephalogram (EEG), electrocorticogram (ECoG), and microelectrode arrays (MEAs) are contrasted in a stylized diagram. Notice that MEAs penetrate the pia mater and cortex, while the ECoG strip shown is merely subdural; EEG, by comparison records the signal after it has passed through the pia mater, arachnoid layer, dura mater, and scalp. (right) An intraoperative photo of an ECoG grid being placed in a human patient. © 2012 IEEE. 6
- 1.4 ECoG System Schematic. This schematic diagram depicts the flow of data and information throughout the parallel architecture described in the main text. Two key components of the system are neural data acquisition from Neuroscan (top left) and kinematic data acquisition from Optotrak and CyberGlove (top right). Each of the acquisition systems is saved to its own data file and simultaneously streamed into a custom MATLAB framework and processed by a parallel node. Frequency and amplitude features are extracted from the neural signals in real time and recorded with kinematics and target locations in a single composite data file (left). Simultaneous parallel port signals synchronize the neural and kinematic data to correct for clock drift for offline analysis (top). A physical or virtual prosthetic arm can be used driven from one of the parallel nodes using either pure kinematic data or models trained from previous offline recording sessions with the same subject (bottom). © 2012 IEEE. 8
- 1.5 Patient room experimental layout. A real object target is presented (from bottom right) as a cue to a patient (off-screen to the left for anonymity). The patient is pointing to the target, and his motions are being tracked by Optotrak markers on the shoulder and hand. The

three-dimensional position of the patient's hand and cue are being displayed in the MSMS simulation environment. The virtual cue is yellow, indicating a successful trial. © 2012 IEEE.

11

- 1.6. Spatial distribution of single feature decoding accuracy relative to identified motor electrodes. (a) Circles denote implanted electrodes that were included in the analysis, while darkened electrodes indicate that motor behavior was elicited or interrupted during electrocortical stimulation mapping (ESM). (b) – (f) Single feature decoding accuracies (Pearson's correlation r between observed and decoded traces) at electrode locations shown in (a) were used to reconstruct observed grasp aperture traces during reach-to-grasp movements. Only positive correlations were considered for display purposes. These plots show concentrations of good decoding electrodes in areas of cortex identified as motor by ESM. (Adapted and modified from (Fifer et al., 2011)). © 2011, 2012 IEEE.

13

- 1.7 Decoding of grasp aperture in four experimental sessions with one patient. The example traces above show the fidelity of decoded grasp aperture to observed grasp aperture. Predicted traces have been formed in fivefold cross-validation with linear models trained with twenty distinct neural signal feature inputs. (Adapted and modified from (Fifer et al., 2011)). © 2011, 2012 IEEE.

15

- 2.1 Online STFM Signal Processing Algorithm. A visual schematic is presented to describe the online signal processing and statistical methods used. A more detailed description of each step can be found in Section 2.3. N , \bar{x} , and s^2 represent sample size, mean, and variance, respectively.

28

- 2.2 Feature extraction algorithm illustration from auditory word repetition in Patient 1. The 'Silent' column plots are from a macroelectrode (LFT33 in Figure 2.3B) that had no significant task-related high gamma response. The 'Activated' column plots are from a microelectrode (PMIC13 in Fig 3B) with a significant task-related high gamma response. In (A)-(C), the units have been normalized so that the baseline period has zero mean and unit standard deviation. (A) Raw ECoG signals from the same single trial are shown after re-referencing to the common average reference (CAR). (B) The high gamma amplitude feature is shown after it was extracted from the same single trial shown in (A) using the algorithm described in Figure 2.1. (C) Post-stimulus high gamma amplitude averaged across all 96 trials of auditory word repetition is shown for both electrodes. (D) The average post-stimulus spectrogram is shown, calculated by averaging the FFT coefficients time-locked to the stimulus marker in 512 ms bins with 256 ms overlap. Time zero is the stimulus onset of each trial. This

spectrogram is not shown to the system user online, but is included here only for comparison with the feature output. 29

2.3 STFM of visual object naming (A) and auditory word repetition (B) in Patient 1. STFM results are shown as a raster of high gamma responses on the left, and as brain maps of high gamma response magnitude (represented by disc size and color) on the right. ESM maps (colored bars between electrodes) are also shown. Color-shaded areas denote anatomical boundaries of classical language areas used as regions of interest (ROI) in ROI sensitivity/specificity analysis. Color plots from offline matching pursuit analysis are illustrated below the brain maps for selected electrodes. Each raster plot displays the spatial-temporal distribution of significant increases (red spectrum) or decreases (blue spectrum) in high gamma energy relative to pre-cue baseline in 16 ms windows. Each row corresponds to a different electrode as displayed on the right brain maps. All times are relative to cue onset ($t=0s$). To highlight the spatial pattern of cortical activation at early (visual/auditory perception) and late (response production) stages, high gamma responses are integrated across an early and late temporal window (early stage highlighted in red and late stage in blue on raster plot), and shown in separate brain maps (early stage in the left brain and late stage in the right brain). Microelectrode arrays AMIC and PMIC are enlarged for better visualization of high gamma responses. The matching pursuit spectrograms are overlaid with line plots (blue) of online high gamma responses of respective electrodes averaged over trials. Matching pursuit spectrograms, arrows pointing to spectrograms, second brain image, and highlighting of early and late time periods on the channel raster have all been added to the screenshot post hoc (i.e., they are not available online). 32

2.4 Visual object naming task results for Patients 2-7 (P2-P7). ESM and Online STFM results are overlaid on brain maps with highlighted ROIs. As in Figure 2.3, online results are separated into early stage (visual perception, left brain) and late stage (response production, right brain), where high gamma responses were computed by integrating across an early or late temporal interval. Microelectrode arrays are enlarged for better visualization. 39

2.5 Auditory word repetition task results for Patients 2-7 (P2-P7). ESM and Online STFM results are overlaid on brain maps with highlighted ROIs. As above, online results are separated into early stage (auditory perception, left brain) and late stage (response production, right brain), where high gamma responses were computed by integrating across an early or late temporal window. Microelectrode arrays are enlarged for better visualization. 40

- 2.6 Single trial responses from online STFM results for Patient 1, auditory word repetition task. The single trial activations are shown for the auditory word repetition task in three separate electrodes: (A) LFT23, a macroelectrode in the early responding, putative stimulus perception cluster, (B) LFT45, a macroelectrode in the late responding, putative verbal response cluster, and (C) PMIC13, a microelectrode from the late responding cluster. The colors shown are scaled according to the negative log of the p -value, computed as a series of t -tests with the channel baseline distributions at the time of the trial. Significance thresholds have not been FDR corrected for multiple comparisons, as the single trial responses are primarily intended as an indicator of neural response consistency across trials. 41
- 2.7 Microelectrodes record ECoG high gamma responses with fewer required trial numbers for both tasks in Patient 1. With only 7 trials averaged from a visual object naming task (A) or an auditory word repetition task (B), statistically significant high gamma responses appeared in the microelectrode array. Responses are either absent in the macroelectrodes or have lower magnitudes than the microelectrodes with the highest magnitude responses. A similar trend is seen with more trials (145 in A, 96 in B). Magnitudes of statistically significant high gamma responses indicated by size/shading of red circles. 56
- 3.1 Functional mapping of cue-averaged task-related high gamma activity in training set. (A) Reconstruction of the implanted grid location for Subject 1 is depicted; the electrode used for reaching (number 25) is highlighted in red and corresponds to the channel circled in red in the activation maps below, while the electrode used for grasping (number 11) is highlighted in blue and similarly corresponds to the electrode circled in blue below; the central sulcus is highlighted in green. (B) Reconstruction of the depth electrodes implanted in right hemisphere of Subject 2; electrodes used for reaching highlighted in red, electrodes used for grasping highlighted in blue (transparent medial view in inset). (C, D) Each task map displays the spatiotemporal distribution of significant increases (red spectrum) or decreases (blue spectrum) in high gamma energy relative to pre-cue baseline in 16 ms windows for Subject 1. Each row corresponds to a different iEEG electrode in the frontoparietal grid displayed in (A). All times are relative to cue onset. (E) A differential map is shown for Subject 1, which is the result of a Wilcoxon test between two conditions for each (channel, time) pair with FDR correction for comparisons across multiple time points within each channel. Channel and time pairs are in the red spectrum if forward reach is more activated than grasp, and in the blue spectrum if grasp is more activated than forward reach. The average times of relevant behavioral events are marked with vertical lines and labeled

(movement onset, MO; pressed target button, PT; released target button, RT; returned arm to home position, Home; released pressure bulb, Rest). © 2014 IEEE.

62

- 3.2 Schematics and photographs of experimental setup with MPL. (top) A schematic of the experimental setup is shown, with Subject 1 seated and interacting with three behavioral sensors. The MPL is to the front and right of the subject, in the same room as and in full view of the subject. Traces of the behavioral sensors, high gamma power, and MPL commands during a three trial segment are shown as an example. (A-C) The subject is seated on his hospital bed (not pictured, right of view), with his arm at rest on a lap desk with inset pushbutton or “home switch.” The subject is holding but not actively grasping the squeeze bulb used to query grasp status. On the subject’s hospital tray are a pushbutton for reach offset detection and a laptop displaying a red bar indicating pressure exerted on the squeeze bulb. (A) In the background, the MPL is at its baseline state (rest posture). (B) The subject is executing a grasp movement, and (C) the subject is executing a reach movement. © 2014 IEEE.

65

- 3.3 Average change of power spectral densities (PSD) relative to baseline, aligned to movement onset. (A) Reach and grasp electrodes are shown for Subject 1, and (B) two representative electrodes are shown for Subject 1. The first vertical dashed line in all plots corresponds to the average time the audio cue began. For each trial, the baseline was chosen from before the onset of the cue (leftmost dashed line). The solid line denotes movement onset (MO). In reach trials, the dashed lines after the solid line correspond to the average time of the reach completion (pressing target button, PT), release of the target button (RT), and return to home (resting on the home switch), from left to right. The rightmost dashed line in the grasp trials corresponds to the average time of grasp completion. The PSD’s were computed via autoregressive spectral analysis. Window size did not allow for accurate calculations at 0-7.5Hz, so these frequencies are not displayed. © 2014 IEEE.

73

- 3.4 Limb performance accuracy metrics. (A, B) The accuracies are shown for reaching and grasping during trials where reach and grasp were executed simultaneously. (C, D) The reach and grasp accuracies are shown for reach and grasp only trials, respectively. The vertical dashed lines in A-D denote separate blocks. Distributions are shown and summarized with boxplots of the peak sensitivities for grasps in Subject 1 (E), reaches in Subject 1 (F), grasps in Subject 2 (G), and reaches in Subject 2 (H). Each distribution is comprised of the peak sensitivities from each trial. Bars above the boxplots with asterisks

mark distributions with significantly different medians ($p < 0.05$, Wilcoxon test). © 2014 IEEE.

77

- 4.1 hdECoG Grid Coverage and spatial map of high gamma responses. (left) An oblique lateral view of the patient's three-dimensional MRI reconstruction is shown. The red arrow points to the postcentral analogue of the primary motor cortex hand knob for reference. The red outline depicts the postcentral grid snippet used in Figures 4.3 and 4.7. The yellow outline surrounds the seven electrodes whose single trial responses are plotted in Figure 4.5. (right) A zoomed-in view of the hdECoG grid and underlying cortex is used as a background for plotting finger responses, or statistically significant ($p < 0.05$, FDR-corrected) increases in high gamma power relative to baseline, time-locked to 0.19 seconds after vibration onset. This time was chosen as it contained the largest magnitude aggregate increase across the hdECoG grid. The diameter of each circle is proportional to the z-scored measure of high gamma power increase, and the color represents the finger being stimulated in accordance with the key in the bottom right. Electrodes excluded from analysis are blackened. The fingers with the largest response at a given electrode are plotted first, and therefore are partially occluded when multiple fingers elicited a high gamma response in that electrode.

94

- 4.2 Spatial map of event-related potential amplitude and low frequency responses. These maps depict the z-scored absolute value of significant changes in amplitude (ERPs, left) or the strength of the decrease in low frequency power (three rightmost maps). The diameter of each circle is proportional to the z-scored measure of amplitude change or power decrease, and the color represents the finger being stimulated in accordance with the key in the bottom right. Electrodes excluded from analysis are blackened. The circle diameters are on the same relative scale as the high gamma plot in Figure 4.1. Since the timing of event-related potentials varies greatly by channel, the peak amplitude change was used to determine circle diameters; low frequency maps were created for the time periods with the largest aggregate magnitude decrease across the entire grid.

97

- 4.3 Finger Representation Somatotopy. (top row) The centers of mass, in two-dimensional electrode coordinate space, are plotted on the top right corner of the hdECoG grid for each feature type. Numbers 1 through 5 designate the first digit (thumb) through the fifth digit (pinky). (bottom row) The electrodes with the strongest response for a given finger for each feature type is plotted on the corresponding brain snippet. The placement of the postcentral snippet within the context of the larger hdECoG grid is depicted in Figure 4.1.

98

- 4.4 Temporal profiles of spectral and amplitude representations of finger vibrations. (A) The high gamma traces for all electrodes with any significant activation in any post-stimulus time window ($p < 0.05$, FDR-corrected) is averaged separately for each finger response. (B) The average magnitudes of all significant amplitude responses for each finger is shown. (C-E) The averages of all sites with significant task-related low frequency decreases are shown for theta, mu, and beta bands. Colored dots correspond to: (A) the largest increase, or (C-E) the largest decrease for a given averaged finger response. In (B), solid dots correspond to the peak magnitude during stimulation, while empty dots denote peak magnitude after stimulation offset. Legends in each plot detail how many sites were used to compose each averaged finger response. 100
- 4.5 Single trial high gamma and beta responses for six adjacent electrodes. High gamma (top) and beta (bottom) responses are shown for the same six adjacent electrodes, arranged along the inferior-superior axis of the grid (depicted in Figure 4.1). Responses from the most superior electrode, from the top row of the grid, are depicted in the leftmost sub-plot. Each row within each sub-plot is a trial, and the horizontal axis represents time after the onset of the stimulus. Trials have been reordered so that all thumb trials appear together, followed by all index finger trials, etc., and the transitions between finger types are marked with black lines. 101
- 4.6 Time-restricted classification accuracy across feature types and smoothing kernel widths. The cross-validated classification accuracy in time windows time-locked to stimulus onset are plotted. Classification results are plotted for high gamma (black), smoothed amplitude (blue), theta (cyan), mu (magenta), and beta (red) features are shown at each smoothing kernel widths. Smoothing over window centers spanning 16 ms (no smoothing for spectral features, 16 ms smoothing for ERPs), 112 ms, and 240 ms are shown. A clear secondary peak in decoding accuracy emerges for smoothed amplitude feature models which is not apparent for the models with spectral feature inputs. 104
- 4.7 Comparison between vibration responses and movement-related sensory high gamma responses. Significant activation at 0.19 seconds post stimulus onset (top left) and 0.03 seconds prior to peak finger flexion in the motor task (top right) are depicted. The diameters of the circles depict high gamma power increases z-scored with respect to the baseline period. They are on identical scales, but a different scale from Figures 1 and 2. The placement of the postcentral snippet within the context of the larger hDECog grid is depicted in Figure 4.1. The

centers of mass (middle row) and representation peaks (bottom row) are depicted for both vibration (left) and motor (right) tasks. 106

List of Tables

2.1	Patient Demographic and Clinical Information	25
2.2	Structure of STFM vs. ESM test results among ROI+ and ROI- stimulation sites	38
2.3	Sensitivity and specificity values for STFM during visual object naming and auditory word repetition tasks, with ESM as the gold standard	47
2.4	STFM vs. ESM test results among ROI+ and ROI- stimulation sites, across all patients	47
2.5	Comparison of sensitivity/specificity calculation for different studies	53
3.1	Summary of MPL specifications. © 2014 IEEE.	70
5.1	Information gained from resections, ESM, and ECoG results for resected sites. Grayed out rows are ESM-positive and would thus be underrepresented in a database of resected sites. Each row corresponds to a specific set of attributes of a single resected site: (1) Did the resection cause a deficit in the task of interest?, (2) Is this site truly functionally related to the task of interest?, (3) Did ESM identify this site as task-related?, and (4) Did ECoG identify this site as task-related? The last column highlights information gained (sometimes incorrectly) about a site with the specified set of attributes. Note: this table assumes that a lesion could result from the resection of another site, which is why the first and second columns are different.	135

Page intended to be blank

Chapter 1

Towards Electrocorticographic Control of Dexterous Upper Limb Prosthesis

1.1 Abstract

One of the most exciting and compelling areas of research and development is building brain-machine interfaces (BMIs) for controlling prosthetic limbs. Prosthetic limb technology is advancing rapidly, and the Johns Hopkins University/Applied Physics Lab (JHU/APL) Modular Prosthetic Limb (MPL) permits actuation with 17 degrees of freedom in 26 articulating joints. The reciprocal challenge is to derive a similar number of control signals for the prosthetic limb, with the ultimate solution for those with upper limb loss likely involving some degree of direct neural control. There are many signals from the brain that can be leveraged, including the spiking rates of neurons in the cortex, electrocorticographic (ECoG) signals from the surface of the cortex, and electroencephalographic (EEG) signals from the scalp, and. Unlike spike recording microelectrodes, ECoG does not penetrate the cortex. ECoG also has higher spatial specificity, signal-to-noise ratio, and bandwidth than EEG signals.

We have implemented an ECoG-based system for controlling the MPL. This system is composed of simultaneous neural and kinematic data acquisition modules which can correlate the neural activity to upper limb kinematics and drive either a virtual arm or the MPL limb. We have implemented this system in the Johns Hopkins

Hospital Epilepsy Monitoring Unit, where patients are implanted with ECoG electrode grids for clinical seizure mapping and asked to perform various recorded finger or grasp movements. We have shown that low frequency local motor potentials and ECoG power in the high gamma frequency (70-150 Hz) range correlates well with grasping parameters and they stand out as good candidate features for closed-loop control of the MPL. This demonstration sets the stage for testing dexterous neural control of the MPL with ECoG signals from human subjects.

1.2 Introduction

An estimated 541,000 Americans were living with some form of upper limb loss in 2005, and that number is projected to more than double with an aging and growing population by 2050 (Ziegler-Graham et al., 2008). Loss of limb may occur congenitally or due to cancer, diseases of the vasculature, or trauma (Dillingham et al., 2002)—including industrial or farming accidents and battlefield injuries. With respect to trauma, recent wars in Iraq and Afghanistan have resulted in a large veteran population with substantial upper limb loss. This recognition has spurred research on the development of advanced prosthetic limbs. One outstanding example has been the JHU/APL Modular Prosthetic Limb (Figure 1.1), which has 17 controllable degrees of freedom in 26 articulating joints (Johannes et al., 2011). This limb has actuators to control shoulder, elbow and wrist in addition to the fingers and thumb, providing extensive dexterous capabilities. Such an advanced limb also poses a control problem. Traditional approaches have used myoelectric signals from the forelimb of trans-radial amputees. Another more recent approach

has been the use of peripheral nerve re-innervation of the chest, using orphaned muscles as a biological amplifier for nerve signals to control a prosthetic limb (Kuiken et al., 2004). Despite these well-accepted approaches, there is good reason to believe that it is possible to achieve direct neural control of prosthetics that is intuitive and adaptive, involving the subject's full sensory, motor, and cognitive capabilities.

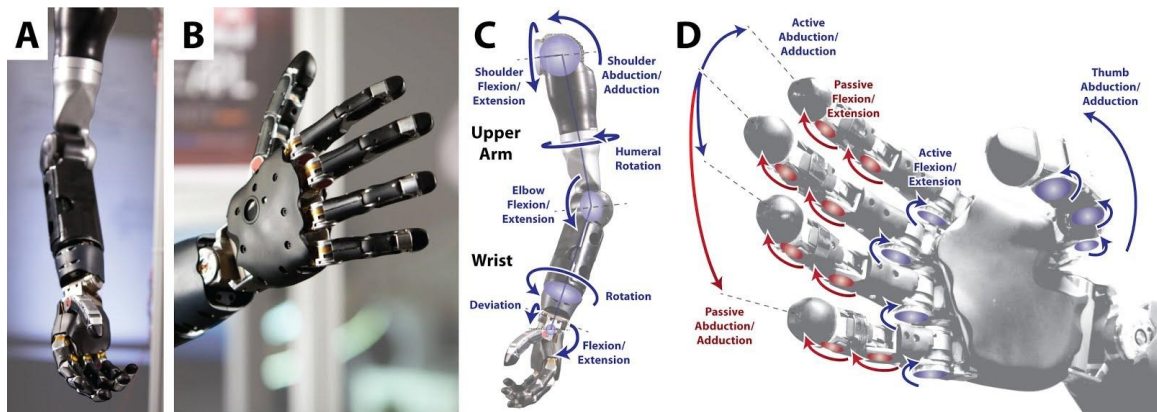


Figure 1.1. MPL Photographs and Schematic. Pictures of the JHU/APL MPL (A) full limb, (B) a zoomed-in picture of the hand portion of the MPL, (C) a schematic showing the controllable joints proximal to the palm, and (D) a schematic showing the controllable and passive joints of the hand. © 2014 IEEE, included from (Fifer et al., 2014).

There are also many conditions in which control of the upper limbs is lost without explicit injuries to the limbs themselves. Conditions of the central nervous system such as amyotrophic lateral sclerosis (ALS, or Lou Gehrig's disease) and traumatic events such as stroke and spinal cord injury (SCI) can disrupt the upper limb control pathways upstream of the peripheral nerves. These debilitating conditions can leave patients completely dependent on others or occasionally unable to communicate at all. One area of research with these patients is attempting to leverage their still-functional brains for direct control of a machine, be it a

prosthetic hand (Yanagisawa et al., 2011), computer cursor (McFarland et al., 2010; Wolpaw et al., 1991), or wheelchair (Galán et al., 2008). These research areas are collectively referred to as brain-machine interfaces (BMIs). The goal of BMIs is to interject a machine into the anatomical pathways of the human nervous system to augment, alter, or replace an end effector or lost control of it (Figure 1.2). The term “end effector” is a fairly succinct way of intimating that a great deal of human functions are currently being targeted by the BMI community—while our lab focuses on replacing upper limb functionality (Acharya et al., 2010; Aggarwal et al., 2008; Tenore et al., 2009), work is being done on text-based neural communication devices (Birbaumer et al., 1999), speech synthesis from neural signals (Kellis et al., 2010), and memory augmentation (Berger et al., 2011).

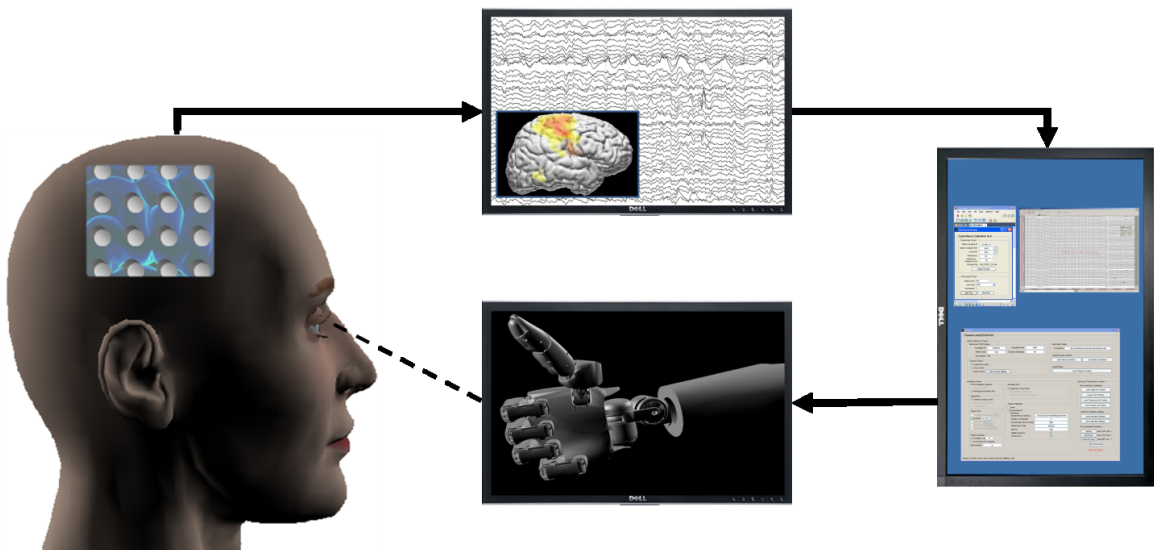


Figure 1.2. A schematic of an ECoG brain-machine interface (BMI). The configuration depicted involves acquisition of ECoG signals from electrodes placed on a human brain (left and top), their computational analysis and modeling (right) to drive a prosthetic limb (bottom). © 2012 IEEE.

1.3 Neural Data Acquisition

The BMI community has explored many different avenues of access to neural signals for BMI applications, but traditionally four modalities dominate: 1) electroencephalography (EEG) is the measure of neural potentials arising from the cortex with electrodes placed on the scalp, 2) electrocorticography (ECoG) is the measure of cortical potentials from the surface of the cortex, 3) local field potentials (LFP) are the low-pass filtered (e.g., 200 Hz) electrical potentials recorded from microelectrodes, and 4) single or multi-unit recordings to detect action potentials (or "spikes") from neighboring neurons. Each of these modalities has a distinct set of strengths and weaknesses that require the experimenter to prioritize his or her study objectives. The EEG signal is very desirable due to its noninvasive nature and has been successfully used to decode limb movements (Bradberry et al., 2010). However, the EEG signal is difficult to acquire due to extensive electrode preparation, and may be subject to movement artifacts. EEG also does not capture high frequency oscillations (e.g., high gamma band, typically above 70 Hz), primarily due to low signal-to-noise from the large distances between neural sources and EEG sensors (Pfurtscheller and Cooper, 1975). Spike recordings represent a fundamental unit of neural activity, and hence their use for acquiring neural movement-related signals and for driving a robotic limb is well known (Chapin et al., 1999; Velliste et al., 2008). However, microelectrodes by design penetrate the cortex (Figure 1.3(a)) and consequently elicit an immune response that degrades the signal quality over the course of months to years (Mercanzini et al., 2009; Williams et al., 1999). Spike recordings are also specifically subject to micro-

motion of the electrode recording sites, which causes individual neurons to drop in and out of recordings on a day-to-day basis.

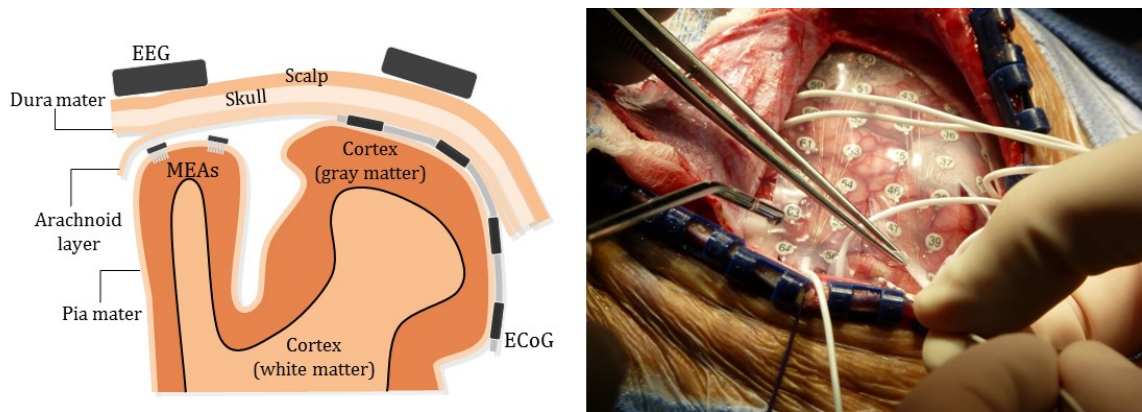


Figure 1.3. Stylized and photographic examples of ECoG arrays. (left) Electroencephalogram (EEG), electrocorticogram (ECoG), and microelectrode arrays (MEAs) are contrasted in a stylized diagram. Notice that MEAs penetrate the pia mater and cortex, while the ECoG strip shown is merely subdural; EEG, by comparison records the signal after it has passed through the pia mater, arachnoid layer, dura mater, and scalp. (right) An intraoperative photo of an ECoG grid being placed in a human patient. © 2012 IEEE.

Considering the potential strengths and weaknesses associated with these methods, ECoG occupies unique middle ground among these technological tradeoffs. There have been a few pioneering efforts to use ECoG recording for BMI purposes. These include control of a cursor in one and two dimensions (Leuthardt et al., 2004; Schalk et al., 2008b) and decoding of individual finger movements (Kubaneck et al., 2009), slow grasping motions of the hand (Acharya et al., 2010), and grasp type (Yanagisawa et al., 2011). Two qualitatively different features of the ECoG signal are emerging from these studies. Power in the high gamma band (>70 Hz) has been established as a reliable index of cortical processing, and has been correlated in various anatomical brain regions with selective attention (Ray et al., 2008b), speech (Crone et al., 2001b), auditory perception (Crone et al., 2001a), and movements

(Crone et al., 1998). In addition, the recently reported local motor potential (LMP) (Schalk et al., 2007) is a simple moving average of the ECoG signal and has been used for decoding slow grasping motions of the hand (Acharya et al., 2010) and individual finger movements (Kubanek et al., 2009).

ECoG electrode grids are predominantly implanted for clinical purposes in patients with uncontrollable epileptic seizures (Figure 1.3(b)). The grids allow neurologists to map out areas of the patient's brain which are generating seizures and areas that are responsible for vital functions like movement and speech (i.e., "eloquent cortex"). This functional map can be used to guide neurosurgeons in the targeted removal of the patient's seizure focus while avoiding eloquent cortex to the greatest extent possible (Luders et al., 1986). Patients are generally implanted with intracranial electrodes for about one week. Before a second procedure to remove the electrodes and resect pathological tissue identified during monitoring, ECoG patients frequently volunteer for neuroscience experiments that can be carried out with no added medical risks.

1.4 ECoG-Based BMI System Implementation

The system we have developed and continue to refine (Figure 1.4) is designed to enable communication between and synchronization of three distinct nodes. In general terms, these nodes are responsible for neural signal acquisition and processing, behavioral kinematic acquisition, and artificial limb actuation.

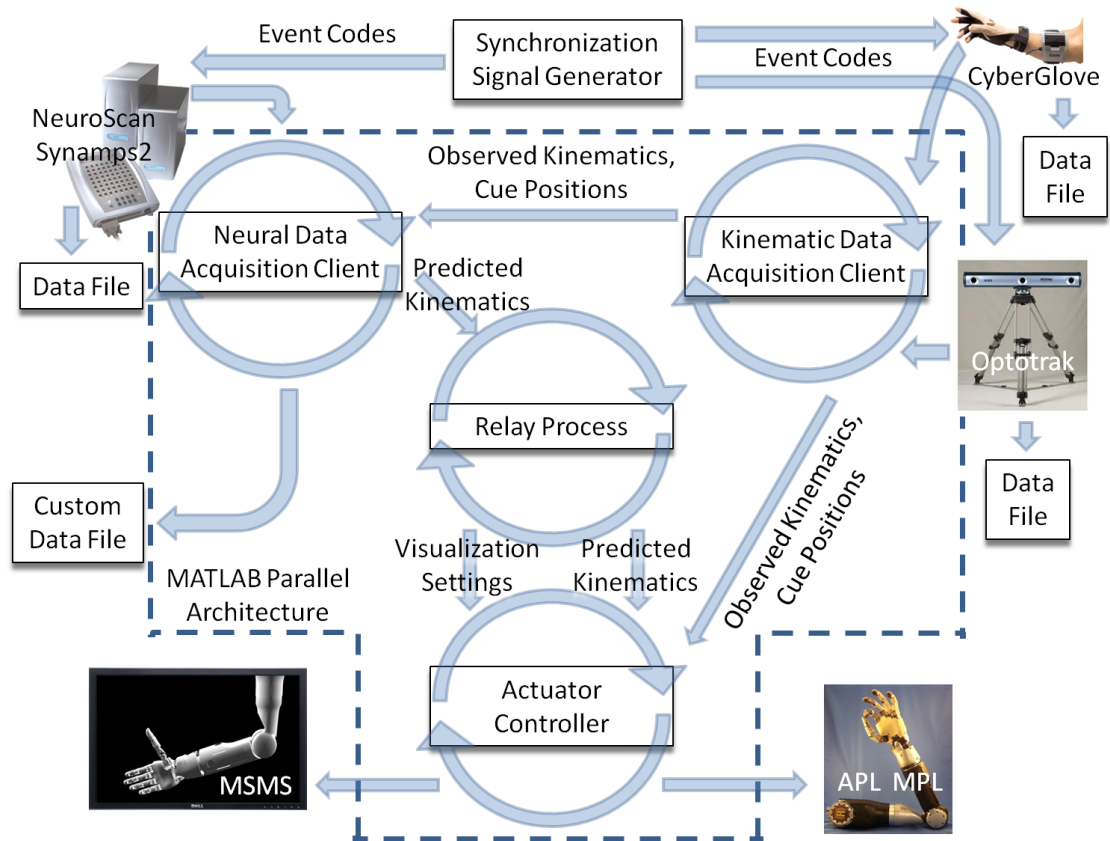


Figure 1.4. ECoG System Schematic. This schematic diagram depicts the flow of data and information throughout the parallel architecture described in the main text. Two key components of the system are neural data acquisition from Neuroscan (top left) and kinematic data acquisition from Optotrak and CyberGlove (top right). Each of the acquisition systems is saved to its own data file and simultaneously streamed into a custom MATLAB framework and processed by a parallel node. Frequency and amplitude features are extracted from the neural signals in real time and recorded with kinematics and target locations in a single composite data file (left). Simultaneous parallel port signals synchronize the neural and kinematic data to correct for clock drift for offline analysis (top). A physical or virtual prosthetic arm can be used driven from one of the parallel nodes using either pure kinematic data or models trained from previous offline recording sessions with the same subject (bottom). © 2012 IEEE.

Neural signal acquisition is accomplished using Neuroscan (Compumedics; Charlotte, NC) SynAmps2 hardware that can be used to amplify either EEG or ECoG signals. For our ECoG experiments, neural signals are sampled at 1000 Hz with a bandpass filter from 0.15 Hz to 200 Hz. As shown schematically in Figure 1.4 (top

left), Neuroscan SCAN software streams the raw neural data samples over TCP/IP, where they are received by our custom MATLAB (MathWorks, Inc.; Natick, MA) code and processed to extract signal features relevant to human motor movements. Raw neural signals are first re-referenced to a common average reference (CAR) in the time domain as a spatial filter (McFarland et al., 1997), to remove elements of the signal common to all channels. Time and frequency domain features are then extracted from the CAR-filtered channel data. Specifically, the signal power is extracted in five physiologically relevant frequency bands (i.e., μ band, 7-13 Hz; β band, 16-30 Hz; low γ band, 30-50 Hz; high γ band, 70-100 Hz and 100-150 Hz) using the Fast Fourier Transform (FFT) and two amplitude time windows (i.e., 512 ms, 2048 ms) using moving average filters. These features are extracted approximately every 40 ms and synchronized with streaming behavioral kinematic data.

Behavioral kinematic data acquisition is accomplished using the Optotrak system (Northern Digital, Inc.; Ontario, Canada) and the CyberGlove (CyberGlove Systems, San Jose, CA), as depicted in Figure 1.4 (top right). Optotrak is an optical tracking system which allows the placement of active sensing markers onto the experimental subject for three-dimensional tracking with sub-millimeter precision. The CyberGlove is a 22 degree of freedom data glove with embedded bend sensors for tracking the flexion and extension of all five digits and the wrist. In our experimental setup, three dimensional reach trajectory is tracked with Optotrak sensors placed on the shoulder and wrist in a reference frame pre-calibrated to be aligned to the axes of the room. The CyberGlove also enables simultaneous tracking

of the postures achieved by the fingers and wrist to accomplish dexterous grasp behaviors. Since the CyberGlove does not rely on line-of-sight tracking, it can be used during arbitrarily complex grasps without risk of occlusion. During experiments, our MATLAB software queries the Optotrak sensor positions and CyberGlove joint angles at 25 Hz.

Artificial limb actuation is achieved either in three-dimensional virtual or physical space. JHU/APL has previously reported and demonstrated the Modular Prosthetic Limb (MPL), a 27 degree of freedom prosthetic arm complete with control of shoulder, elbow, wrist, and fingers. This arm has been duplicated as a virtual model in the Musculoskeletal Modeling Software (MSMS) simulation environment (Davoodi et al., 2004), which has been developed at the University of Southern California and is freely available online. Object cues are tracked using the Optotrak system and can be placed in the simulation environment for visualization purposes. Depending on the experimental protocol, the subject can actuate either the physical or virtual arm to make contact with a physical or virtual cue.

While real-time feature extraction is necessary for online control of a physical or virtual prosthetic, the computational limitations it places on algorithm selection are intense. Both the Optotrak and Neuroscan systems are capable of simultaneous data recording and TCP/IP streaming. A synchronizing pulse is sent intermittently to both systems (top middle, Figure 1.4), which is stored alongside channel and marker data for offline co-registration of the data sampled at the highest possible rate. This synchronized dataset allows for more sophisticated post-hoc neural feature extraction that simply is not possible in a real-time environment.

The computational resources necessary to process the incoming neural and kinematic data are contained within a single eight core Dell Workstation with 32 GB RAM, of which four are dedicated to MATLAB's Parallel Computing Toolbox. Each node in the parallel framework is denoted by cycling arrows in Figure 1.4. The entire setup for these experiments needs to be mobile; development occurs in our research laboratory, but the testing itself occurs in the subject's room in the Epilepsy Monitoring Unit of Johns Hopkins Hospital. ECoG patients are literally tethered to the wall, as long cables constantly transmit neural data from their cortices to the hospital's recording hardware for continuous monitoring. Our workstation, along with the Optotrak and Neuroscan recording hardware, is contained on a single cart (Anthro; Tualatin, OR) and all of these are powered by an isolated power supply unit. The cart and the Optotrak 3-camera sensor are rolled into the subject's room. A photograph of this environment including a patient seated in his hospital room is depicted in Figure 1.5.



Figure 1.5. Patient room experimental layout. A real object target is presented (from bottom right) as a cue to a patient (off-screen to the left for anonymity). The patient is pointing to the target, and his motions are being tracked by Optotrak markers on the shoulder and hand. The three-dimensional position of the patient's hand and cue are being displayed in the MSMS simulation environment. The virtual cue is yellow, indicating a successful trial. © 2012 IEEE.

1.5 Results

We have used the system described to initiate research into ECoG-based control of a dexterous prosthetic limb. As summarized above, this work involves performing experiments with subjects who have been implanted with ECoG grids for seizure monitoring and who volunteer for our limb trials. In previously published work (Acharya et al., 2010), our lab discovered that the LMP recorded from subjects implanted with ECoG grids could be used to decode slow grasping motions of the hand with simple linear models. A great deal of the predictive power of these models was achieved with only a single electrode, and the peak decoding accuracy was obtained with between four and six electrodes in the best performing subjects. LMP signals with highest correlation to the recorded kinematics were selected for inclusion in the decoding models. These signals were highly concentrated in areas of cortex that were shown to be involved in motor behavior using electrocortical stimulation mapping (ESM). Peak decoding performance was achieved with as few as four electrodes in areas that can be identified intraoperatively as having motor involvement, meaning that these signals can be recorded from low-footprint ECoG grids implanted in known areas. These results are very promising for the use of LMP signals for neuroprosthetic applications. The

robustness of LMP as a phenomenon is validated by the high decoding accuracy across sessions.

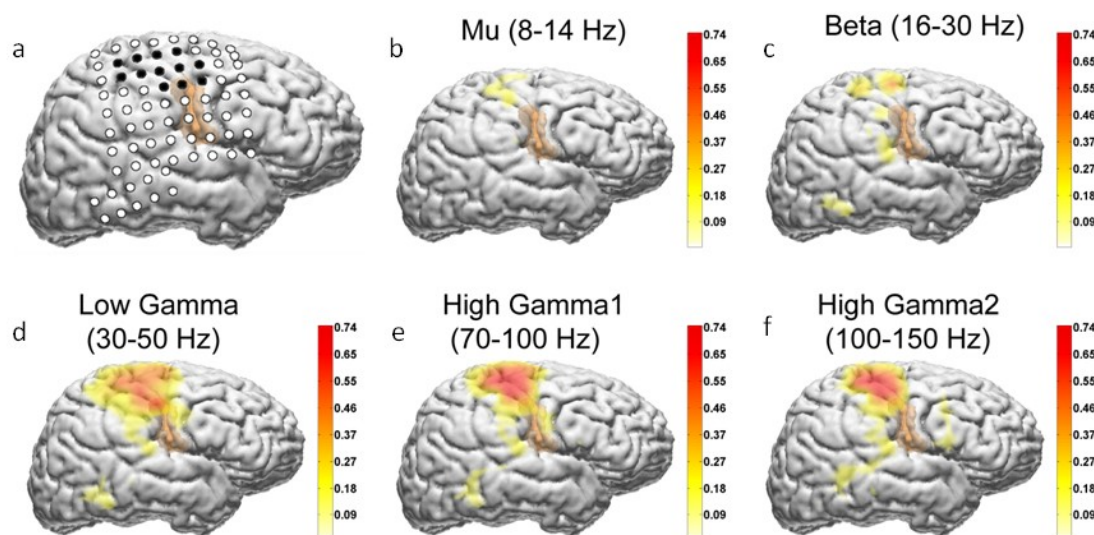


Figure 1.6. Spatial distribution of single feature decoding accuracy relative to identified motor electrodes. (a) Circles denote implanted electrodes that were included in the analysis, while darkened electrodes indicate that motor behavior was elicited or interrupted during electrocortical stimulation mapping (ESM). (b) – (f) Single feature decoding accuracies (Pearson’s correlation r between observed and decoded traces) at electrode locations shown in (a) were used to reconstruct observed grasp aperture traces during reach-to-grasp movements. Only positive correlations were considered for display purposes. These plots show concentrations of good decoding electrodes in areas of cortex identified as motor by ESM. (Adapted and modified from (Fifer et al., 2011)). © 2011, 2012 IEEE.

In more recent work from our lab, we investigated the neural signals responsible for the coordination of slightly more complex grasps (Fifer et al., 2011). A subject was verbally cued to reach out and grasp a series of objects with varying shapes and sizes. ECoG signals were decomposed into various spectral bands. Our study showed that frequency components in the high gamma band (70-100 Hz and 100-150 Hz) provide the best performance for decoding grasp aperture. Using a linear model that incorporated information from the high gamma band at multiple

time points, we were able to achieve very high accuracy using a single electrode that improved only slightly with the addition of information from other features and electrodes. Figure 1.6a shows the location of the implanted grid electrodes, with darkened electrodes corresponding to motor brain areas as identified by ESM. Figures 1.6b-f show the spatial pattern of decoding accuracies used with single electrodes from various locations on the cortex. Again, the highest-performing electrodes appear to be concentrated over areas identified as having motor involvement prior to experimentation. Figure 1.7 visually depicts correspondence between observed and decoded grasp aperture traces using the twenty features that best predict grasp aperture in each cross-validation training set. Although not shown here, the LMP signal recorded during this experiment performed poorly in decoding grasp aperture during these complex and rapid reach movements.

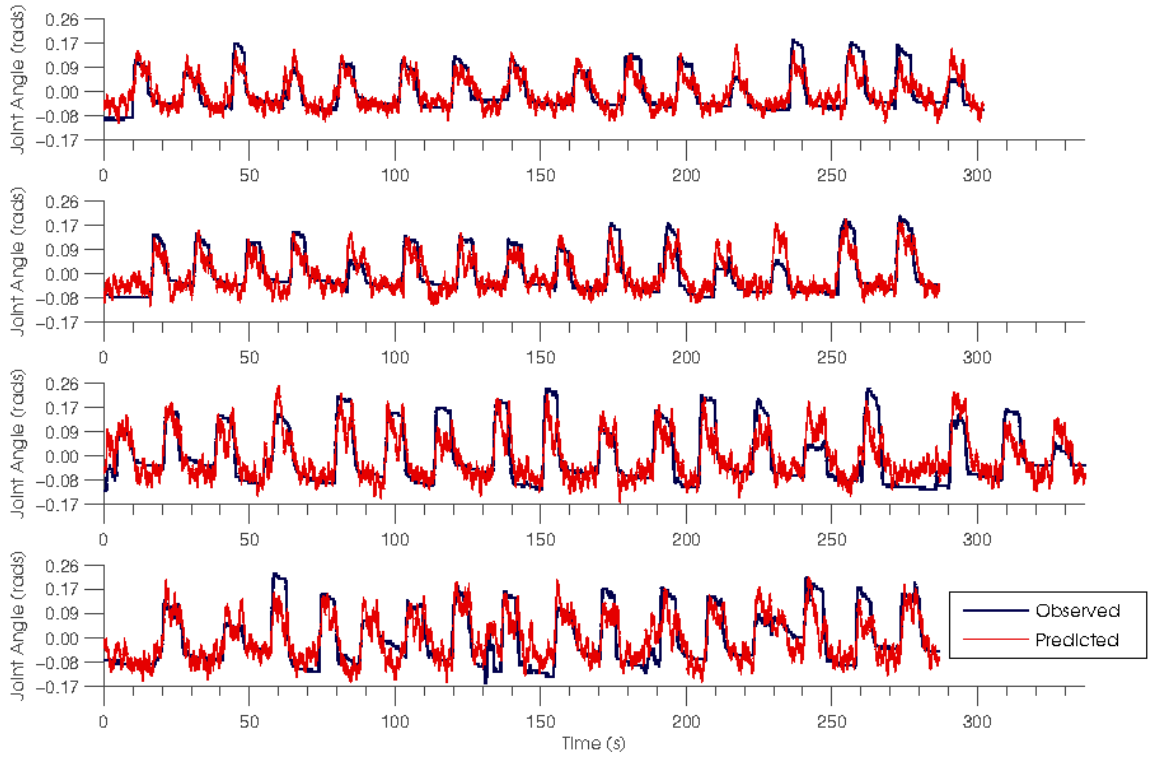


Figure 1.7. Decoding of grasp aperture in four experimental sessions with one patient. The example traces above show the fidelity of decoded grasp aperture to observed grasp aperture. Predicted traces have been formed in fivefold cross-validation with linear models trained with twenty distinct neural signal feature inputs. (Adapted and modified from (Fifer et al., 2011)). © 2011, 2012 IEEE.

Our results not only indicate that complex movements can be decoded from a patient's ECoG signal, but that both LMP (an amplitude feature) and high gamma band (a spectral feature) should be considered in decoding complex motor tasks. While it is an area of active investigation, it is our hypothesis that the LMP, as a slower signal, encodes information about low velocity or repetitive movements fairly robustly, while the high gamma band may be more useful for decoding movements with higher degrees of complexity or more sudden onset.

1.6 Future Directions

While our lab and the BMI research field as a whole have enjoyed success in neural decoding, ECoG research has its challenges and limitations. It is important to emphasize that the goals of electrode implantations are solely clinical in nature—to treat debilitating seizures and avoid post-operative neurological impairments. BMI experiments cannot interfere with these goals or add risk to the patient. Because invasive monitoring is often a last resort for treating epilepsy, there are relatively few subjects available for neural recording specifically for BMI applications and demonstrations of neuroprosthetic control. These patients are in the hospital for a week, but the majority of their time is dedicated to mapping out seizure foci and eloquent cortex. BMI researchers are often able to spend several hours with each ECoG subject—including setting up the experimental equipment and explaining the experimental protocol. During this relatively brief time, it is necessary for researchers to test the instrumentation, algorithms and the operation of the closed-loop BMI system, not to mention allow the subject to adapt to controlling the BMI. Additionally, placement of the grids is decided solely on the basis of the patient's clinical needs. Epilepsy and any associated structural pathology can also be associated with substantial cortical reorganization (Rasmussen and Milner, 1977; Datta et al., 2013). These dual factors mean that every patient's grid records from slightly different brain areas and that it takes time to understand the functions performed by the neuronal populations sampled by the implanted electrodes in each individual subject. To address the scarcity of subject time with ECoG, researchers are beginning to create models of human subject control (Cunningham et al., 2011).

One limitation of our neural decoding approach is that we have been studying the neural signals generated by subjects with intact limbs and relatively healthy motor cortices. Patients in our target population have lost the ability to move their natural upper limbs, so we will need to think creatively about detecting innate neural control signals. Existing literature has shown that imagining (Beisteiner et al., 1995; Miller et al., 2010) or watching (Iacoboni et al., 1999) a movement generates similar neural activity to actually performing it, which could be used to train first-pass neural decoding models of complex arm and hand movements. In order to test these methods and their effectiveness with the end-user, it will be useful to test patients with pre-existing motor impairments. This has been done with one patient already at the University of Pittsburgh (Wang et al., 2013), but there will be a significant need to prove the safety and efficacy of these studies before more widespread clinical trials can occur.

We are making steady progress toward the dream of neural control of prosthetic limbs using a variety of means, but the journey is just beginning. A few major challenges to achieving ECoG based control of dexterous prosthetic remains include: 1) improving the resolution of ECoG arrays; high resolution ECoG with arrays of mini- and micro-electrodes may provide better localization to the areas of the cortex responsible for dexterous hand and finger movements; 2) maturation of decoding algorithms specifically suited to ECoG signals; ECoG signals in very low frequency as well as high gamma bands may offer novel decoding capabilities and information; 3) provision of proprioceptive and touch feedback to the neuroprosthetic user by stimulating intact peripheral nerves or directly stimulating

somatosensory cortex (London et al., 2008; O'Doherty et al., 2011; Suminski et al., 2010) may greatly facilitate natural control of an artificial limb; 4) building fully implanted ECoG systems—long-term cortically-controlled prosthetics will need to be comprised of electrodes, circuits, and telemetry interface to the limb while being fully implanted and powered.; 5) ethical considerations in selection of patients and implantation with regards to the potential risks of benefits to each individual patient.

1.7 Study Acknowledgements

This work was launched by the DARPA Revolutionary Prosthetics (RP2009) program Phase I and II that funded the development of the JHU/APL prosthetic limb and decoding work. Recent work on human subjects was funded by the Phase III DARPA funding to JHU/APL and clinical investigation by the National Institute of Neurological Disorder and Stroke Grant 3R01NS040596-09S1. We would like to thank Rahman Davoodi at the University of Southern California for assistance with the MSMS simulation environment, and the MPL team at the Johns Hopkins Applied Physics Lab for providing an MSMS model of their MPL. Most importantly, we thank the patients who volunteer to be subjects for ECoG experiments. Progress in our lab and in the BMI community as a whole continues to depend critically on of their valuable time and effort.

Chapter 2

Spatial-Temporal Functional Mapping (STFM) with Online Spectral Analysis of Electrocorticography

2.1 Abstract

Spectral analysis of electrocorticographic (ECoG) recordings has emerged as a potential alternative to electrocortical stimulation mapping (ESM) for epilepsy or brain tumor surgery patients. However, the complex brain dynamics involved during language tasks present unique challenges for testing and interpretation, and investigators have observed less correspondence between ECoG and ESM maps for language tasks than for motor tasks. Here we demonstrate the feasibility and utility of an online *spatial-temporal functional mapping* (STFM) system that exploits ECoG's temporal resolution to study the evolution of neuronal population activity across all recording sites simultaneously. We illustrate how this information is particularly useful for mapping language function. The average sensitivity and specificity of online STFM across seven subjects were 69.9% and 83.5%, respectively, using ESM as the gold standard. Moreover, relative to regions of interest where cortical lesions have most reliably caused language impairments in the literature, the sensitivity of STFM was significantly greater than that of ESM, while its specificity was also greater than that of ESM, though not significantly so. This study supports the feasibility and clinical utility of online STFM for mapping human language function,

particularly under clinical circumstances in which time is limited and comprehensive ESM is impractical.

2.2 Introduction

Despite ongoing advances in non-invasive functional neuroimaging, electrocortical stimulation mapping (ESM) remains the gold standard for mapping cortical function at a fine spatial scale in individual patients prior to resecting cortical tissue for the treatment of drug-refractory epilepsy (Lesser et al., 1994; Penfield and Jasper, 1954) and brain tumors (Sanai et al., 2008). The major advantage of this technique is that it allows clinicians to simulate the neurological consequences of lesioning tissue before it is permanently resected (Ojemann et al., 1989). However, there are important practical limitations on its clinical application. Chief amongst these is the risk of triggering afterdischarges and clinical seizures (Blume et al., 2004; Hamberger, 2007; Lesser et al., 1984) that can prevent comprehensive functional mapping without contributing to localization of the patient's ictal onset zone. Additionally, ESM can elicit pain that prevents mapping at individual sites (Lesser et al., 1985). Lastly, because ESM is done sequentially at pairs of electrodes, finding the optimal stimulation current (Lesser et al., 1984; Pouratian et al., 2004) and then testing the effect of stimulation on different language tasks (Schäffler et al., 1993), it is time-consuming. This can force clinicians to map only a subset of sites. This factor may ultimately pose a particularly acute limitation on ESM as the number and density of ECoG electrodes used for long-term monitoring increases (Viventi et al., 2011; Bouchard and Chang, 2014).

In addition to the practical limitations on ESM's clinical application, there are a number of concerns about its accuracy and predictive value. The neural populations and operations that are interrupted during stimulation are not well controlled, and it is difficult to rule out distant effects through diaschisis or the distant effects of action potentials evoked by stimulation (Hamberger, 2007; Ishitobi et al., 2000; Karakis et al., 2015). Furthermore, the simulated lesion of ESM cannot take into account the reorganization that occurs after real permanent lesions, and if it is done in only a subset of electrodes, it cannot identify other cortical sites that could potentially assume the function of the lesioned site (i.e., assess functional reserve). Finally, when ESM interrupts the performance of a cognitive task such as word production, the effect is usually all-or-none. The same observed effect can potentially result from interruption of different stages of processing or levels of representation that are necessary for successful task completion.

The limitations of ESM have long motivated the investigation of passive ECoG recordings as a tool for mapping cortical function prior to resective surgery (Cervenka et al., 2013; Crone et al., 2001b, 1998; Grossman and Gotman, 2001; Sinai et al., 2005). ECoG recordings cannot trigger seizures or pain, and they can be used to simultaneously survey task-related cortical activity in the entire set of implanted electrodes. In addition, ECoG recordings yield a graded measure of task-related neural activity capable of resolving the activation of cortical sites at temporal scales comparable to the stages of processing that comprise language tasks (Edwards et al., 2010). Thus, the relative degree and timing of activation at a given site can be used to estimate its contribution to these processing stages, providing clinicians with

more information as they weigh the benefits and risks of removing epileptogenic tissue vs. sparing eloquent cortex.

In spite of its practical and theoretical advantages over ESM, ECoG functional mapping has not been widely used in clinical practice. One reason for this has been a lack of consensus on which signal components are most informative about task-related neural activity. In recent years, high gamma (~ 60 to 200 Hz) power changes have been increasingly recognized as a robust and reliable index of task-related activation of cortical populations of neurons (Crone et al., 2011, 2006; Jerbi et al., 2009; Lachaux et al., 2012). This index is highly correlated with blood oxygen level-dependent (BOLD) responses in fMRI (Genetti et al., 2014; Khursheed et al., 2011; Lachaux et al., 2007a; Siero et al., 2014) and with single unit activity recorded by microelectrodes (Ray et al., 2008a; Manning et al., 2009). Accordingly, it is highly specific with respect to the location and timing of task-related cortical activation, and it has been observed in nearly every cortical functional-anatomical domain in which it has been studied, including sensorimotor, auditory, visual, and language areas (Crone et al., 2011; Jerbi et al., 2009; Lachaux et al., 2012).

Until recently, the computational demands of multi-channel ECoG recording and spectral analysis were such that feedback to clinicians was unacceptably delayed. However, recent computing advances, including real-time data streaming and high performance multi-core workstations, have made it possible to provide online feedback. For example, a system called BrainTV (Lachaux et al., 2007b) can compute and display the modulation of several frequency bands during unstructured behavioral tasks, allowing highly flexible investigation of the

functional roles of individual sites. Another strategy for performing online mapping is to use a block design and characterize the difference between rest and active periods, most notably demonstrated in real-time by Miller et al. (Miller et al., 2007a), and by the SIGFRIED system (Schalk et al., 2008a) implemented within the BCI2000 framework (Schalk et al., 2004). A recent study by Cheung and Chang also demonstrated a system for providing real-time computation and display of spectrograms (Cheung and Chang, 2012). None of these systems, however, provides a trial-based framework for real-time display and statistical validation of temporally evolving high gamma power.

Here we introduce and test the feasibility and utility of an online trial-based system for spatial-temporal functional mapping (STFM). The STFM system enables visualization of the temporal evolution of functional activation at all ECoG sites during discrete tasks. This system updates and displays statistically thresholded trial-averaged or single trial high gamma power changes relative to baseline. The baseline distribution for these comparisons is collected between trials, so that the system can compensate for drifting arousal. This obviates the need to collect a separate rest interval, during which the patient's cognitive state is less controlled. An intuitive display and user interface allows experimenters or clinicians to select times (i.e., relative to cue) for displaying the spatial map of activation or to switch between trial-averaged and single trial rasters.

In a series of seven patients, we found that online STFM had sufficient temporal resolution to identify sites involved in distinct stages of commonly used language tasks. Additionally, estimates of the system's sensitivity and specificity

relative to the benchmark of ESM were the same or better than previous reports comparing ECoG mapping and stimulation mapping for language tasks (Bauer et al., 2013; Cheung and Chang, 2012; Ruescher et al., 2013; Wu et al., 2010). Moreover, we found that relative to regions of interest where cortical lesions most reliably cause language impairments, the sensitivity of STFM was significantly greater than that of ESM, and the specificity of STFM appeared greater than that of ESM, though the latter difference was not statistically significant.

2.3 Materials and Methods

2.3.1 Patient and Clinical Settings

Seven English-speaking patients (see Table 2.1) with intractable epilepsy underwent placement of subdural electrodes in the dominant hemisphere to localize their ictal onset zone and to identify language and motor areas using ESM. The implanted electrodes consisted of arrays (grids and/or strips) of macro electrodes (2.3mm exposed diameter, 1cm center-to-center spacing, Adtech, Racine, WI or PMT Corp, Chanhassen, MN). In five of seven patients, the macroelectrodes were supplemented by 4 x 4 arrays of microelectrodes (75micron diameter, 0.9mm spacing, PMT Corp, Chanhassen, MN) inserted into perforations in a grid of macroelectrodes. In all patients, the anatomical placement of electrodes was dictated solely by clinical considerations, which is for recording seizures and/or mapping cortical function. Patients were admitted to the Johns Hopkins Epilepsy Monitoring Unit after electrode implantation for a period of 6-14 days. All subjects

gave informed consent to participate in research testing under a protocol approved by the Institutional Review Board of the Johns Hopkins Medical Institutions.

Patient Number	Age	Gender	Handedness	Hemisphere dominance for language, Wada test (Davis and Wada, 1978)	Hemispheric Coverage	Seizure onset zone
1	23	F	Right	Left	Left	Anterior temporal
2	13	F	Right	Left	Left	Amygdala
3	55	M	Right	Left	Left	Anterior temporal
4	22	M	Right	N/A	Left	Occipital
5	62	M	Right	N/A	Left	Anterior temporal
6	25	M	Right	N/A	Left	Frontal
7	55	F	Right	Left	Left	Anterior temporal

Table 2.1. Patient Demographic and Clinical Information

2.3.2 Experimental Testing and Event Markers

In this study, the STFM system performed online functional mapping during two distinct behavioral tasks. In the visual object naming task, subjects were shown a picture stimulus on a monitor directly in front of them during each trial. Subjects were instructed to speak the name of the object in the picture, or say “pass” if they could not recall the name. In the auditory word repetition task, subjects were played an audio recording of a spoken word through insert earphones designed to attenuate external background noise during each trial. Subjects were instructed to verbally repeat the cued word. Subjects completed a range of 55-251 trials of visual object naming and 96-116 trials of auditory word repetition, where the number of trials was governed by the time constraints on patient testing and the set of stimuli used.

We detected the onset of picture stimuli by recording the thresholded digital output of a photodiode mounted on the computer monitor presenting the stimuli. In each trial, the photodiode detected a reduction in luminance that occurred when a

small black square appeared at the bottom left corner of the screen during presentation of the visual stimulus. In the auditory word repetition tasks, we detected the onset of acoustic stimuli by transmitting TTL pulse triggers synchronized with the onset of the auditory stimuli in a separate channel. This was implemented with a high-end psychoacoustics workstation (model Z6A, Tucker-Davis Technologies, Alachua, FL). The STFM system presented here was not hardcoded to receive these stimuli, but rather was designed to be flexible with respect to the functional tasks (and thus stimuli) used for mapping. The only requirement for trial-based mapping is that temporally accurate signals marking behavioral events can be recorded along with ECoG to ensure synchronization of ECoG analysis with relevant behavioral events. The system allows the user to adjust parameters for stimulus DC offset, threshold, and latency.

2.3.3 Electrode Localization

Electrode locations were identified in a high-resolution post-operative brain CT; electrode locations were then transformed onto a high-resolution pre-operative brain MRI by volumetrically co-registering the pre- and post-operative scans in Bioimage Suite (Duncan et al., 2004). Since some of the patients studied in this report had electrodes implanted over their basal temporal lobes, multiple viewpoint snapshots were aggregated into a single image for these patients so that all electrodes could be visualized simultaneously. Electrode locations were manually tagged on these images for subsequent display of online STFM results. The system

presented here is designed to accommodate any image of the electrodes with a corresponding list of electrode locations for visualizing the STFM results.

2.3.4 Data Acquisition and Analysis

Recordings of all standard ECoG macroelectrodes were referenced to a single intracranial macroelectrode to minimize extracranial sources of artifact. ECoG microelectrodes were referenced to a single microelectrode on the opposite side of the same insert, facing the dura mater. Raw ECoG signals were recorded with a 128-channel NeuroPort System (BlackRock Microsystems; Salt Lake City, UT) which amplified and sampled the data at 30 kHz with an analog third-order Butterworth anti-aliasing filter. The recordings for Patient 1 were sampled at 30 kHz, but for all other patients, the anti-aliased 30 kHz recording was downsampled to a lower rate (1 kHz, Patient 5; 2 kHz, Patient 2; 10 kHz, Patients 3, 4, 6, 7). This data was streamed using the built-in real-time streaming functionality of the NeuroPort system. The streaming data was immediately decimated to 1 kHz online in all patients prior to any subsequent analysis.

Channels with excessive amounts of noise were identified by a clinical neurophysiologist and excluded from analysis prior to online ECoG mapping. The remaining channels were re-referenced using a common average reference (CAR) to remove spatial bias in the raw ECoG amplitudes. Separate CAR blocks were used for: (1) all the macroelectrodes in each patient, and (2) each microelectrode array (in Patients 1, 3, 4, 5 and 6).

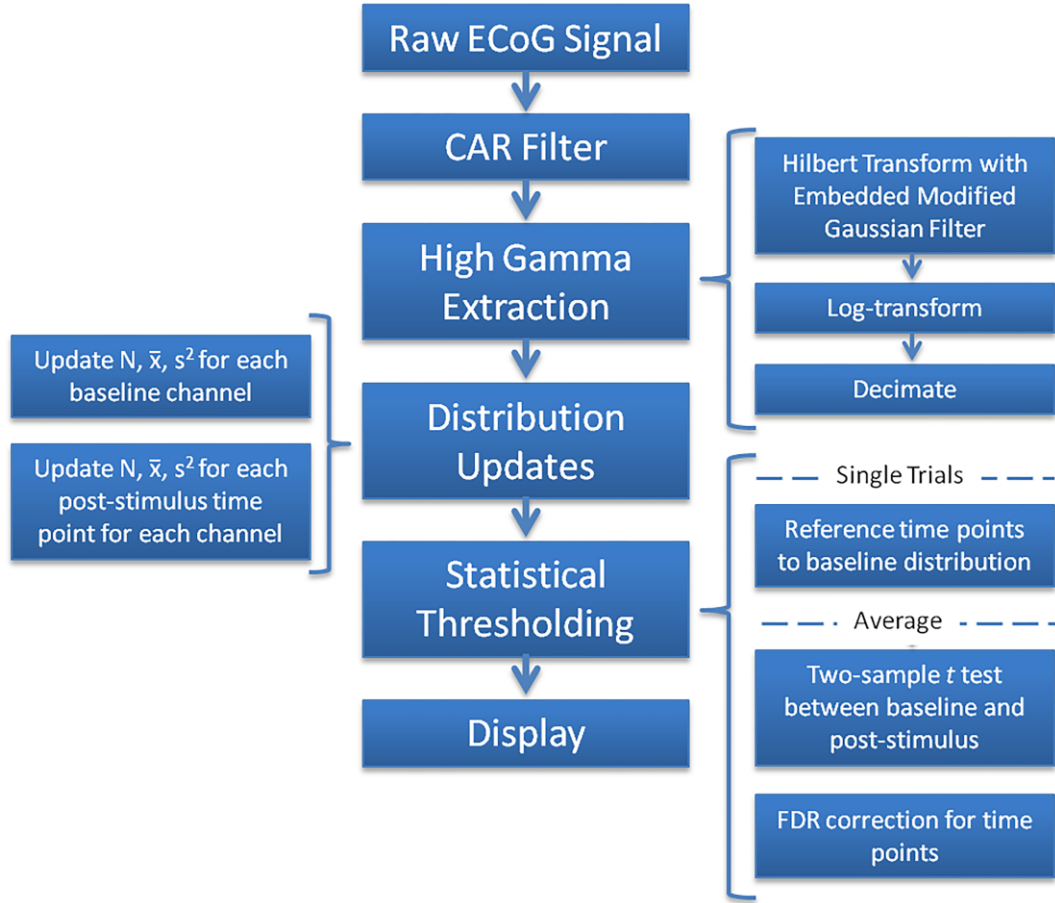


Figure 2.1. Online STFM Signal Processing Algorithm. A visual schematic is presented to describe the online signal processing and statistical methods used. A more detailed description of each step can be found in Section 2.3. N , \bar{x} , and s^2 represent sample size, mean, and variance, respectively.

2.3.5 Online Spectral Feature Extraction

The CAR-referenced ECoG signal was analyzed for the duration of the task in 512 ms epochs of data with 256 ms overlap (Patient 1) or 128 ms epochs of data with 112 ms overlap (other patients). The Fast Fourier transform (FFT) was computed on each window, and the resulting coefficients were then multiplied by a modified flat-top Gaussian window with cutoff between 67-115Hz (Patient 1) or 72-110 Hz (other patients) to minimize noise at 60 Hz and 120 Hz. The bandpass-filtered spectrum was converted to high gamma amplitude by zeroing the negative

frequency components, doubling the positive frequency components, computing the inverse FFT, and taking the magnitude of the result (i.e. the Hilbert transform) (Bruns, 2004; Canolty et al., 2007). The right column of Figure 2.1 shows the spectral feature extraction process in block diagram form. The resulting high-gamma amplitude was then log transformed to approximate a normal distribution and decimated to a temporal resolution of 16 ms using a moving average filter. Figure 2.2 shows the signal at several key points in this process.

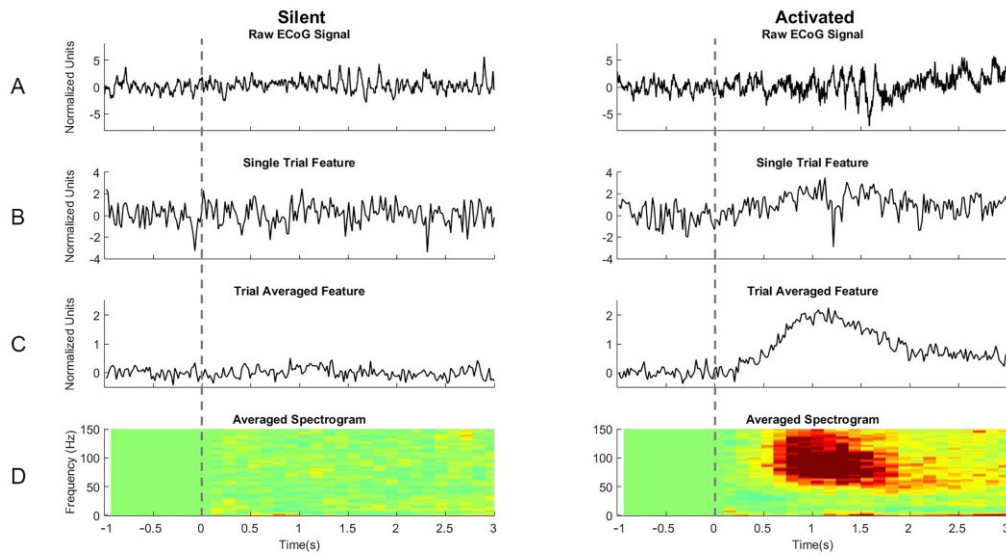


Figure 2.2. Feature extraction algorithm illustration from auditory word repetition in Patient 1. The ‘Silent’ column plots are from a macroelectrode (LFT33 in Figure 2.3B) that had no significant task-related high gamma response. The ‘Activated’ column plots are from a microelectrode (PMIC13 in Fig 3B) with a significant task-related high gamma response. In (A)-(C), the units have been normalized so that the baseline period has zero mean and unit standard deviation. (A) Raw ECoG signals from the same single trial are shown after re-referencing to the common average reference (CAR). (B) The high gamma amplitude feature is shown after it was extracted from the same single trial shown in (A) using the algorithm described in Figure 2.1. (C) Post-stimulus high gamma amplitude averaged across all 96 trials of auditory word repetition is shown for both electrodes. (D) The average post-stimulus spectrogram is shown, calculated by averaging the FFT coefficients time-locked to the stimulus marker in 512 ms bins with 256 ms overlap. Time zero is the stimulus onset of each trial. This spectrogram

is not shown to the system user online, but is included here only for comparison with the feature output.

2.3.6 Online Statistical Analysis

The time series of log-transformed high-gamma amplitude estimates, extracted as described above, was segmented separately into baseline and task-activated distributions. The baseline distribution for each channel was drawn from 64 samples of the analytic amplitude, corresponding to 1024 ms prior to stimulus onset (i.e., 16 ms resolution \times 64 points = 1024 ms). A separate task-activated distribution was estimated for each channel and time point after stimulus onset (i.e., 3072 ms in this study, with 16 ms resolution, for 192 total time points per channel). The baseline and task-activated amplitude distributions were approximated as Gaussian, parameterized by the sample size, mean, and variance, and were updated after each trial according to the following equations:

$$n_{new} = n_{old} + \Delta n \quad (1.1)$$

$$\bar{x}_{new} = \frac{\sum_{i=n_{old}+1}^{n_{new}} x_i + \bar{x}_{old} n_{old}}{n_{new}} \quad (1.2)$$

$$s^2_{new} = \sum_{i=n_{old}+1}^{n_{new}} x_i^2 + \left(\frac{n_{old}-1}{n_{old}} s_{old}^2 + \bar{x}_{old}^2 \right) \frac{n_{old}}{n_{new}-1} - \bar{x}_{new}^2 \frac{n_{new}}{n_{new}-1} \quad (1.3)$$

where n_{old} and n_{new} are the previous and current sample size, \bar{x}_{old} and \bar{x}_{new} are previous and current sample mean, and s^2_{old} and s^2_{new} are the previous and current sample standard deviations after update.

For trial-averaged activation maps, a two-way t -test was performed between the accumulated amplitude distribution from all baseline time points in each channel, and the accumulated amplitude distribution from each time point after stimulus onset in that same channel. The threshold for significance was determined using the false discovery rate (FDR) correction (Benjamini and Hochberg, 1995), where the two-sided significance threshold of $\alpha < 0.05$ was adjusted for m positively correlated tests, where m was the number of time points after stimulus onset. Each statistically significant difference from the baseline distribution was also tagged as an increase or a decrease in high gamma amplitude. Single trial results were computed similarly, but with a simple two-sided z -test with a threshold of $\alpha < 0.05$ uncorrected for multiple comparisons.

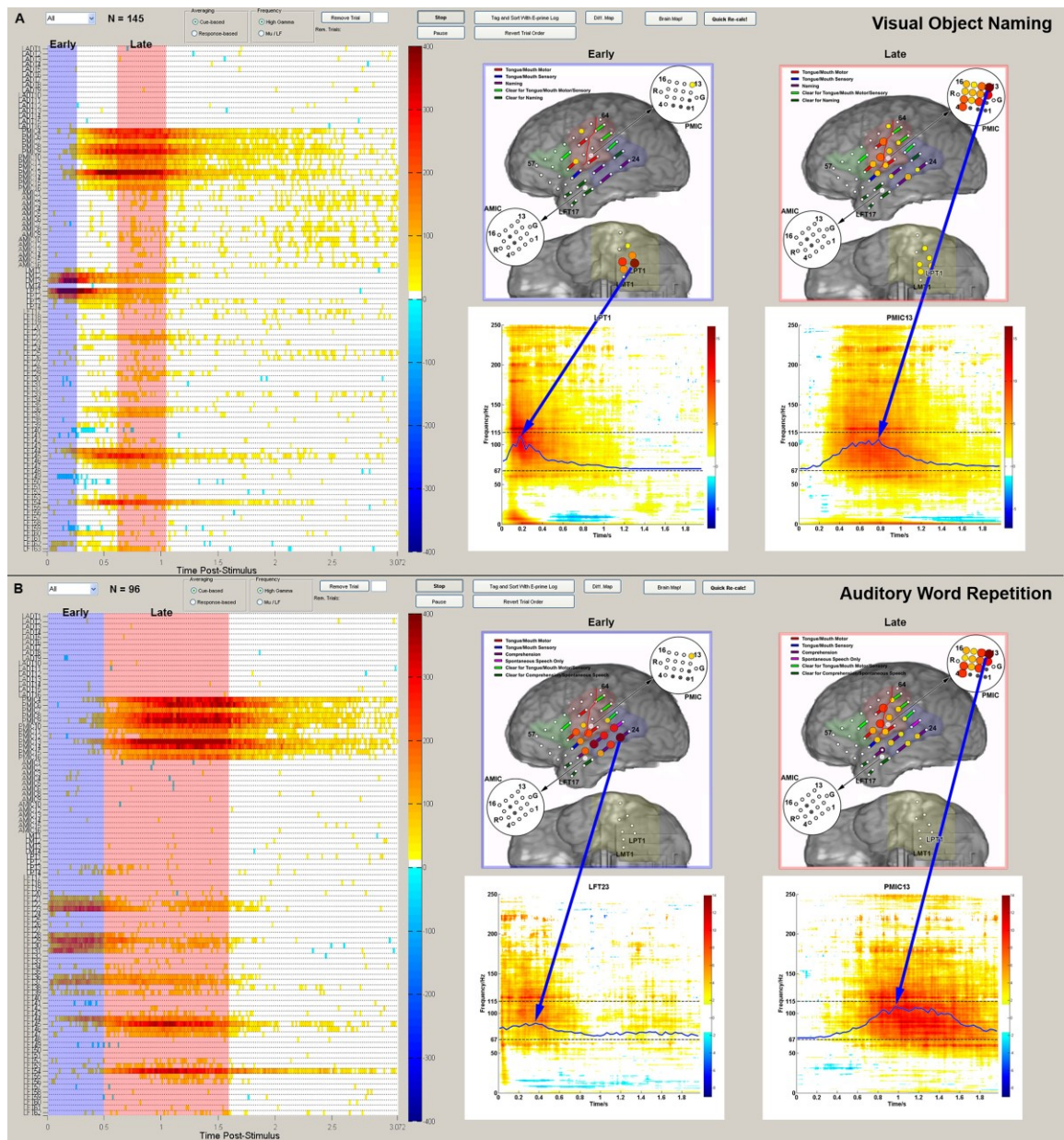


Figure 2.3. STFM of visual object naming (A) and auditory word repetition (B) in Patient 1. STFM results are shown as a raster of high gamma responses on the left, and as brain maps of high gamma response magnitude (represented by disc size and color) on the right. ESM maps (colored bars between electrodes) are also shown. Color-shaded areas denote anatomical boundaries of classical language areas used as regions of interest (ROI) in ROI sensitivity/specificity analysis. Color plots from offline matching pursuit analysis are illustrated below the brain maps for selected electrodes. Each raster plot displays the spatial-temporal distribution of significant increases (red spectrum) or decreases (blue spectrum) in high gamma energy relative to pre-cue baseline in 16 ms windows. Each row corresponds to a different electrode as displayed on the right brain maps. All times are relative to cue onset ($t=0s$). To highlight the spatial pattern of cortical activation at early

(visual/auditory perception) and late (response production) stages, high gamma responses are integrated across an early and late temporal window (early stage highlighted in red and late stage in blue on raster plot), and shown in separate brain maps (early stage in the left brain and late stage in the right brain). Microelectrode arrays AMIC and PMIC are enlarged for better visualization of high gamma responses. The matching pursuit spectrograms are overlaid with line plots (blue) of online high gamma responses of respective electrodes averaged over trials. Matching pursuit spectrograms, arrows pointing to spectrograms, second brain image, and highlighting of early and late time periods on the channel raster have all been added to the screenshot post hoc (i.e., they are not available online).

2.3.7 Raster Visualization

Raster plots (Figure 2.3) display the magnitude of event-related changes in the high gamma amplitude at each time point after stimulus onset, as compared to the baseline. These rasters display either trial-averaged amplitude changes (Figure 2.3, rows represent electrodes) or single-trial amplitude changes (Figure 2.6, rows represent trials). The magnitudes are thresholded for significance ($p < 0.05$) using FDR in the channel raster and are uncorrected in the trial raster. Each trial raster (Fig. 6) has a row at the bottom with the FDR-corrected estimate of activation aggregated from all trials (identically displayed on the channel raster, Fig. 3). A trial counter is displayed at the top of each raster for reference, and the rasters are updated after each trial. A dropdown menu allows users to view the channel raster or the trial raster from any of the channels. Supplemental Video 1 shows the evolution of the statistically significant high gamma responses obtained as the number of trials grew during a visual object naming task in Patient 1.

2.3.8 Brain Map Visualization

The magnitude of the high gamma response at a particular electrode and at a particular time is represented by the size and color of disks overlaid on ECoG

electrode locations in a two dimensional snapshot of the three dimensional brain reconstruction. This brain map can be displayed alongside the channel raster to show the locations and relative magnitudes of activations at any user-selectable time point or range of time points displayed in the channel raster. This is designed to facilitate clinical interpretation of time-varying cortical activity displayed by STFM. In addition, a button on the GUI can launch a short video in which the frames are snapshots of activation from the channel raster at sequential 16 ms time points.

2.3.9 Offline Time-Frequency Analysis

Offline time-frequency analysis using matching pursuits (MP) was performed with a custom C toolbox and Java interface (Franaszczuk and Jouny, 2004). A 1024 ms pre-stimulus baseline period was used as a basis for statistical comparison with 3072 ms of post-stimulus activity. A two-way, non-parametric Wilcoxon test was performed between every time-frequency pair and the baseline distribution of the corresponding frequency. The threshold for significance was determined similarly to online analysis by correcting for multiple comparisons across time and frequency using the FDR method to account for both time and frequency ($\alpha = 0.05$). The extent of modulation was displayed as a scaled color only if the activation was statistically significant.

2.3.10 ECoG Maps vs. Electrical Stimulation Maps

To investigate the degree of correspondence between STFM and ESM, the sensitivity and specificity of STFM was first computed using ESM as the gold standard. All ESM stimulation sites were listed as either ESM positive or negative

and as either STFM positive or negative. A site was marked STFM+ if it exhibited significant task-related high gamma power increase. A site was marked ESM+ if stimulation at this site inhibited language and/or inhibited or elicited movements or sensations in face, tongue, or mouth. At sites categorized as ESM+ by bipolar stimulation (stimulation between two adjacent electrodes), either electrode being STFM+ resulted in both electrodes being labeled as STFM+/ESM+, but only one of these electrodes was counted in our calculations of sensitivity and specificity. In this case, we reasoned, stimulation could have interfered with neural processing at either or both sites. In contrast, when pairs of electrodes were ESM- according to bipolar stimulation, each electrode was marked independently as either STFM+ or STFM-. STFM of visual object naming was compared with ESM of picture naming, while STFM of auditory word repetition was compared with ESM of comprehension and spontaneous speech. Auditory word repetition is not part of the standard battery of language tests used for ESM. Sensitivity and specificity were calculated separately for visual object naming and auditory word repetition, using the following equations:

$$Sensitivity = \frac{STFM_{+} / ESM_{+}}{STFM_{+} / ESM_{+} + STFM_{-} / ESM_{+}} \quad (2.1)$$

$$Specificity = \frac{STFM_{-} / ESM_{-}}{STFM_{+} / ESM_{-} + STFM_{-} / ESM_{-}} \quad (2.2)$$

2.3.11 Region of Interest Analysis

For each subject, we performed an anatomical region of interest (ROI) analysis to compare both ESM and STFM results to the regions where cortical

lesions most consistently impair language function. Task-relevant ROIs for auditory word repetition included Broca's area, sensorimotor cortex, and Wernicke's area, whereas the task-relevant ROIs for visual object naming included those from auditory word repetition in addition to the middle third of basal temporal-occipital cortex (yellow shaded areas in Figs 3, 4, and 5). The middle-third was adopted as a convenient and inclusive boundary for inclusion of higher order visual cortex responsible for visual object processing (Halgren et al., 1994; Nobre et al., 1994; Rangarajan et al., 2014; Tanji et al., 2005). For this analysis, Wernicke's area was defined as the posterior half of STG, supramarginal gyrus, and angular gyrus (blue shaded area in Figs 3, 4, and 5). Broca's area included pars triangularis and pars opercularis of the left inferior frontal gyrus (green shaded area in Figs 3, 4, and 5). Relevant sensorimotor cortex (red shaded area in Figs 3, 4, and 5) included pre- and postcentral gyri inferior to hand knob of central sulcus (red highlighted sulcus in Figs 3, 4, and 5).

Each stimulation site (i.e. monopolar or bipolar) was classified as ESM+ (positive) or ESM- (negative). Each monopolar stimulation site was either considered ROI+ when inside the ROIs, or ROI- when outside the ROIs; each bipolar stimulation site was considered ROI+ when at least one of the two electrodes, was inside the ROIs, and ROI- otherwise. Similarly, each monopolar stimulation site was considered STFM+ when the site exhibited a significant task-related high gamma power increase and STFM- otherwise; bipolar stimulation sites were counted only once and were considered STFM+ when at least one of the two electrodes was activated, and STFM- otherwise.

Using the classification of inside or outside language ROIs as a theoretical diagnostic standard, we calculated the sensitivities and specificities of STFM and ESM for all stimulation sites across all patients. Sensitivity was calculated as the proportion of stimulation sites in task-relevant ROIs correctly classified as positive. Specificity was calculated as the proportion of stimulation sites outside task-relevant ROIs correctly classified as negative. Tables 2a and 2b illustrate the STFM+/- and ESM+/- electrode counts for ROI+ and ROI- stimulation sites. Using these values, we calculated the sensitivities and specificities of STFM and ESM with the following equations:

$$Sensitivity(STFM) = \frac{STFM_{+} / ROI_{+}}{STFM_{+} / ROI_{+} + STFM_{-} / ROI_{+}} = \frac{a_1 + c_1}{n_1} \quad (2.1)$$

$$Sensitivity(ESM) = \frac{ESM_{+} / ROI_{+}}{ESM_{+} / ROI_{+} + ESM_{-} / ROI_{+}} = \frac{a_1 + b_1}{n_1} \quad (2.2)$$

$$Specificity(STFM) = \frac{STFM_{-} / ROI_{-}}{STFM_{+} / ROI_{-} + STFM_{-} / ROI_{-}} = \frac{b_2 + d_2}{n_2} \quad (2.3)$$

$$Specificity(ESM) = \frac{ESM_{-} / ROI_{-}}{ESM_{+} / ROI_{-} + ESM_{-} / ROI_{-}} = \frac{c_2 + d_2}{n_2} \quad (2.4)$$

McNemar's χ^2 test (McNemar, 1947) was performed to assess the statistical discordance of the sensitivities (Table 2.2a) and specificities (Table 2.2b) of STFM and ESM relative to language ROIs. A p -value under the acceptable level ($p < 0.05$) would mean that there is a statistically significant discordance of proportions of positive examinations between STFM and ESM among ROI+ stimulation sites.

Table 2.2a. Illustration of STFM vs. ESM test results among ROI+ stimulation sites			
	STFM+	STFM-	Row total
ESM+	a_1	b_1	$a_1 + b_1$
ESM-	c_1	d_1	$c_1 + d_1$
Column total	$a_1 + c_1$	$b_1 + d_1$	n_1

Table 2.2b. Illustration of STFM vs. ESM test results among ROI- stimulation sites			
	STFM+	STFM-	Row total
ESM+	a_2	b_2	$a_2 + b_2$
ESM-	c_2	d_2	$c_2 + d_2$
Column total	$a_2 + c_2$	$b_2 + d_2$	n_2

Table 2.2. Structure of STFM vs. ESM test results among ROI+ and ROI- stimulation sites

2.4 Results

2.4.1 Spatial-Temporal Functional Mapping can be Performed Online

Visual Object Naming

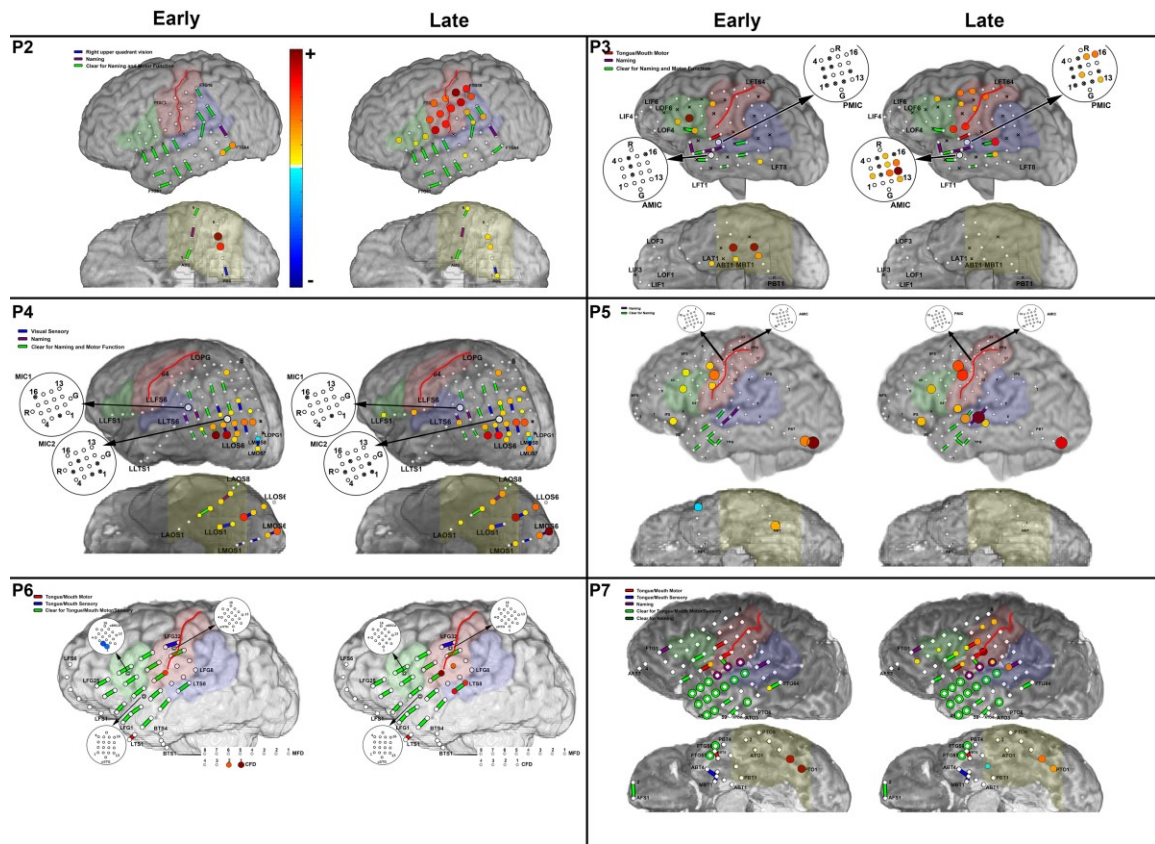


Figure 2.4. Visual object naming task results for Patients 2-7 (P2-P7). ESM and Online STFM results are overlaid on brain maps with highlighted ROIs. As in Figure 2.3, online results are separated into early stage (visual perception, left brain) and late stage (response production, right brain), where high gamma responses were computed by integrating across an early or late temporal interval. Microelectrode arrays are enlarged for better visualization.

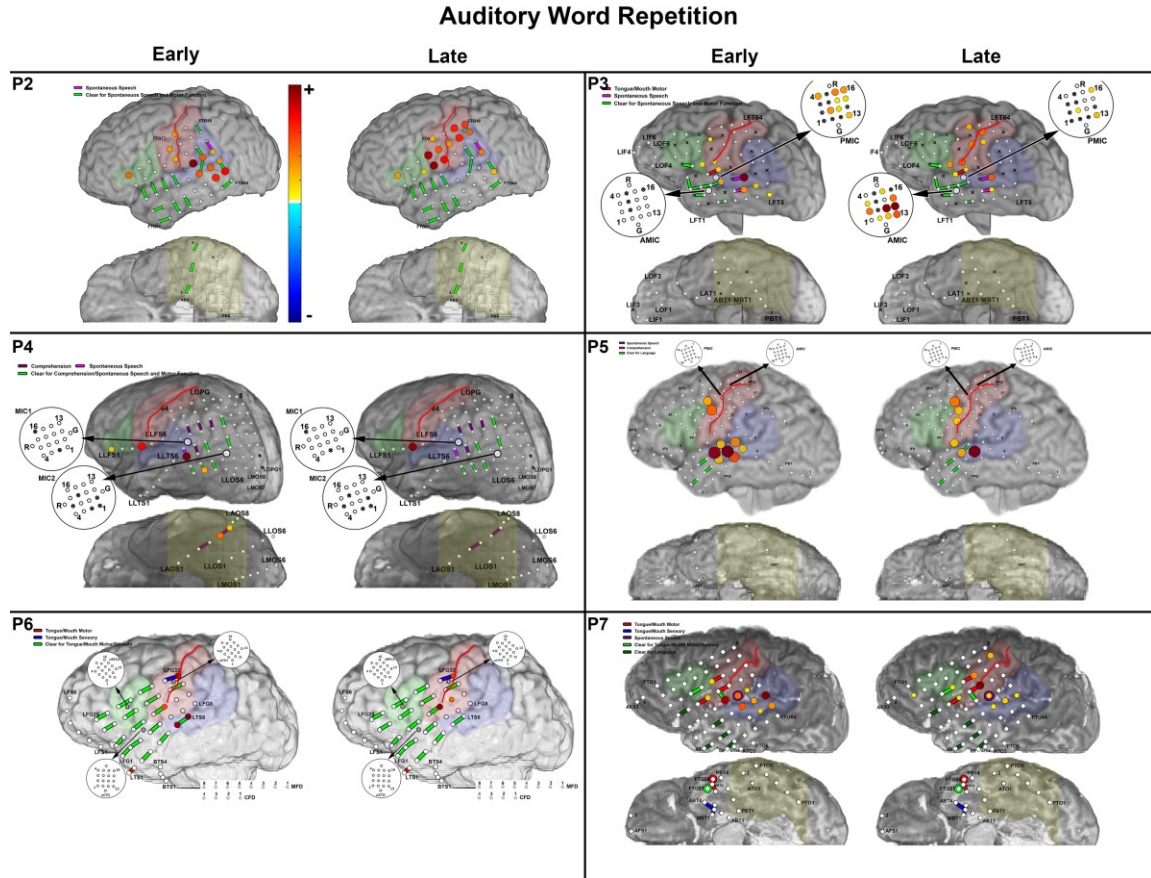


Figure 2.5. Auditory word repetition task results for Patients 2-7 (P2-P7). ESM and Online STFM results are overlaid on brain maps with highlighted ROIs. As above, online results are separated into early stage (auditory perception, left brain) and late stage (response production, right brain), where high gamma responses were computed by integrating across an early or late temporal window. Microelectrode arrays are enlarged for better visualization.

In all of our patients, our system successfully produced spatial-temporal functional maps (STFMs) of language function that could be reviewed online. Trial-based signal analyses, statistical testing, and STFM visualization were updated between trials. Supplemental Figure 2.1 shows an unmodified screenshot of the online STFM system. Modified screenshots of online STFM for visual object naming and auditory word repetition tasks in Patient 1 are shown in Figure 2.3. In each illustration, a screenshot of the channel raster of ECoG activation has been modified

to: a) highlight temporally clustered responses evident during online STFM, b) compare online STFM results to offline time-frequency analysis with matching pursuits, and c) compare online STFM to the results from electrocortical stimulation mapping (ESM). ROIs are also highlighted, including Wernicke's area, Broca's area, sensorimotor cortex, and basal temporal-occipital cortex. Simplified brain maps for Patients 2-7 are shown in Figures 4 and 5, with online STFM and ESM results from visual object naming and auditory word repetition tasks, respectively. Supplemental Video 2 shows the frame-by-frame temporal evolution of cortical activation associated the visual object naming task in Patient 1.

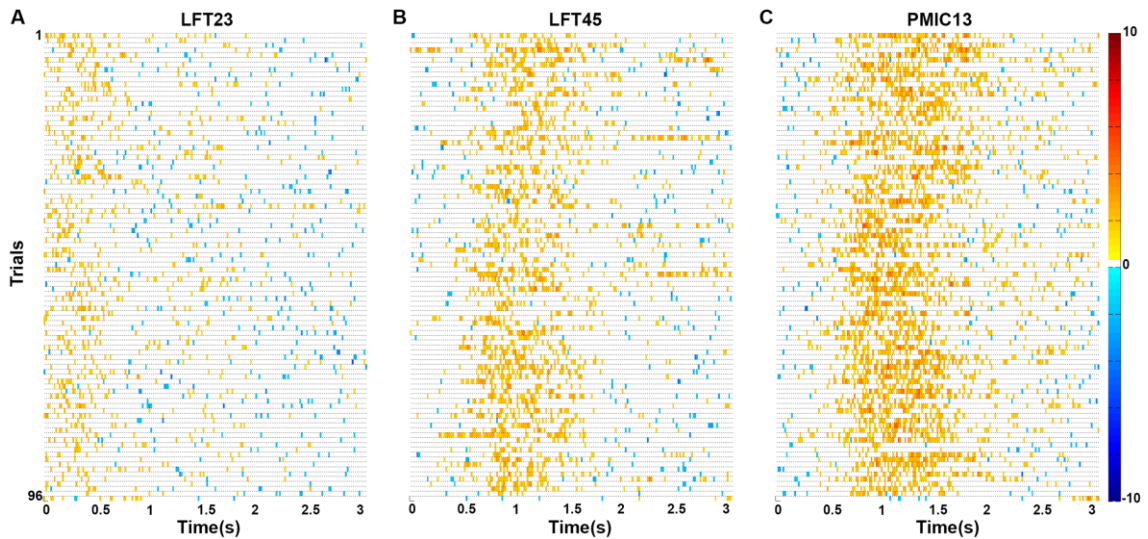


Figure 2.6. Single trial responses from online STFM results for Patient 1, auditory word repetition task. The single trial activations are shown for the auditory word repetition task in three separate electrodes: (A) LFT23, a macroelectrode in the early responding, putative stimulus perception cluster, (B) LFT45, a macroelectrode in the late responding, putative verbal response cluster, and (C) PMIC13, a microelectrode from the late responding cluster. The colors shown are scaled according to the negative log of the p -value, computed as a series of t -tests with the channel baseline distributions at the time of the trial. Significance thresholds have not been FDR corrected for multiple comparisons, as the single trial responses are primarily intended as an indicator of neural response consistency across trials.

Task-related high gamma responses were sufficiently robust to yield statistically significant responses in single trials. The online STFM system allowed these single-trial responses to be updated after each trial and to be displayed in a trial-by-time raster of ECoG activations. This provided additional insight into the robustness and consistency of the high gamma responses at individual ECoG recording sites. For example, single-trial responses are shown in Figure 2.6 for macroelectrodes that were activated in early and late phases (A and B, respectively) of the auditory word repetition task, and for a microelectrode (C) with activation similar to a late temporal cluster of activation in the macroelectrodes.

Measures of ECoG high gamma responses from STFM closely corresponded to time-frequency analyses performed with offline matching pursuits analysis. Representative individual channels were chosen for display from both the early and late responding channel-clusters in each patient, but in general there was very high correspondence between the online STFM results and the envelope of high gamma spectral energy estimated via matching pursuits, as demonstrated in Figure 2.3.

2.4.2 Spatial-Temporal Functional Maps are Task-Specific

In all our patients, online STFM revealed the temporal evolution of activation across all ECoG recording sites. As expected, the different components of each patient's cortical language networks were activated with different temporal envelopes, resulting in complex, cascading spatial-temporal patterns of activation. When the STFMs for different language tasks were compared, their differences appeared to reflect the contrasting processing demands of the tasks.

Visual object naming requires visual processing to identify the object to be named. The most basic processing of the visual stimulus is expected to occur at the earliest post-stimulus latencies in cortex around the occipital pole, near calcarine cortex (as in Patient 4, Figure 2.4c). Higher-order processing of object features, identity, and perhaps semantic information is expected to occur later and further downstream in the visual object processing stream in basal temporal-occipital cortex (as in Patient 1, Figure 2.3a). To highlight the spatial pattern of cortical activation at early latencies in Figure 2.3, we integrated statistically significant high gamma responses across an early interval (a parameter that can be customized ad hoc in the system) and showed the locations of these responses in a separate brain map (highlighted in blue on channel raster and with size-and-color-scaled discs in the brain maps to the right of the raster). In general, the earliest activations we observed during this task occurred in the aforementioned anatomical regions.

Visual object naming also requires retrieval of lexical representations for identified objects and transformation of these into articulatory codes that are implemented by motor cortex. Based on data from lesion analysis, psychophysics, and neuroimaging, these processing stages are implemented in a perisylvian frontal-temporal network that includes Broca's area, Wernicke's area, and sensorimotor cortex, controlling the muscles of articulation. To highlight these stages of task processing, we integrated high gamma responses across a later temporal window and showed the locations of these responses (highlighted blue on channel raster and brain maps on the right). In general, the significant responses in this timeframe were greatest over ventral premotor and sensorimotor cortices, likely

corresponding to oral-facial representations activated in preparation for and during articulation.

During articulation, we also observed activation of posterior superior temporal gyrus (pSTG). This activation has been observed in previous studies (Crone et al., 2001a; Edwards et al., 2010; Flinker et al., 2010a) and likely corresponds to monitoring of self-generated acoustic speech stimuli. Note that activation during this timeframe had an anatomical distribution similar to the one observed during the auditory word repetition task, consistent with the common demands of the two tasks during articulation. In some cases, we also observed activation of posterior inferior frontal gyrus (Broca's area) and posterior middle and inferior temporal gyrus. These activations generally occurred at latencies intermediate between those attributable to visual object processing and articulation, likely reflecting processes responsible for retrieval of lexical and phonological representations for the spoken responses.

Auditory word repetition requires perceptual decoding of the auditory stimulus, typically occurring in posterior STG and nearby perisylvian cortices, followed by transformation into an articulatory code. In all our patients the earliest activation, almost immediately after onset of the auditory stimulus, was localized to auditory association cortex in superior temporal gyrus (STG), consistent with the role of this cortical area in speech perception (Boatman et al., 1997; Crone et al., 2001a; Nourski and Howard III, 2015). A subset of these early-responding macroelectrodes were also activated later, albeit to a smaller degree, likely corresponding to self-monitoring of spoken responses, as mentioned above. A late

cluster of activation occurred in ventral sensorimotor cortex during articulation of spoken responses.

2.4.3 Micro-ECoG vs. Macro-ECoG Responses: Similarities and Differences

The overall response patterns within micro-ECoG arrays were consistent with those of macroelectrodes, and both were consistent with task-related processing demands. However, high gamma responses within micro-ECoG arrays were often more robust than those recorded from macroelectrodes. This was most evident in single-trial responses, in which statistically significant responses occurred more consistently across time windows and across trials (Fig 6). This could have been due to greater temporal and functional homogeneity in population responses recorded from microelectrodes than those recorded from macroelectrodes. Micro-ECoG arrays sampled cortical activity from a surface area (2.7 mm²) only slightly larger than that of individual macroelectrodes (2.3-mm diameter). One might expect that task-related cortical activation at this scale would be highly correlated among adjacent microelectrodes, resulting in highly uniform spatial-temporal patterns of activation. However, in many instances we observed a surprising degree of heterogeneity in the temporal and spatial patterns of activation at different microelectrodes within individual micro-ECoG arrays.

For example, during auditory word repetition in Patient 1, the microelectrode array over ventral post-central gyrus (PMIC, Figure 2.3a) showed robust responses with substantial heterogeneity in their onsets and magnitudes;

collectively, these activations were similar to nearby macroelectrode responses, occurring before and during spoken responses, albeit with onset latencies about 300 ms earlier. Activation of this region during spoken responses has been reported in other studies (Crone et al., 2001b) and likely reflects motor commands to and sensory feedback from the muscles of phonation and articulation. The responses from this high-density array during auditory word repetition were also noteworthy in the heterogeneity of their onset latencies, which could have been attributable to either true differences in latencies at each electrode or an artifact of the statistical thresholding process in which stronger activations would appear to have earlier onsets. Regardless of the true reason for the different onset times, this variation suggests some degree of functional-anatomic selectivity at this scale. The microelectrode array over anterior middle temporal gyrus (MTG) in Patient 1 was inactive during auditory word repetition but showed late, temporally dispersed activity during visual object naming, consistent with its neighboring macroelectrodes.

2.4.4 ECoG Maps vs. Electrical Stimulation Maps

STFM results for both visual object naming and auditory word repetition tasks for each patient were first computed by using ESM results as the gold standard (Table 2.3). The average sensitivity across tasks and patients was 69.9%, and the average specificity was 83.5%.

Comparison of STFM vs. ESM		
Patient	Visual Object Naming	Auditory Word Repetition

Number	Sensitivity (%)	Specificity (%)	Sensitivity (%)	Specificity (%)
1	100.0	94.4	100.0	78.6
2	33.3	69.2	100.0	78.6
3	75.0	62.5	100.0	77.8
4	85.7	65.0	28.6	92.9
5	100.0	90.0	100.0	100.0
6	0.0	90.3	50.0	90.3
7	50.0	92.3	55.6	86.7
Average	63.4	80.5	76.3	86.4

Table 2.3. Sensitivity and specificity values for STFM during visual object naming and auditory word repetition tasks, with ESM as the gold standard.

Tables 4a and 4b show STFM vs. ESM test results for both ROI+ and ROI- stimulation sites across all patients.

Table 2.4a. STFM vs. ESM test results among ROI+ stimulation sites			
	STFM+	STFM-	Row total
ESM+	37	9	46
ESM-	26	24	50
Column total	63	33	96

Table 2.4b. STFM vs. ESM test results among ROI- stimulation sites			
	STFM+	STFM-	Row total
ESM+	10	17	27
ESM-	7	89	96
Column total	17	106	123

Table 2.4. STFM vs. ESM test results among ROI+ and ROI- stimulation sites, across all patients

The sensitivity and specificity of both ESM and STFM using anatomical ROIs as a gold standard were calculated across patients, using Equations 2.1-2.4 and values from Table 2.4. The average sensitivity across tasks and patients was $63/96 = 65.6\%$ for STFM vs. $46/96 = 47.9\%$ for ESM; the overall average specificity was $106/123 = 86.2\%$ for STFM vs. $96/123 = 78.0\%$ for ESM.

We used McNemar's χ^2 test (Trujillo-Ortiz et al., 2004) to determine whether the sensitivities and specificities of STFM mapping were statistically different from those of ESM mapping, assuming our ROIs as a hypothetical gold standard, with a significance threshold of $p < 0.05$. We found that the sensitivity of STFM was significantly greater than that of ESM ($p = 0.0068$), while the specificity of STFM appeared to be greater than that of ESM, but this difference was not statistically significant ($p = 0.066$).

2.5 Discussion

Results from seven patients performing a variety of language tasks demonstrated that the spatial-temporal functional mapping (STFM) system is fast and robust enough to compute maps of cortical function for online review, using ECoG high gamma responses that correspond well to both ESM and offline MP analysis results.

The time-consuming and taxing nature of ESM motivates the development of a passive functional mapping alternative. We believe that online spatial-temporal functional mapping (STFM) based on event-related changes in ECoG signals provides important opportunities for clinicians and neuroscience researchers. The

clinical utility of STFM currently lies in both augmenting the findings from ESM and identifying the areas of potential functional significance as a guide to further exploration by ESM. STFM has the advantage of being performed at all recording sites simultaneously. Additionally, it can provide a graded measure of cortical activation that allows clinicians to estimate the relative contribution of different cortical sites to task performance. A recent study performing covert ECoG mapping of motor cortex (Vansteensel et al., 2013) shows that information about high gamma activation associated with spontaneous limb movements can be captured with minimal demands on patient cooperation. Our system could also be adapted to such a protocol using electronic sensors for detecting movement (e.g. with accelerometers) or speech (e.g. with microphones).

With a larger body of evidence, it may be possible to someday make clinical decisions from passive functional mapping alone. Brunner et al. (Brunner et al., 2009) performed a side-by-side comparison of ESM and STFM in motor cortex with favorable results (i.e. no false negatives, ~1% false positives). Mapping language cortex presents additional challenges, however, since multiple sites over large-scale cortical networks are involved. The temporal profile of activation at a given site and its timing relative to other sites could therefore provide insight into its function and contribution to a given task. For example, semantic knowledge is likely distributed broadly over temporal and frontal cortices (Mesulam, 1990) . Although some studies have indicated poor sensitivity and specificity of STFM in relation to ESM (e.g. specificity of 78% and sensitivity of 38% during visual object naming (Sinai et al., 2005)), a recent report has suggested that in some instances it can be more

predictive of post-operative language impairments than ESM (Cervenka et al., 2013, 2011). More work will be required to correlate surgical outcomes with the location of resected and preserved sites identified by ESM and STFM.

For the neuroscience researcher, STFM can provide preliminary maps of cortical function that allow subsequent experiments to be chosen intelligently. This customization is critical to maximize the relevance of an experimental battery in a setting where electrodes are implanted solely according to clinical need. It also allows both clinicians and researchers to immediately determine whether they have sufficient data to demonstrate statistical significance, especially useful in time sensitive environments, e.g. intra-operative functional mapping. Additional functions such as trial removal and single trial display allow users to better observe the results and optimize their experiments during testing.

We feel that our STFM system offers advantages over real-time spectral feedback, as is provided in systems like BrainTV (Lachaux et al., 2007b). These systems provide flexibility to rapidly hypothesize and test the functional roles of cortex under a particular electrode. This flexibility allows for the exploration of non-traditional stimuli and enables clinical neuroscientists to perform experiments analogous to single unit recordings for discovering the tuning of neural signals to stimulus or behavioral parameters. However, interpretation of the results requires an expert to simultaneously monitor the patient and the real-time spectral feedback to detect functional responses at individual recording sites, all while generating and testing hypotheses for each site.

Previous systems have also employed block-based online functional mapping schemes (Miller et al., 2007a; Schalk et al., 2008a). Although block-based functional mapping is capable of providing a single metric for quantifying gross contribution to a task (i.e., which is desirable to be comparable to ESM), it lacks the ability to precisely map complex cortical activations that evolve over time. A trial-based scheme allows for coarse spatial maps of task-relevance to be decomposed into temporal sequences of activation with greater functional anatomical discrimination among activated sites. This segmentation allows activated sites to be compared by their relative contribution to each temporal stage of activation without having their estimated contributions scaled by the relative duration of each stage to which they contribute.

Compared to existing ECoG functional mapping systems, our STFM system offers several key advantages. First, our trial-based system constructs a baseline distribution from the pre-cue phases of individual trials, rather than a pre-session block of baseline activity, as employed by previous studies (Brunner et al., 2009; Cheung and Chang, 2012; Lachaux et al., 2007b). In our opinion, the pre-cue baseline provides the best control for active periods because it controls for variations in the arousal and attentiveness of the patient that are not directly related to the experiment. Trial-based analyses also provide greater cognitive control during both the baseline and the active period. In a block design, by contrast, it is difficult to ensure that a patient is continuously performing an experimental task during a long active period without contaminating this period with unintended cognitive events or brief rest periods.

The second major, and perhaps most important, advantage of an STFM system is that it can elucidate the temporal evolution of cortical activation. This becomes particularly important for interpreting cortical activation during complex, multifaceted tasks, including most language tasks. Without information about the timing of activation relative to behavior, one can only speculate about the contributions that different activated sites make to the different facets of these tasks. The timing of activation at each site allows one to make more informed hypotheses about the functional contribution of that site to task performance. For example, of the many sites activated during a particular task, there may be sites with task-related activation that is time-locked a) only to the cue, b) only to the behavioral response, or c) to both the cue and behavioral response. The magnitude of activation at each site can then be more accurately understood as the degree of activation during certain phases of task performance. In contrast, integration of activation over the entire trial, or during an active period with repeated trials, would emphasize electrodes with a longer temporal envelope of activation.

The addition of timing information admittedly increases the complexity of interpretation over that of a single metric of activation. To attempt to mitigate these difficulties, the system includes the ability to click on the channel raster to visualize a time-specific snapshot of brain activation. The resulting brain maps provide an intuitive display with labeled electrodes that are colored and sized according to the magnitude of activation. In addition, these maps can be aggregated into a video to visualize the spatial-temporal evolution of brain activation.

During language testing with our STFM system, we observed rich single trial responses, especially in the microelectrodes (see Figure 2.4). The signal quality of ECoG signals is much higher than that of scalp EEG, particularly for high gamma activity (Ball et al., 2008). This allows not only better spatial sampling of activated neuronal populations, but also high gamma responses that are sufficiently robust to be detected in single-trial analyses (Flinker et al., 2010b). Single-trial high gamma responses can be leveraged for a variety of purposes, including brain-computer interfaces (Schalk and Leuthardt, 2011) and online functional mapping (Lachaux et al., 2007b). In addition, they can provide richer correlations with behavior. For example, single trial responses can be used to study inter-trial variability in a given task; if sorted properly, single trial responses can reveal differential neural responses to different categories of behavioral stimuli or responses. Variations in the patient's attention to a task can also be observed in single trials so that encouragement or further instructions can be given to improve performance and map accuracy. Single trial responses can therefore be a powerful tool for the experimenter when it is otherwise difficult to monitor adherence to a task (e.g., motor imagery or imagined speech).

ECoG vs. ESM in previous studies					
Author	Year	Frequency Band (Hz)	Task	Sensitivity (%)	Specificity (%)
Wu et al.	2010	75-100	Language	71.0	59.9
Cheung et al.	2012	61-260	Motor/Speech	70.8	78.1
Ruesher et al.	2013	60-400	Speech	18.9	96.7
Bauer et al.	2013	69-95	Language	20.3	85.0

This paper	2015	70-110	Language	69.9	82.5
------------	------	--------	----------	------	------

Table 2.5. Comparison of sensitivity/specificity calculation for different studies

Previous studies of ECoG mapping using the high gamma frequency band have shown comparable, if slightly lower, sensitivities and specificities relative to ESM (Table 2.5) (Bauer et al., 2013; Cheung and Chang, 2012; Ruescher et al., 2013; Wu et al., 2010). These studies have all assumed that ESM is the gold standard for identifying eloquent cortex and predicting post-resection deficits. For this, the real gold standard would be post-operative outcome following resection of a cortical site. However, this is difficult, if not impossible, to achieve in clinical practice because resections always include more than one site and because reorganization of function inevitably takes place following resection. For these reasons and others, no other method has proved better than ESM to date. However, concerns about the accuracy of ESM can be traced back to its inception in clinical practice (Cushing, 1908; Penfield and Boldrey, 1937). It has long been recognized that cortical stimulation can affect function at a distance (Hamberger, 2007), and that ESM does not always predict post-operative language outcomes (Cervenka et al., 2013, 2011; Krauss et al., 1996). This concern is perhaps best illustrated in somatosensory and motor cortices where the effects of lesions are more predictable. Although stimulation of post-central gyrus often elicits motor responses, resection of this gyrus causes sensory impairments and apraxia, but not weakness per se (Nii et al., 1996; Penfield and Boldrey, 1937). Conversely, stimulation of pre-central gyrus can elicit somatic sensations. Indeed, clinical investigators have elicited movements with stimulation 1.5-4.7 cm anterior and 2 to 3.4 cm posterior to the central sulcus, but resection of

most of this territory can be performed with little or no motor impairment (Nii et al., 1996; Penfield and Boldrey, 1937). Indirect evidence for distant effects of ESM can also be found in studies in which direct cortical stimulation has elicited both evoked responses (Matsumoto et al., 2007, 2004) and high gamma responses (Matsuzaki et al., 2013) in distant cortical regions that have putative functional connectivity with the stimulation site. Because high gamma responses reflect population firing rates (Manning et al., 2009; Ray et al., 2008a), the latter study suggests that ESM can affect neuronal firing in distant populations, though the impact on cortical function is not known.

Because of the potential inaccuracies of ESM for functional localization, we believe it is important to evaluate the accuracy of both ECoG and ESM with respect to an independent measure of cortical function. This must necessarily be drawn from the rich literature on the effects of brain lesions (Hickok and Poeppel, 2007; Damasio and Geschwind, 1984; Damasio, 1991), as well as on regions typically activated on fMRI during experimental language tasks, albeit at far lower temporal resolution (Buchsbaum et al., 2001; Hickok and Poeppel, 2007; Price, 2000). Using this approach we found that the sensitivity of STFM was significantly greater than that of ESM, while the specificity of STFM was greater than that of ESM, though not significantly so. In light of these findings, we believe that both ESM and passive ECoG mapping offer approximations of the patient's true functional anatomy and that more studies are needed to understand their comparative utilities in clinical practice.

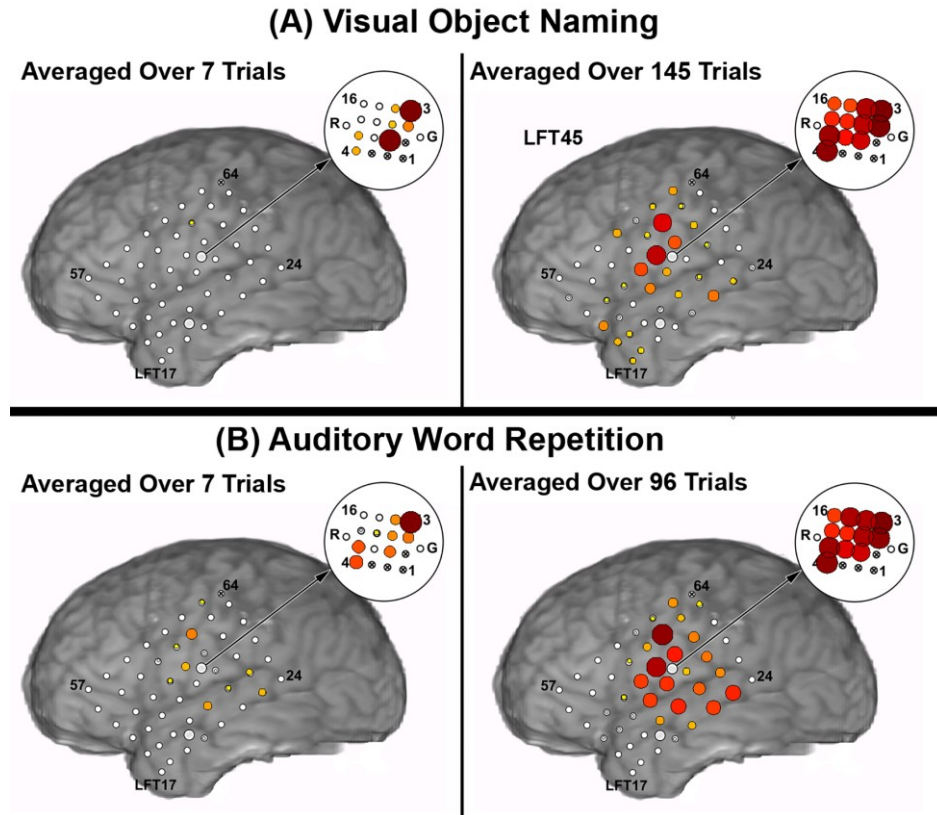


Figure 2.7. Microelectrodes record ECoG high gamma responses with fewer required trial numbers for both tasks in Patient 1. With only 7 trials averaged from a visual object naming task (A) or an auditory word repetition task (B), statistically significant high gamma responses appeared in the microelectrode array. Responses are either absent in the macroelectrodes or have lower magnitudes than the microelectrodes with the highest magnitude responses. A similar trend is seen with more trials (145 in A, 96 in B). Magnitudes of statistically significant high gamma responses are indicated by size/shading of red circles.

The STFM system presented here also allowed novel observations from microelectrode recordings in Patient 1. For example, statistically significant and stable high gamma responses emerged with fewer trials in activated microelectrodes than in neighboring activated macroelectrodes during visual object naming and auditory word repetition tasks (Figure 2.7). The greater robustness of high gamma responses in the microelectrodes could have been due to higher sensitivity to high frequency activity or greater spatial selectivity for activated

cortical populations. In contrast, macroelectrodes record from larger populations of neurons and are more likely to average activity from responding neurons with activity from neurons that do not respond or are inhibited. The spatial heterogeneity of the microelectrode responses observed in Patient 1 could not be explained simply by spatially interpolating between neighboring macroelectrodes. These findings are consistent with previous work highlighting the macrocolumn, with a size on the order of surface microelectrodes, as a functional subunit of the cortical gray matter (Mountcastle, 1997). ECoG functional mapping may be particularly useful for probing the functional role of cortex under arrays microelectrodes. While it is possible to perform ESM in microelectrodes, stimulation parameters and subsequent interpretation of the behavioral responses are not well chronicled; interpretation of ECoG mapping results in microelectrodes, however, relies on the same principles as that of macroelectrodes. This advantage of ECoG mapping over ESM is expected to be more relevant as the number and density of ECoG electrodes used for long-term monitoring increases, since ESM will become increasingly impractical and time-consuming in high-density ECoG arrays currently being developed for use in mapping the epileptogenic zone and in other clinical applications (Bouchard and Chang, 2014; Viventi et al., 2011).

In conclusion, we have demonstrated a system that is able to compute spatial-temporal functional maps (STFM) online, allowing for immediate access to ECoG mapping results at the patient's bedside. This system is designed to mimic offline high gamma functional mapping with concessions made only as necessary to satisfy computing and timing constraints. Our approach is generalizable to a variety

of clinical and experimental applications, as only a reliable marker of the stimulus and a trial-based design is required. Although not demonstrated here, this system could easily be adapted to the time-pressured circumstances of an awake craniotomy. At the same time, the system offers full visualization of the complex spatial-temporal dynamics of functional tasks of varying complexity. We believe that this information will help both clinicians and researchers better understand the contributions that tested sites make to task performance.

2.6 Study Acknowledgments

This work was supported by the National Institute of Neurological Disorders and Stroke (NINDS) Grant NS40596 and NS91139. We also thank the research participants that made this study possible.

Chapter 3

Simultaneous Neural Control of Simple Reaching and Grasping with the Modular Prosthetic Limb Using Intracranial EEG

3.1 Abstract

Intracranial electroencephalographic (iEEG) signals from two human subjects were used to achieve simultaneous neural control of reaching and grasping movements with the Johns Hopkins University Applied Physics Lab (JHU/APL) Modular Prosthetic Limb (MPL), a dexterous robotic prosthetic arm. We performed functional mapping of high gamma activity while the subject made reaching and grasping movements to identify task-selective electrodes. Independent, online control of reaching and grasping was then achieved using high gamma activity from a small subset of electrodes with a model trained on short blocks of reaching and grasping with no further adaptation. Classification accuracy did not decline ($p < 0.05$, one-way ANOVA) over three blocks of testing in either subject. Mean classification accuracy during independently executed overt reach and grasp movements for (Subject 1, Subject 2) were (0.85, 0.81) and (0.80, 0.96) respectively, and during simultaneous execution they were (0.83, 0.88) and (0.58, 0.88) respectively. Our models leveraged knowledge of the subject's individual functional neuroanatomy for reaching and grasping movements, allowing rapid acquisition of control in a time-sensitive clinical setting. We demonstrate the potential feasibility of verifying

functionally meaningful iEEG-based control of the MPL prior to chronic implantation, during which additional capabilities of the MPL might be exploited with further training.

3.2 Introduction

Reaching to and grasping objects is an important skill that forms the basis for many activities of daily living (ADLs). It is thus an important target for brain-machine interfaces (BMIs) being developed for patients with impaired limb function due to neurological lesions of motor pathways (e.g., spinal cord injury, amyotrophic lateral sclerosis, stroke, etc.). Recent work has demonstrated that grasp types (Pistohl et al., 2012), grasp timing (Pistohl et al., 2013), hand postures (Chestek et al., 2013), and reach parameters (Anderson et al., 2012) can be decoded from spectral changes in human intracranial electroencephalographic (iEEG) signals, and that movement-related spectral modulation of iEEG can be used for online control of BMIs, for example during dexterous grasping (Vinjamuri et al., 2011), when selecting between grasp types and elbow movement (Yanagisawa et al., 2012), or for three dimensional cursor control (Wang et al., 2013). We therefore sought to determine whether human iEEG could be used to provide simultaneous and independent online control of reaching and grasping movements, thus demonstrating segregation of these two movement types at the spatial scale of iEEG macroelectrodes. iEEG is an attractive platform for the development of BMIs because of the potential for better long-term signal stability than multi-unit recordings, as well as the availability of subjects who have accepted the risks of

electrode implantation for the mapping of their seizure onset zones prior to epileptic resection surgery (Leuthardt et al., 2006).

Relative to scalp EEG, iEEG provides better spatial resolution and better signal quality for high frequency activity (T. Ball et al., 2009; Freeman et al., 2000). There is substantial empirical evidence from local field potential studies in humans (Manning et al., 2009) and nonhuman primates (Ray et al., 2008a) that this high frequency activity closely tracks population firing rates. The degree of control that can be achieved with the large-scale population activity recorded with iEEG (Leuthardt et al., 2004; Schalk et al., 2008b) is unknown, however, especially with chronic training beyond the time constraints of seizure monitoring. To ensure that the risk of long-term electrode implantation is offset by the benefit of stable long-term BMI use, it would be advantageous to confirm at least basic control of the intended prosthetic at the time of implantation.

Previous work in scalp EEG and iEEG has demonstrated two- and three-dimensional cursor control where at least one dimension is controlled by behavior unrelated to the task at hand (e.g., vocalization or tongue movement) (Leuthardt et al., 2004; McFarland et al., 2010; Schalk et al., 2008b; Wolpaw et al., 1991). Although it has been demonstrated that training and “operant conditioning” can be used to learn BMI control on the time-scale of months (Rouse et al., 2013), it is unclear to what extent an unnatural mapping will scale up to more complex tasks in more complex environments. We therefore sought to determine whether the command signals for forward reaching and grasping of the Johns Hopkins University Applied Physics Lab (JHU/APL) Modular Prosthetic Limb (MPL) could be derived

from high frequency (70-110 Hz) neural population activity associated with naturalistic reaching and grasping movements, respectively. These commands were interpreted by the hardware in the MPL and converted to multi-axial anthropomorphic movements spanning two controllable joints for forward reaching and 10 controllable joints for grasping.

3.3 Methods

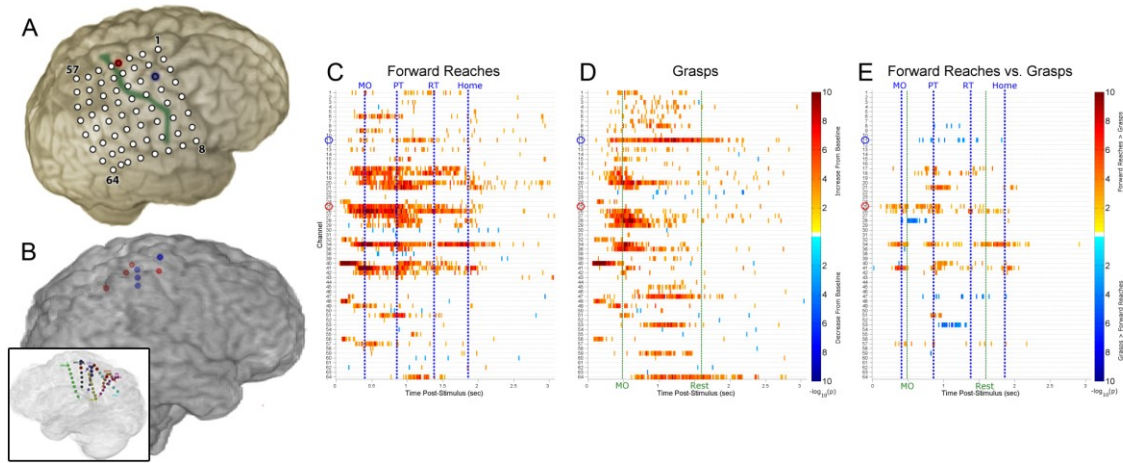


Figure 3.1. Functional mapping of cue-averaged task-related high gamma activity in training set. (A) Reconstruction of the implanted grid location for Subject 1 is depicted; the electrode used for reaching (number 25) is highlighted in red and corresponds to the channel circled in red in the activation maps below, while the electrode used for grasping (number 11) is highlighted in blue and similarly corresponds to the electrode circled in blue below; the central sulcus is highlighted in green. (B) Reconstruction of the depth electrodes implanted in right hemisphere of Subject 2; electrodes used for reaching highlighted in red, electrodes used for grasping highlighted in blue (transparent medial view in inset). (C, D) Each task map displays the spatiotemporal distribution of significant increases (red spectrum) or decreases (blue spectrum) in high gamma energy relative to pre-cue baseline in 16 ms windows for Subject 1. Each row corresponds to a different iEEG electrode in the frontoparietal grid displayed in (A). All times are relative to cue onset. (E) A differential map is shown for Subject 1, which is the result of a Wilcoxon test between two conditions for each (channel, time) pair with FDR correction for comparisons across multiple time points within each channel. Channel and time pairs are in the red spectrum if forward reach is more activated than grasp, and in the blue spectrum if grasp is more activated than forward reach. The average times of relevant behavioral events are marked with vertical lines and

labeled (movement onset, MO; pressed target button, PT; released target button, RT; returned arm to home position, Home; released pressure bulb, Rest). © 2014 IEEE.

3.3.1 Subject Info

The subjects for this study were 55 year old (Subject 1) and 30 year old (Subject 2) right-handed males implanted with intracranial electrodes to map the ictal onset zone of medically resistant seizures prior to surgical resection. In Subject 1, an 8x8 grid of subdural platinum-iridium electrodes (Adtech, Racine, WI, 1.3 mm diameter exposed surface, 1-cm spacing) were surgically implanted over right frontal-parietal regions (see Figure 3.1), in addition to a 4x5 electrode grid over right lateral occipital cortex and a 1x8 electrode strip stretching from right mid-temporal regions to dorsolateral prefrontal cortex (both not shown). Subject 2 was implanted with a 1x8 electrode strip (Adtech; Racine, WI; as above) across right frontoparietal cortex, six depth electrodes with eight platinum macrocontacts each (Adtech; 1.41-mm long, 6.5 mm center-to-center spacing) placed medially from the right premotor area to the posterior parietal lobe, and one hybrid depth with eight platinum macrocontacts (Adtech; 1.57 mm long, 5 mm center-to-center) and sixteen microcontacts (Adtech; 75 micron diameter). Neuronavigation via the Cranial Navigation Application (BrainLab; Westchester, IL) was used during placement of the depth electrodes in Subject 1. Anatomical reconstructions of the subjects' brains with the location of implanted electrodes were generated by volumetrically co-registering the pre-surgical MRI with a post-surgical CT using BioImage (Figure 3.1A) (Duncan et al., 2004). Subject 1's seizures began after a bout of viral encephalitis with coma at 33 years of age. His complex partial seizures were

typically preceded by a somatosensory aura in his left hand with spread to the face and subsequent shaking of the left hand, and were sometimes followed by secondary generalization. Subject 2 had previously undergone chronic recording with partial resection of his right post-central gyrus and superior parietal lobule. Both patients gave informed consent for research testing, which was done in accordance with a protocol approved by the Institutional Review Board of the Johns Hopkins Medical Institutions.

3.3.2 Neural Signal Acquisition

Using a NeuroPort system (BlackRock Microsystems; Salt Lake City, UT), iEEG signals were initially sampled at 30 KHz with an analog bandpass filter with cutoffs of 0.3 Hz and 7500 Hz. The NeuroPort system then applied a digital 4th order Butterworth lowpass filter with a 250 Hz cutoff and downsampled to 1000 Hz. Artifactual channels were visually identified and excluded from all further analysis. Acquired iEEG signals were broadcast over UDP to an experimental workstation, where they could be accessed for online spectral feature extraction and model evaluation to drive the MPL.

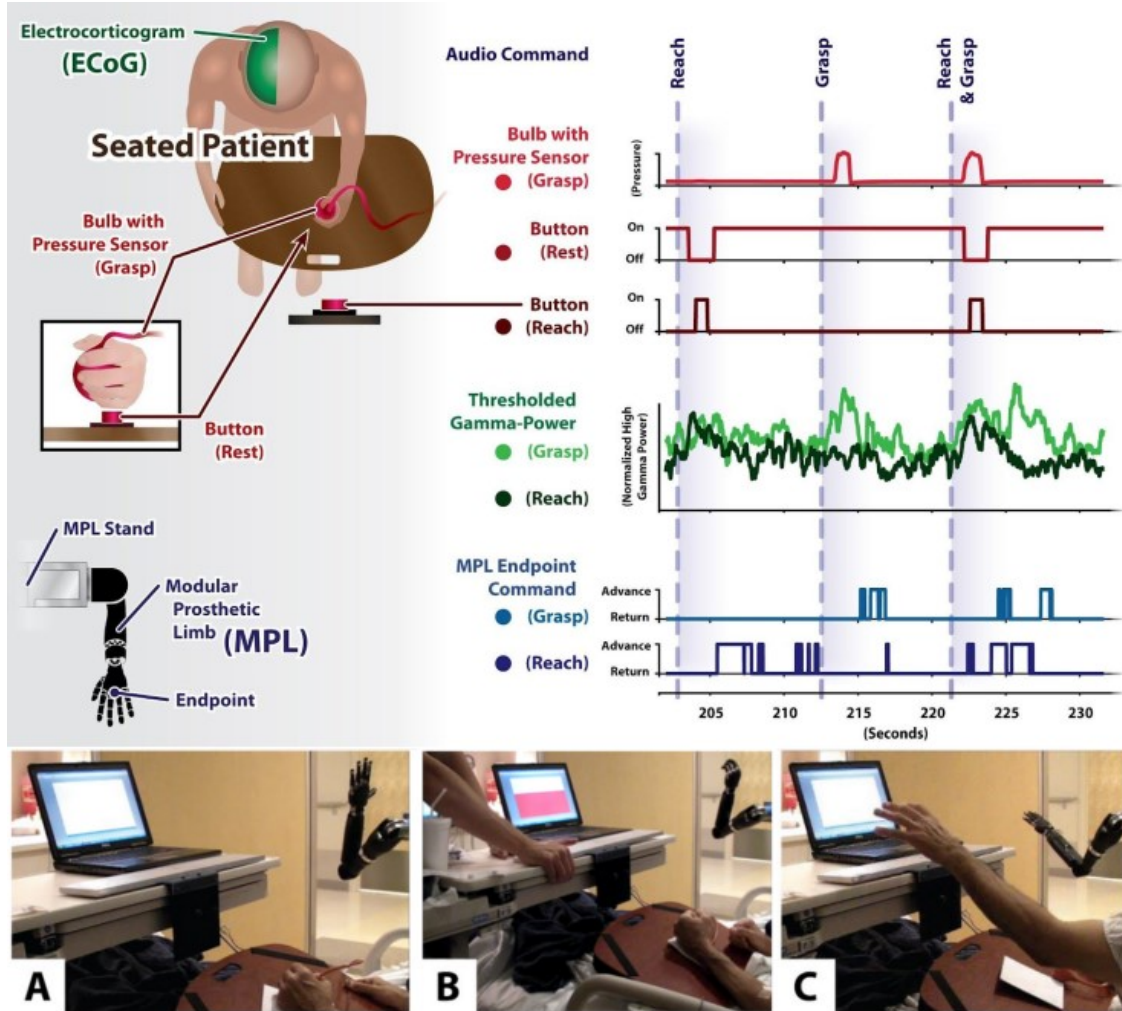


Figure 3.2. Schematics and photographs of experimental setup with MPL. (top) A schematic of the experimental setup is shown, with Subject 1 seated and interacting with three behavioral sensors. The MPL is to the front and right of the subject, in the same room as and in full view of the subject. Traces of the behavioral sensors, high gamma power, and MPL commands during a three trial segment are shown as an example. (A-C) The subject is seated on his hospital bed (not pictured, right of view), with his arm at rest on a lap desk with inset pushbutton or “home switch.” The subject is holding but not actively grasping the squeeze bulb used to query grasp status. On the subject’s hospital tray are a pushbutton for reach offset detection and a laptop displaying a red bar indicating pressure exerted on the squeeze bulb. (A) In the background, the MPL is at its baseline state (rest posture). (B) The subject is executing a grasp movement, and (C) the subject is executing a reach movement. © 2014 IEEE.

3.3.3 Experimental Procedures

Short offline data sets of 30 (Subject 1) or 50 (Subject 2) auditorily cued

trials were collected each for forward reaches and grasping movements. Audio cues of "reach" or "grasp" were delivered via external speakers by E-Prime software (PST, Inc.; Sharpsburg, PA). For Subject 2 only, the reach and grasp trials were interspersed with "Reach and Grasp" trials, of which there were also 50. The onset of each trial was manually initiated by the experimenter to ensure that the preceding reach was completed and an additional varying delay had passed before a cue was given. Behavioral states were detected using analog sensors sampled at 1000 Hz on the same hardware as the neural data: 1) the onset and offset of each reaching movement were detected using a pushbutton embedded in a wooden lap desk, 2) the termination of each reach on a distal target was detected using a pushbutton, and 3) the onset and offset of each grasp were detected using a pneumatic squeeze bulb connected via flexible tubing to an electronic pressure sensor. A detailed schematic of the experimental setup is included in Figure 3.1. Reaches by Subject 1 ranged in duration from 1.3 to 1.8 seconds (median = 1.4 seconds) with response latencies ranging from 330 to 500 ms (median = 410 ms), while grasps (i.e., as detected by the squeeze bulb) ranged in duration from 0.6 to 1.7 seconds (median = 0.9 seconds) with response latencies ranging from 380 to 930 ms (median = 460 ms). Reaches by Subject 2 ranged in duration from 1.9 to 4.8 seconds (median = 1.7 seconds), with response latencies ranging from 450 to 1450 ms (median = 790 ms), while grasps ranged in duration from 0.8 to 3.5 seconds (median = 1.0 seconds) with response latencies ranging from 640 to 2070 ms (median = 1010 ms).

3.3.4 iEEG Electrode Evaluation

Following collection of the reach and grasp datasets, event-related high gamma activations were analyzed. The audio cue played to the subject was split and fed into the BlackRock system; the beginning of this cue was detected and used as a stimulus onset (SO) marker. The 1024 ms prior to SO was pooled into baseline distributions for each channel, while the 3072 ms following the onset of the audio cue was used as a post-stimulus epoch. The 1024 ms prior to SO and 3072 ms following SO were segmented into 128 ms windows with 112 ms overlap. Each window was reduced to a single estimate of the high gamma analytic amplitude in a 16 ms bin using a Hilbert transform with an embedded, flat-top Gaussian bandpass filter with cutoffs of 72 and 110 Hz. Separate distributions were created for each post-stimulus 16 ms time bin and channel and referenced to the channel baseline distributions using two-sample t tests with significance threshold $p < 0.05$. The thresholds for p-value significance of these tests were corrected for multiple comparisons within each channel using the false discovery rate (FDR) correction (Benjamini and Hochberg, 1995). Any resulting significant p-values were then \log_{10} transformed, and any significant modulation was labeled as an increase or a decrease. This resulting matrix of statistical significance measures therefore contained timing information about activation that was used to exclude channels which displayed modulation in response to the audio cue. This entire analysis was performed with custom MATLAB (MathWorks, Inc.; Natick, MA) software, from which the results were available within the experimental session (see Figure 3.1).

3.3.5 BMI Model Training

For Subject 1, a final training set was recorded in which the verbal commands "reach," "grasp," and "reach and grasp" were pseudo-randomly chosen and played to the subject via external speakers with E-Prime; this training set contained 46 trials and lasted approximately five minutes. For Subject 2, the 150 trials spanning approximately sixteen minutes collected for electrode evaluation were used as a training set. Also for Subject 2, the initially trained model was used to drive a virtual version of the MPL as visual feedback during an additional 120 trials (i.e., 40 each of "reach," "grasp," and "reach and grasp"). The iEEG and behavioral data recorded during this block were used as the training set for online testing.

Signals in each training set were first spatially filtered with a common average reference [20] of all channels not excluded by visual inspection because of artifact or noise. Autoregressive power was extracted from the streamed signals using the Burg algorithm with model order 16 on a 400 ms window. The logarithm of the spectral power from components between 71.5 and 110 Hz were then averaged to yield an estimate of the broadband high gamma power. In offline data collection for model training purposes, feature extraction windows were overlapped by 300 ms.

In Subject 1, one electrode each was chosen for reach and grasp using information from the functional maps of post-stimulus activation. The high gamma log-powers during movement and rest movement were compared to manually establish a threshold for movement classification. In Subject 2, four channels each

were selected as model inputs to separate binary linear discriminant analysis (LDA) classifiers for reach and grasp. In addition, transition probabilities were adjusted manually before the testing session to smooth the output from the classifier. For this study, we used a probability of 0.95 for the probability of a rest classification if currently at rest (i.e., 0.05 for a movement classification), and 0.8 for the probability of a movement classification if currently in the movement state (i.e., 0.2 for a rest classification).

3.3.6 JHU/APL Modular Prosthetic Limb

Developed by JHU/APL under the Defense Advanced Research Project Agency (DARPA) Revolutionizing Prosthetics Program, the MPL (Figure 1.1) is an advanced upper-body extremity prosthetic and human rehabilitation device (Johannes et al., 2011). The MPL has 17 controllable degrees of freedom (DoF) and 26 articulating DoF in total (Figure 1.1, with specifications in Table 3.1). To facilitate control from neural decoded motion intent, the MPL has a custom software interface, VulcanX, that receives movement/motion commands locally and sends them over a controller area network (CAN) bus to a limb controller (LC) board in the hand of the MPL (Harris et al., 2011). Three types of high-level control commands, passed through VulcanX, are fused together to form individual actuator commands by the LC: 1) Degree of Motion Control (DOM) commands, which allow each degree of motion to be controlled individually with position and/or velocity commands; 2) Endpoint Control (EP) commands, which allow the hand's position and orientation to be controlled in Cartesian space using a Jacobian-based algorithm

for computing inverse kinematics; and, 3) Reduced Order Control (ROC) commands, which allow pre-programmed hand grasp patterns to be actuated in a coordinated fashion as a single degree of freedom (Bridges et al., 2011; Fifer et al., 2012). EP velocity and ROC commands were utilized to control reach and grasp, respectively, in this study.

<u>Specification</u>	<u>Value</u>	<u>Units</u>	<u>Specification</u>	<u>Value</u>	<u>Units</u>
Articulating DOF	26	N/A	2-jaw pinch force	15	lbf
Controllable DOF	17	N/A	3-jaw chuck pinch force	25	lbf
Onboard motor controllers	17	N/A	Lateral key pinch force	25	lbf
Mass of hand and wrist	1.9	lbs	Upper arm joint speed	120	deg/s
Mass of upper arm with battery	7.6	lbs	Wrist joint speed	120	deg/s
Payload capacity (wrist active)	15	lbs	Finger joint speed	>540	deg/s
Cylindrical grasp force	70	lbf	Communications	CAN	N/A

Table 3.1. Summary of MPL specifications. © 2014 IEEE.

The MPL software and hardware architecture consists of a distributed network of processors that include a Neural Fusion Unit (NFU), a Limb Controller (LC), 10 Small Motor Controllers (SMC), 4 Large Motor Controllers (LMC), and 3 Wrist Motor Controllers (WMC). The NFU is a processor capable of running on-board neural decoding and sensory stimulation algorithms for generation of limb motion commands. The LC is the main processor of the limb system and is responsible for receiving limb control commands, running high-level control algorithms, and coordinating the control of the individual motors in the system. The LMC, WMC, and SMC integrated software/hardware systems, which receive real-time data from temperature, torque, and position sensors located within each joint,

are responsible for providing closed-loop position, velocity and torque control of the brushless DC motors in the limb system. In addition to internal polling, these joint sensors broadcast information to the user/experimenter along the MPL's external communication CAN bus for data logging and external control processing.

3.3.7 Online Testing

Once the high gamma thresholds for movement were established, classification outputs from the trained models of reach and grasp movements were simultaneously used to actuate the MPL via the VulcanX interface. Whenever the classifiers predicted that the subject was reaching and/or grasping, the MPL was commanded to reach and/or grasp, respectively, at a set rate. If the either reach or grasp classifier predicted that the subject was resting, the limb was commanded to return to its rest arm or hand posture, respectively, at an equal rate. For Subject 2 only, the return rate for reaching was adjusted to be 50% higher than the forward rate. High gamma log-power calculations were performed in 400 ms windows (i.e., as in training) computed as quickly as possible on the streaming iEEG signals to provide inputs to the trained model (i.e., 11 ms for Subject 1, slowed to 32 ms for Subject 2 purposefully to avoid inundation of the MPL). Both subjects completed three blocks of online trials by performing the same overt movements with their native limbs as during the training set. In Subject 1 only, the second and third blocks were separated by a battery of physical and imagined movements that were not analyzed as a part of this study.

3.3.8 Quantitative Evaluation of Control

The physical movement blocks lasted approximately 4, 11, and 13 minutes for Subject 1 and 11, 15, and 10 minutes for Subject 2 (respectively). The MPL VulcanX control software created a log of commands sent to the limb with timestamps, which was compared offline to the timestamps of salient cues and behavioral events recorded by the BlackRock system (e.g., subject leaves the home switch, subject grasps the squeeze bulb, etc.). Trials were designated as starting 500 ms prior to the earliest of the reach and/or grasp onsets and ending 500 ms prior to the onset of the next trial. For each trial, we recorded the proportion of correct commands (e.g., the percentage of ‘grasp’ commands with a positive velocity when a physical grasp was performed) in a window of equal length to the corresponding physical movement duration for that trial. To account for variable response latencies by the subject and an inconsistent system latency, the start of the window relative to the onset of the trial was selected individually for each trial to maximize the accuracy. For reach-and-grasp trials, durations and latencies were selected separately for the reach and grasp components. As a control, a window whose length equaled the average duration of the reaches or grasps was used to compute the peak reach or grasp command accuracy in grasp-only and reach-only trials, respectively. Accuracy for each trial was computed as the average of the single trial sensitivity (i.e., proportion of reach or grasp commands within the selected movement window) and the single trial specificity (i.e., proportion of rest commands outside of the selected movement window). The median reach command accuracies for reach-only vs. grasp-only and reach-and-grasp vs. grasp-only and the grasp command accuracies for grasp-only vs. reach-only and grasp-

only vs. reach-and-grasp were compared using a nonparametric two-sided Wilcoxon rank sum test.

3.4 Results

Both subjects were able to attain a high degree of subjective control over reaching and grasping with the MPL across the experimental session with no model adaptation while moving their native limbs. Furthermore, both subjects were able to achieve a level of performance throughout the experimental session that was qualitatively similar to the first block.

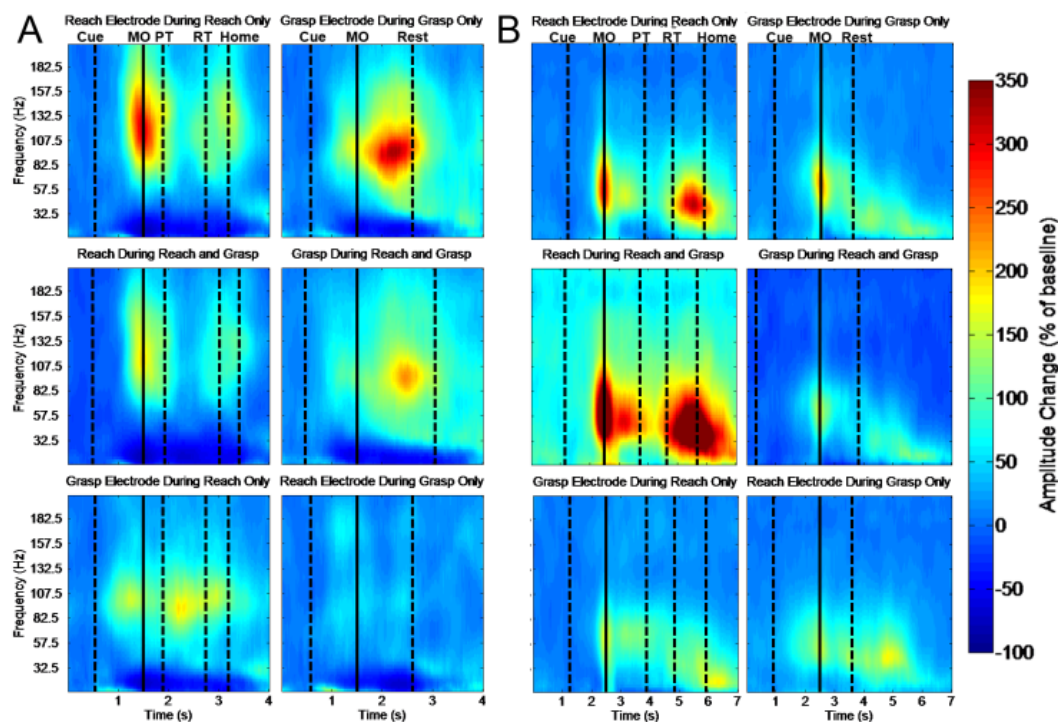


Figure 3.3. Average change of power spectral densities (PSD) relative to baseline, aligned to movement onset. (A) Reach and grasp electrodes are shown for Subject 1, and (B) two representative electrodes are shown for Subject 1. The first vertical dashed line in all plots corresponds to the average time the audio cue began. For each trial, the baseline was chosen from before the onset of the cue (leftmost dashed line). The solid line denotes movement onset (MO). In reach trials, the dashed lines after the solid line correspond to the average time of the reach

completion (pressing target button, PT), release of the target button (RT), and return to home (resting on the home switch), from left to right. The rightmost dashed line in the grasp trials corresponds to the average time of grasp completion. The PSD's were computed via autoregressive spectral analysis. Window size did not allow for accurate calculations at 0-7.5Hz, so these frequencies are not displayed.

We investigated the spectrogram of modulation time-locked to salient stimuli and behavioral events to validate our choice of the high gamma band for online control. As shown in the functional mapping results (Figure 3.1), the electrodes used for control of the MPL exhibited robust high gamma modulation. Figure 3.3 shows the time-frequency response of the reaching electrode during reach-only and reach-and-grasp trials of the online task, as well as the grasping electrode during grasp-only and reach-and-grasp trials. High gamma modulation in the reaching electrode occurred within the frequency range of 80-160 Hz for Subject 1, in contrast with the more spectrally restricted 60-120 Hz modulation in the grasping electrode. Subject 2 displayed activation at a lower frequency range, centralized around 40-90 Hz. These frequency ranges of power modulation show that while our choice of 71.5-110 Hz for control may not have exactly matched the neurophysiological response to the task, it did capture a substantial amount of the power modulation for both tasks. The temporal envelope of activation was relatively restricted in the reaching electrode for both subjects, with mean power modulation peaking roughly 200 ms before the onset of movement. Subject 2 had similarly tight timing in grasp-related cortical activation. In contrast, power modulation in the grasping electrode of Subject 1 began an average of 300 ms prior to movement onset and peaked more than 300 ms after movement onset. The reach-related high gamma power modulation also differed from grasp-related power modulation in the

presence of two distinct temporal peaks, time-locked to outward reach and the subsequent return to rest. Figure 3.3 (bottom row) provides verification that gamma power modulations in the grasp and reach electrodes were markedly lower during execution of reach and grasp, respectively.

During online control in Subject 1, we observed that control of grasping was less reliable for reach-and-grasp trials than grasp-only trials. Figure 3.3 (middle row) shows that high gamma modulation in the reaching and grasping electrodes during reach-and-grasp trials was qualitatively reduced relative to reach-only and grasp-only trials. To evaluate this effect, log high gamma power was extracted in 300 ms around the onset of movement. Statistical analysis revealed that log power in the grasping electrode around the onset of grasp was significantly higher in grasp-only than in reach-and-grasp trials ($p < 0.05$, Wilcoxon test); the log power in the reaching electrode around the onset of reach was not significantly different in reach-only and reach-and-grasp trials, however. Identical analyses performed in Subject 2 did not reveal any significant differences in movement-related power modulation between reach-and-grasp trials and either the reach-only or grasp-only trials in any of the electrodes used for control ($p > 0.05$, Wilcoxon test, Bonferroni-corrected).

To evaluate the high gamma power modulation associated with movement state in reach-only trials, log power was also extracted in time windows around the onset of stable hold and the onset of return, in addition to a baseline window preceding the cue. For Subject 1, log-power in the reach electrode was significantly higher in the reach window and return window than in the hold window, all of

which were significantly higher in the baseline window ($p < 0.05$, one-way ANOVA with Tukey's honestly significant difference post-hoc). In all four electrodes used for reaching control in Subject 2, median hold activity was lower than median reaching and returning activity; the difference was significant in three out of four electrodes ($p < 0.05$, one-way ANOVA, with Tukey's honestly significant difference post-hoc). Reaching, returning, and intermediate hold windows similarly exhibited higher levels of high gamma activity than baseline windows in Subject 1.

Classification accuracy for both reaching and grasping started and remained high throughout all three blocks of the online task. The mean reach classification accuracy across all trials was 86% (Subject 1) and 82% (Subject 2) for reach-only trials; the reach accuracy across reach-and-grasp trials was 83% (Subject 1) and 89% (Subject 2). The mean grasp classification accuracy across all grasp-only trials was 81% (Subject 1) and 96% (Subject 2); the grasp accuracy across reach-and-grasp trials was 55% (Subject 1) and 88% (Subject 2). The evolution of classification accuracies showed no significant effect of block ($p > 0.05$, one-way ANOVA) in either subject. The trial-by-trial reach and grasp accuracies are depicted in Figure 3.4. Reach accuracies were significantly higher than chance for both reach-only trials and reach-and-grasp trials ($p < 0.05$, Wilcoxon test with Bonferroni correction), while grasp accuracies were significantly higher than chance for grasp-only trials ($p < 0.05$, Wilcoxon test with Bonferroni correction), but not reach-and-grasp trials in Subject 1 only ($p=0.078$, Wilcoxon test). Grasp accuracies were significantly higher in grasp-only trials than in reach-and-grasp trials in both subjects ($p < 0.05$, Wilcoxon test). Reach accuracies were not significantly higher in

reach-only trials than in reach-and-grasp trials for Subject 1 ($p > 0.05$, Wilcoxon test), although reach accuracies were higher in reach-and-grasp trials than in reach-only trials for Subject 2 ($p > 0.05$, Wilcoxon test).

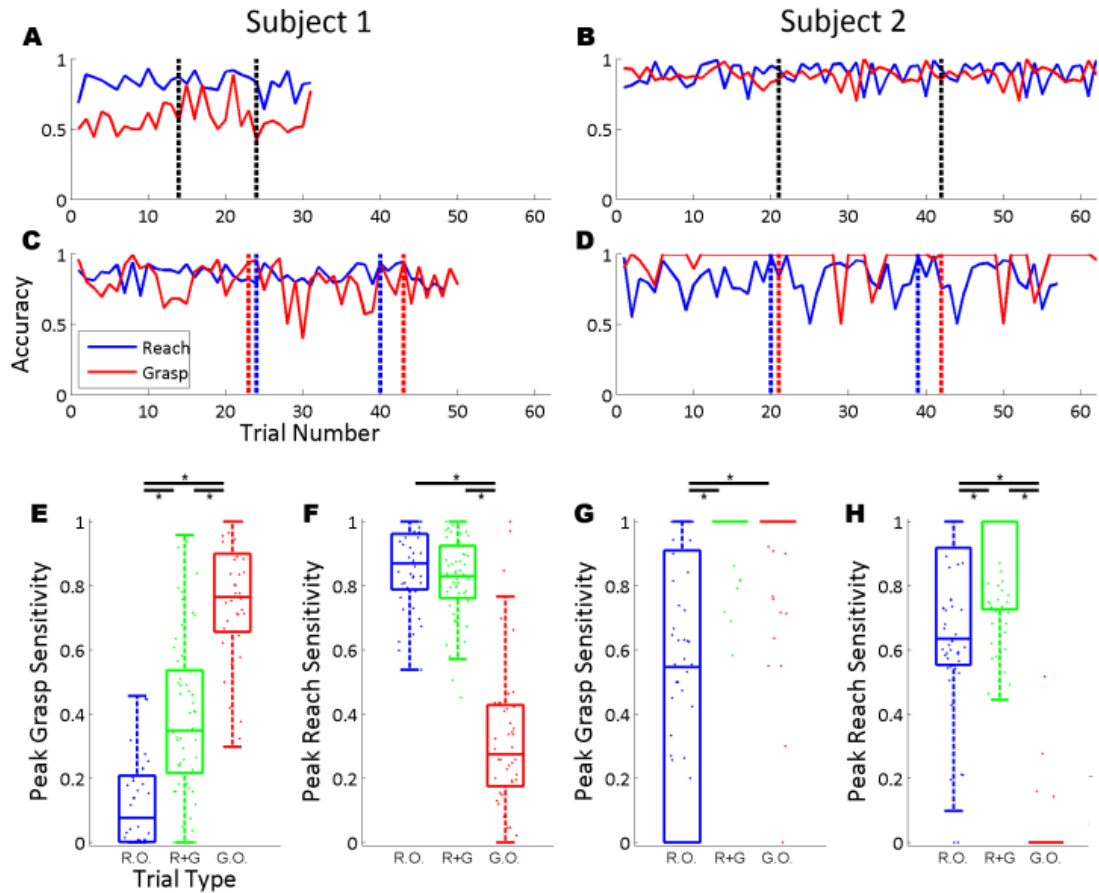


Figure 3.4. Limb performance accuracy metrics. (A, B) The accuracies are shown for reaching and grasping during trials where reach and grasp were executed simultaneously. (C, D) The reach and grasp accuracies are shown for reach and grasp only trials, respectively. The vertical dashed lines in A-D denote separate blocks. Distributions are shown and summarized with boxplots of the peak sensitivities for grasps in Subject 1 (E), reaches in Subject 1 (F), grasps in Subject 2 (G), and reaches in Subject 2 (H). Each distribution is comprised of the peak sensitivities from each trial. Bars above the boxplots with asterisks mark distributions with significantly different medians ($p < 0.05$, Wilcoxon test).

To investigate whether reaching and grasping were indeed independent, sham sensitivities were calculated as a control; reach sensitivities were calculated

during grasp-only trials and grasp sensitivities were calculated during reach-only trials (Figure 3.4). Since no physical reaches took place in grasp-only trials, nor physical grasps during reach-only trials, the average reach and grasp durations were used as surrogates. Peak reach sensitivities were significantly higher in cued reach-only and reach-and-grasp trials than in cued grasp-only trials for both Subjects ($p < 0.05$, Wilcoxon test); reach sensitivities were significantly higher in reach-only trials than in reach-and-grasp trials for Subject 2 ($p < 0.05$, Wilcoxon test) but the difference was not significant in Subject 1 ($p = 0.16$, Wilcoxon test). Peak grasp sensitivities were higher in cued grasp-only and reach-and-grasp trials than in cued reach-only trials for both subjects ($p < 0.05$, Wilcoxon test); grasp sensitivities were significantly higher in grasp-only trials than in reach-and-grasp trials for Subject 1 ($p < 0.05$, Wilcoxon test) but the difference was not significant in Subject 2 ($p = 0.15$, Wilcoxon test).

3.5 Discussion

We were able to provide two human subjects with control of the MPL using a control scheme that exploited individual functional anatomy, i.e., the population responses in cortical regions used for control of each subject's native arm. This allowed our subjects to achieve control without extensive training. To identify iEEG control sites and characterize their response selectivity, we used iEEG functional mapping during reaching and grasping. By using electrodes over cortical areas that were differentially activated during reaching and/or grasping, we were able to afford the patient independent control over the reaching and grasping

functionalities of the MPL arm. We showed that these two movements, when executed individually, elicited cortical responses in the gamma band that generalized to their simultaneous execution, although the same responses occurred with a reduced magnitude.

Additionally, the subject's control over the arm did not wane over the course of three separate blocks using thresholds derived from a short training block. Models were equally effective across blocks with no adaptation or re-training, providing evidence that control was achieved by accurately detecting the naturalistic circuits for reaching and grasping, not via adaptation or operant conditioning. Reach and grasp commands were controlled independently, suggesting functional segregation of these movements at the spatial scale of clinically routine iEEG electrodes. There is abundant evidence from experiments in non-human primates that reaching and grasping engage different networks of cortical areas (Rizzolatti et al., 1998). As in non-human primates, human premotor cortices engaged by reaching are likely dorsal to those engaged by grasping (Filimon, 2010). As expected, the iEEG site activated by and used for control of reaching was dorsal to the site activated by and used for control of grasping.

Our BMI used event-related high gamma power augmentation as an index of task-related neural activity during physical movements. This choice was based on a body of literature which demonstrates that high gamma band modulation is an index of cortical processing in humans (Crone et al., 2001b, 1998; Miller et al., 2007b; Ray et al., 2008b) and recent experimental evidence that high gamma power changes are strongly and positively correlated with the firing rates of neuronal

populations in close proximity to recording electrodes (Liu and Newsome, 2006; Manning et al., 2009; Ray et al., 2008a; Ray and Maunsell, 2011). Our findings are consistent with empirical evidence that compared with power changes in other frequencies, high gamma power augmentation has high spatial selectivity with respect to task-related cortical activation, such that adjacent iEEG electrodes can yield signals with greater independence at higher frequencies (Flinker et al., 2010a; Lachaux et al., 2012). High gamma responses are also robust enough to be detected in single trials (Flinker et al., 2010b), a necessary requirement for BMI applications. Furthermore, several studies have shown that high gamma features extracted from human iEEG outperform corresponding lower frequency features for offline motor decoding (Kubaneck et al., 2009; Pistohl et al., 2013) and online BMI control (Schalk et al., 2008b; Yanagisawa et al., 2012, 2011).

This study focused on the control of reach and grasp in the MPL since they are fundamental to upper limb use, which provides a proof of concept for the systems-level integration groundwork necessary for more complicated and dexterous tasks. Reaching and grasping movements were decoded for actuation of the MPL with high accuracy and stability; furthermore, this was achieved in a clinical epilepsy monitoring setting under time constraints that did not allow for long-term training or testing. Although this prohibited testing the long-term stability of MPL control, it did demonstrate the feasibility of obtaining MPL control within a compressed timeframe, which could have important clinical benefits. Specifically, it would be highly advantageous to demonstrate acceptable brain control of a neuroprosthetic at the time of surgical implantation in order to verify

the placement of electrodes and troubleshoot any technical difficulties at the time of the operation. Non-invasive methods of functional mapping (e.g., fMRI) can be used to perform gross surgical planning, but intraoperative verification of control with iEEG would be extremely useful to refine the final implantation site. This would help to avoid the need for re-implantation because the patient is unable to control the neuroprosthetic. This would be both costly and increase surgical risk. Although the total time for our experiment was longer than that of an awake craniotomy, most of this time was due to experimental setup and troubleshooting, and thus could be reduced with additional practice.

We observed during online testing with the subject that it was fairly common for the MPL to exhibit a secondary reach or grasp as the subject returned to the resting position. This corresponded to a burst of high gamma activity as the subject initiated return of his limb to the home switch or as the subject relaxed his hand after squeezing the bulb. This was best demonstrated in the reaching trials by post-hoc offline analysis of the high gamma power in windows associated with reaching to, holding at, and returning from the distal reach target, which demonstrated a higher degree of modulation for reaching and returning than for the intermediate holding in the reaching electrode for Subject 1 and for a subset of the reaching electrodes in Subject 1.

This report provides additional evidence for the potential utility of iEEG as a source of control signals for BMIs. Although the participants in this study did not suffer from upper limb paralysis, we believe that the technique of rapid trial-averaged spatiotemporal mapping of high gamma modulation can be used to

identify sites that are activated when subjects with motor impairments attempt to perform movements. These patients often have residual motor function and could attempt to move with assistance, be moved passively, or observe upper limb movements in a trial-based framework.

A large amount of decoding and BMI success has been achieved using command signals derived from iEEG (Leuthardt et al., 2004; Schalk et al., 2008b; Wang et al., 2013; Yanagisawa et al., 2012, 2011). Although iEEG macroelectrodes (Leuthardt et al., 2004; Schalk et al., 2008b), iEEG microelectrodes (Chao et al., 2010), and multi-electrode arrays (Collinger et al., 2013; Hochberg et al., 2012) have all been used to demonstrate effective BMI control in small populations, no large-scale longitudinal studies have compared the tissue response and control performance between these classes of implants. Much previous work has illustrated a significant redundancy of motor encoding at the single neuron level (Narayanan et al., 2005), suggesting that population activity could be useful for prosthetic control. Nevertheless, there is evidence from studies in motor, perceptual, and cognitive systems that the richness of encoding increases with improvements in spatial resolution (i.e., iEEG macroelectrodes exhibit coarser encoding than iEEG microelectrodes, and iEEG microelectrodes exhibit coarser encoding than local field potentials from multi-electrode arrays) (Slutzky et al., 2010). It is possible that as the spatial resolution of iEEG implants improves and more comparative studies are done between iEEG and multi-electrode arrays, that iEEG implants for BMI control will be an attractive option for some patients (Thongpang et al., 2011; Viventi et al., 2011). In the meantime, iEEG recordings in patients undergoing epilepsy surgery

will continue to serve as a platform for demonstrating the degree of useful control that can be achieved without extensive training, prior to chronic implantation of iEEG electrodes for BMIs.

3.6 Study Acknowledgements

Data analysis and online control were supported by the National Institute of Neurological Disorders and Stroke under Grant 3R01NS0405956-09S1, by DARPA under contract 19GM-1088724, and by the National Institute of Biomedical Imaging and Bioengineering under Grant 5T32EB003383-08. The MPL was developed with funds from DARPA under contract No. N66001-10-C-4056. We wish to thank Heather Benz, Anna Korzeniewska, Zachary Huff, and Griffin Milsap for lab meeting discussions of our approach and analysis, Howard Conner for building the stand used to hold the MPL, and Charles Schuman for constructing the mounting interface.

Chapter 4

Overlapping Spatiotemporal Representations of Finger Vibrations in the Postcentral Gyrus at 3 mm Scale in a Human Subject

4.1 Abstract

The somatosensory representations of individual fingers in the postcentral gyrus are arranged somatotopically, extending superiorly from first to fifth digit. Finger areas have been shown to overlap in functional magnetic resonance imaging (fMRI) studies, but not in electrocorticographic (ECoG) recordings of neuronal populations. Addressing this question has been impossible using traditional ECoG grids due to insufficient spatial resolution. Here we present the results of a fingertip vibration study with a human subject implanted with a high-density ECoG (hdECoG) grid with 3mm center-to-center spacing on the surface of the postcentral gyrus in putative finger areas. Spectral and amplitude features exhibited significant task-related changes, including the existence of event-related potentials (ERPs), power increases in the high gamma band (70-120 Hz), and power decreases in theta (4-8 Hz), mu (8-12 Hz), and beta bands (14-30 Hz). The high gamma band exhibited the most somatotopically organized, yet still overlapping, responses to vibrational stimuli. Despite a clear somatotopic gradient from first (inferiorly) to fifth digits (superiorly), over 62% (28 of 45) of sites with task-related high gamma increases exhibited significant responses to multiple fingers. High gamma increases showed

the lowest spatial correlation across fingers, with an average Pearson's correlation coefficient (r) of 0.19 between the finger responses, compared to spatial correlations of 0.64-0.69 for low frequency decreases. Within the high gamma responses, the thumb appeared to be the most independent, with the lowest average spatial correlation to the other finger representations ($r = 0.01$, compared to averages of 0.23, 0.34, 0.28, and 0.10 for index, middle, ring, and little fingers). Vibrotactile stimuli lasted 500 ms; the high gamma responses peaked approximately 170-210 ms after stimulus onset, and decreased steadily until 200-400 ms after stimulus offset. ERPs peaked 90-220 ms after stimulus onset and 130-320 ms after stimulus offset. High gamma responses exhibited clear finger selectivity in single trials, with finger classification accuracies peaking at 98.8% when smoothing over windows with centers spanning 240 ms, centered 220 ms after stimulus onset. Additionally, movement-related somatosensory responses generally exhibited larger magnitude yet less finger-specific activation than vibration responses. This study provides evidence that finger representations, particularly in the high gamma band, are somatotopically organized yet overlap at 3 mm scale.

4.2 Introduction

Nearly eight decades ago, Penfield and Boldrey localized finger sensations to the postcentral gyrus between representations of the face (inferiorly) and the whole hand (superiorly), and noted a consistent ordering--from inferior to superior--of thumb, index finger, middle finger, ring finger, and little finger (Penfield and Boldrey, 1937). Recordings from nonhuman primates revealed the granularity of

the finger representation in primary somatosensory cortex (S1), describing four parallel yet distinct representations on the postcentral gyrus (Kaas et al., 1979; Powell and Mountcastle, 1959). Individual neurons in these representations respond preferentially to either cutaneous or muscular/joint stimuli, with the proportions of each type varying across the four sub-areas (Kaas et al., 1979; Powell and Mountcastle, 1959). In particular, neurons in Brodmann's areas (BA) 3b and 1 have been observed to respond robustly to cutaneous stimulation (Kaas et al., 1979).

Functional magnetic resonance imaging (fMRI) studies have shed light on the relative size and overlap of finger representations on the human postcentral gyrus. Many studies have observed overlapping finger sensory representations with distinct centers (Maldjian et al., 1999; Martuzzi et al., 2014; Nelson and Chen, 2008; Schweizer et al., 2008; van Westen et al., 2004). Several studies have also confirmed the existence of multiple parallel finger representations within the human postcentral gyrus, likely corresponding to BA 3a, 3b, 1, and 2 (Hluštík et al., 2001; Martuzzi et al., 2014; Nelson and Chen, 2008). Although fMRI permits simultaneous sampling of voxels spanning the postcentral gyrus, its limited signal-to-noise ratio and temporal resolution makes it difficult to ascertain the cortical dynamics of tactile stimulation of the fingertips or observe single trial responses. Furthermore, most fMRI studies of finger representation have been performed at 3T (Nelson and Chen, 2008; Schweizer et al., 2008; van Westen et al., 2004), or 4T (Maldjian et al., 1999) and have presented findings aggregated across multiple subjects, blurring the relative spatial relationships of individual finger representations (Maldjian et al.,

1999; Nelson and Chen, 2008; Schweizer et al., 2008; van Westen et al., 2004). Although a recent 7T study has provided a glimpse into finger responses within single subjects (Martuzzi et al., 2014), the apparent overlap between digit responses has not been demonstrated in electrophysiological recordings. Since BA1 responds robustly to cutaneous stimulation and has been shown in cytoarchitectural studies to usually reside on the crown of the postcentral gyrus (Geyer et al., 2000, 1999)--with infrequent encroachment by BA2 (Grefkes et al., 2001)—it is a prime candidate for electrophysiological mapping of vibrotactile representations on the cortical surface.

Electrocorticography (ECoG) offers an intermediate point in the spatiotemporal sampling tradeoff inherent in all existing human functional mapping techniques. It has much greater temporal resolution than fMRI and much wider sampling than single or multi-unit studies with microelectrodes. ECoG signals are composed of a variety of components that may reflect different neural elements and neurophysiological processes. Event-related potentials (ERPs), capture phase-locked changes in overall signal amplitude thought to reflect ascending inputs from the thalamus (Pfurtscheller and Lopes da Silva, 1999a). ERPs from ECoG have previously been used to demonstrate somatotopic representation of finger sensation in humans (Sutherling et al., 1992; Woolsey et al., 1979) and as a common methodology confirming the similarity of human and nonhuman primate finger representations (Shoham and Grinvald, 2001; Woolsey et al., 1979, 1942). In addition to ERPs, event-related spectral modulation in the alpha/mu (8-12 Hz), beta (14-30 Hz) and high gamma (70+ Hz) bands has been demonstrated across sensory

modalities (Crone et al., 2001a; Jacobs and Kahana, 2009; Meshulam et al., 2013; Pasley et al., 2012) and in sensorimotor cortex during arm (Anderson et al., 2012; Tonio Ball et al., 2009; Pistohl et al., 2008), hand (Acharya et al., 2010; Chestek et al., 2013; Pistohl et al., 2012; Yanagisawa et al., 2011), and finger movements (Kubaneck et al., 2009; Miller et al., 2009; Siero et al., 2014). Task-related increases in high gamma signal power in particular have been shown to have extremely high spatial and temporal resolution relative to lower frequency phenomena (Crone et al., 1998; Jerbi et al., 2009), and have been shown to correlate well with population firing rates (Manning et al., 2009; Ray et al., 2008a) and fMRI BOLD (Genetti et al., 2014; Khursheed et al., 2011; Lachaux et al., 2007a; Siero et al., 2014).

The spacing between finger representations on the surface of the human postcentral gyrus, is on the order of 1-5 mm (Martuzzi et al., 2014), which makes it impossible to adequately sample them with traditional clinical ECoG grids (1 cm center-to-center spacing). Occasionally, however, a patient's seizure semiology will involve language or motor symptoms and make him or her a candidate for implantation of a high-density ECoG (hdECoG) grid. While hdECoG implantations occur infrequently, the high spatial and temporal resolution coupled with a high signal-to-noise ratio make this modality particularly valuable for probing cortical representations of sensation or behavior. To date, hdECoG implants have been used primarily to study articulatory (Bouchard and Chang, 2014) and auditory (Mesgarani et al., 2014; Mesgarani and Chang, 2012) cortical representations. We present evidence, in a single subject with a 3 mm spaced hdECoG grid, for

somatotopically ordered yet overlapping finger representations in postcentral gyrus at the spatial scale of neuronal populations.

4.3 Methods

4.3.1 Subject Info and Neural Signal Acquisition

The subject was a 20-year old right-handed male implanted with an 8x16 hdECoG electrode grid (Adtech; Racine, WI; 1mm diameter, 3 mm center-to-center spacing) over left sensorimotor cortex for mapping the seizure focus and eloquent cortex prior to epilepsy resection surgery. Placement of the high-density grid was determined based on the semiology of the patient's seizures, which consistently began with tingling in the right forearm and spread proximally to the rest of the right upper arm. A previous resection had been performed eleven years prior, removing a medial portion of the left frontal lobe, without long-term reduction in seizure frequency or change in semiology. In addition to the high-density grid, depth electrodes were implanted in the inferior frontal and parietal lobes and standard clinical macroelectrode strips were placed in the parietal cortex; signals from these electrodes were not analyzed as a part of this study. The hdECoG signals were recorded at 1 kHz by a NeuroPort system (BlackRock Microsystems; Salt Lake City, UT). Signals were initially sampled at 30 kHz with an analog bandpass filter with cutoffs of 0.3 Hz and 7.5 kHz, then downsampled. Artifactual channels were visually identified and excluded from any subsequent analyses. Referencing was done post-hoc with a common average reference. Anatomical reconstruction of the hdECoG grid placement relative to the subject's neuroanatomy was performed using

BioImage Suite (Duncan et al., 2004). A preoperative MRI depicting clear structural anatomy was volumetrically co-registered with a postoperative CT containing the electrodes. As a final step, the reconstruction was checked against intraoperative photos from the implantation and explantation of the high density grid. The electrode locations on a two-dimensional snapshot of the reconstruction were manually adjusted relative to the underlying cortex via rotation, scaling, and translation of the grid in the GNU Image Manipulation Program (GIMP) to optimize the alignment between the grid and prominent gyral and sulcal landmarks present in both the 3D reconstruction and the intraoperative photos. The subject gave informed consent for research testing, which was done in accordance with a protocol approved by the Institutional Review Board of the Johns Hopkins Medical Institutions.

4.3.2 Experimental Tasks

Vibrational motors (14mm, 3V coin motors) were taped to the subject's fingertips, wrist (over the ulnar head), elbow, and shoulder. The subject rested his hand over an armrest with their fingers unsupported and pointed down. He watched a sporting event on television throughout the experiment. Gauze was placed between the fingers to prevent vibrations from spreading to neighboring fingers. The motors were vibrated one at a time in a pseudorandom order for 0.5 seconds per trial. There was an intertrial interval of 1.5 seconds between vibrations to allow for the cortical signals to recover and a baseline to be captured. The motors were controlled by an Arduino Duemilanove with two Adafruit motor v2.3 shields

powered by a 9V battery. We conducted two consecutive blocks of 200 trials, resulting in each motor being vibrated 50 times. Only vibrations of the fingertips were analyzed in this study. The vibration frequency of the motors was approximately 150 Hz. Each trial began with a pulse being sent by the Arduino to the analog input of the Blackrock Neuroport system for data alignment.

To compare digit representations for passive vibration to those for movement-related sensory feedback, a subsequent session was performed in which the patient was visually cued to move individual fingers. The subject wore a CyberGlove (CyberGlove Systems; San Jose, CA) to track the kinematics of their finger movements. The subject was instructed to tap each finger repeatedly on appearance of the corresponding visual stimulus. The session consisted of 25 movements by each finger. The period of peak flexion (i.e., of the first finger movement in the series) in each trial was used as an alignment point for subsequent neural feature extraction to highlight the period of maximal sensory feedback.

4.3.3 Event-Related Potential and Spectral Estimation

Prior to ERP estimation, hdECoG signals were forwards-backwards filtered with a 150-order finite impulse response (FIR) highpass filter with a cutoff frequency of 1 Hz. Signal amplitudes were then baseline-normalized so that the pre-stimulus (i.e., baseline) period of had zero mean and unit standard deviation.

Event-related spectral modulation was also estimated in theta (4-8 Hz), mu (8-12 Hz), beta (14-30 Hz), and high gamma (70-120 Hz) bands. Spectral extraction was done separately for each band using a two-step process to limit leakage

between neighboring frequency bands. Raw signals were first bandpass filtered forwards and backwards with an FIR filter, and then the spectral power in overlapping windows was estimated using the Chronux toolbox (Bokil et al., 2010; “Chronux,” 2015). The filter order was 300 for theta, mu, and beta bands and 150 for the high gamma band; cutoff frequencies are the bounds of the ranges listed above. Once filtered, the spectral power was estimated in overlapping windows of 128 ms (high gamma), 256 ms (beta), or 512 ms (mu and theta); in all bands, consecutive windows were offset by 16 ms. A multitaper method was used to extract spectral power, using 5 tapers and a time-bandwidth product of 3 to extract high gamma power; one taper and a time-bandwidth product of 1 were used for the lower frequencies.

Smoothed amplitudes and spectral powers were then baseline-normalized so that the pre-stimulus (i.e., baseline) period of each trial had zero mean and unit standard deviation. Trial-averaged spectrograms for single channels were generated using the high gamma multitaper approach described above, without any pre-filtering, so that modulation in all frequencies could be observed simultaneously.

Smoothed amplitudes and spectral estimates were statistically compared to the baseline period for significance using a *t* test. One window was selected from each baseline period so that the variance estimate of the null distribution would not be distorted by correlated, nearby time windows. Time windows after stimulus onset were then compared to the baseline distribution of the corresponding channel. Two-sided *p*-values were thresholded for significance using the false

discovery rate (FDR) correction with $q = 0.05$ for multiple comparison across channels and times.

4.3.4 Finger Classification Analyses

A linear discriminant analysis (LDA) was run to classify which finger was stimulated in each trial. This analysis serves not only as an aggregate measure of digit representation separability (i.e., the degree of somatotopy), but also the timing of this somatotopy. For each feature type—smoothed amplitude and theta, mu, beta, and high gamma power—an LDA classifier was trained for time windows with consistent timing relative to the onset of the vibrational stimulus. Inputs to these classifiers were smoothed with varying kernel widths to assess not only the timing of peak classification accuracy, but also the duration of time over which this information was present in the neural features. Classifiers were trained and tested under tenfold cross-validation, in which 90% of the trials were used to select channels model inputs and train a classifier to be evaluated on the remaining 10% of the trials. Individual channels were selected as model inputs if they were able to classify finger stimuli in the training set above chance level. Chance level in this context was defined as the number of trials correctly classified assuming random classifications (i.e., 20% for five fingers). To reduce the chance of including channels whose performance was only spuriously above chance, the threshold accuracy for model inclusion was set as the 95% value of the binomial cumulative distribution function for $N=225$ trials (i.e., the size of the training set) and $p=0.2$.

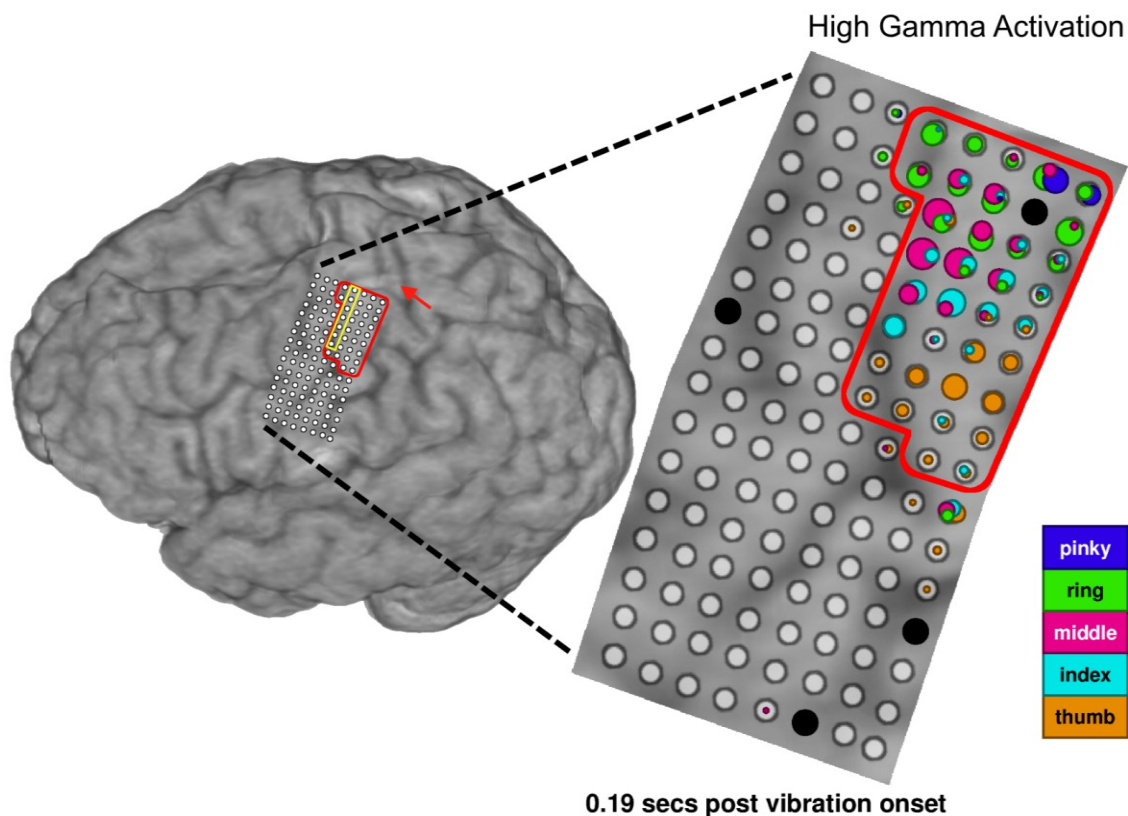


Figure 4.1. hdECoG Grid Coverage and spatial map of high gamma responses. (left) An oblique lateral view of the patient’s three-dimensional MRI reconstruction is shown. The red arrow points to the postcentral analogue of the primary motor cortex hand knob for reference. The red outline depicts the postcentral grid snippet used in Figures 4.3 and 4.7. The yellow outline surrounds the seven electrodes whose single trial responses are plotted in Figure 4.5. (right) A zoomed-in view of the hdECoG grid and underlying cortex is used as a background for plotting finger responses, or statistically significant ($p < 0.05$, FDR-corrected) increases in high gamma power relative to baseline, time-locked to 0.19 seconds after vibration onset. This time was chosen as it contained the largest magnitude aggregate increase across the hdECoG grid. The diameter of each circle is proportional to the z-scored measure of high gamma power increase, and the color represents the finger being stimulated in accordance with the key in the bottom right. Electrodes excluded from analysis are blackened. The fingers with the largest response at a given electrode are plotted first, and therefore are partially occluded when multiple fingers elicited a high gamma response in that electrode.

4.4 Results

4.4.1 Somatotopy of Spectral Features and Event-Related Potentials

Ordered but overlapping finger representations were observed from the high gamma activations across the hdECoG grid (see Figure 4.1). A clear gradient was apparent from the thumb representation (inferiorly) to the pinky representation (superiorly). Despite this ordering, finger representations in the high gamma band were not totally distinct from one another. Of the 124 sites in the hdECoG grid, 45 showed significantly increased high gamma power relative to baseline during at least one finger stimulation, and a majority (28 of 45, or 62.2%) of those sites were significantly activated for multiple fingers.

Among the high gamma responses, the thumb-specific representation appeared to be the most independent. The average Pearson's correlation coefficient, r , between thresholded high gamma power across the grid was 0.01 between thumb and the other four fingers. For comparison, the average correlation between index, middle, ring, and little fingers and all other fingers was 0.23, 0.34, 0.28, and 0.10, respectively. The little finger correlation with other fingers was low as well, though this was attributable to the low number of sites with significant activation during pinky stimulation. Other than the poor sampling of the little finger representation, a comparable number of sites exhibited significant high gamma activation for each finger—22 sites exhibited thumb activation, 20 exhibited index finger activation, 21 exhibited middle finger activation, and 20 exhibited ring finger activation.

Despite the clear somatotopy evident in the high gamma finger representations, lower frequency features did not exhibit the same degree of finger specificity in the high density grid (see Figure 4.2). Many more sites exhibited task-related changes in low frequency power; of the 124 sites in the grid, 91 exhibited significantly reduced theta power, 81 had reduced mu power, and 82 had reduced beta power. Of sites with significant low frequency power decreases, a higher portion (i.e., than high gamma) exhibited responses to multiple fingers, including 64.8% for the theta band, 79.0% for the mu band, and 70.7% for the beta band. The average correlations between different finger representations were 0.64, 0.67, and 0.69 for theta, mu, and beta bands, respectively, compared to 0.21 for the high gamma band.

We further wanted to test whether the finger representations in these different bands were merely centered in the same locations with different widths, or if the representation centers themselves differed between each band. To test this, we computed the centers of mass of each finger representation for each frequency feature. We plotted the centers of mass and the electrodes with peak activation (see Figure 4.3). As expected, both the centers of mass and peak electrodes show a clear inferior-to-superior ordering from thumb to pinky for the high gamma responses. This pattern is not replicated with high fidelity in lower frequency features. Of more interest than the tighter spacing, however, is the generally weak or nonexistent somatotopic ordering in the centers of mass and the peak electrodes of the low frequency representations. The mu band appears to exhibit separate thumb and little finger representations with confused ordering in between. The representation

peaks in the beta band exhibit some somatotopy that is not replicated in the centers of mass.

The somatotopy of event-related potentials (ERPs) for each finger was also analyzed (see Figure 4.3). The representation centers and peaks for the ERPs showed a stronger similarity to the high gamma representation than did the low frequency features. Though the centers of mass show a tighter clustering, they exhibit a rough inferior-to-superior digit ordering, albeit with slight confusion between middle and ring fingers. Among the representation peaks, four of the five ERP peaks are within one electrode of their corresponding high gamma peaks. This suggests that finger representations in ERPs and high gamma responses share similar centers, with differing extents of representation overlap. Indeed, the average spatial correlation across fingers is 0.25 for event-related potentials, both higher than high gamma (0.19), and much lower than for low frequencies (0.64-0.69).

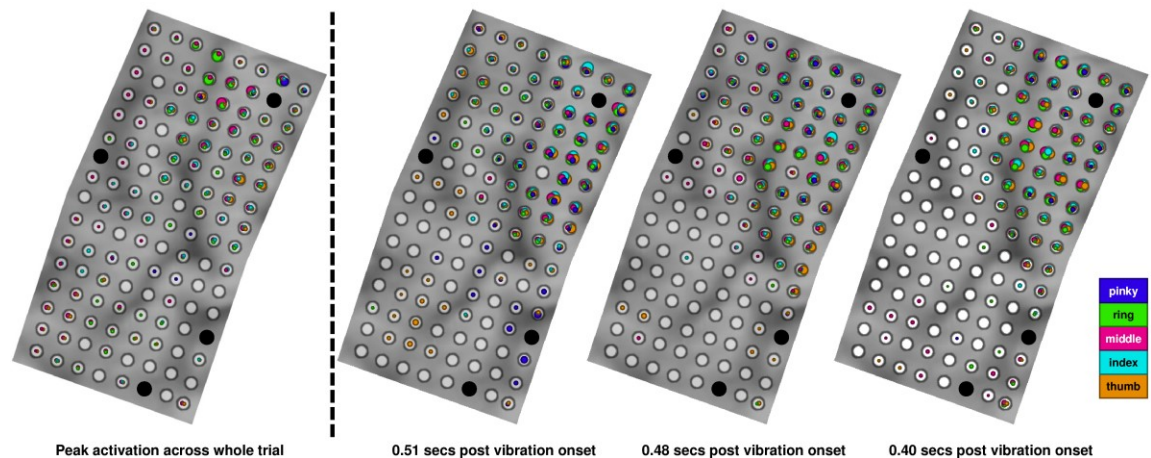


Figure 4.2. Spatial map of event-related potential amplitude and low frequency responses. These maps depict the z-scored absolute value of significant changes in amplitude (ERPs, left) or the strength of the decrease in low frequency power (three rightmost maps). The diameter of each circle is proportional to the z-

scored measure of amplitude change or power decrease, and the color represents the finger being stimulated in accordance with the key in the bottom right. Electrodes excluded from analysis are blackened. The circle diameters are on the same relative scale as the high gamma plot in Figure 4.1. Since the timing of event-related potentials varies greatly by channel, the peak amplitude change was used to determine circle diameters; low frequency maps were created for the time periods with the largest aggregate magnitude decrease across the entire grid.

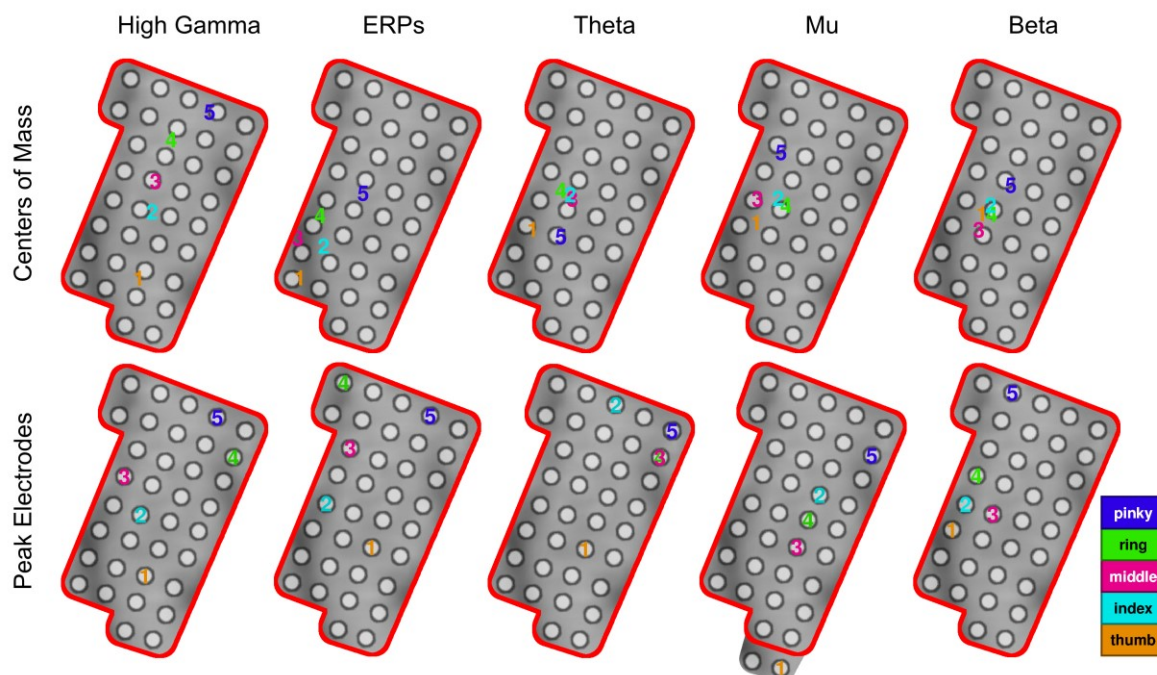


Figure 4.3. Finger Representation Somatotopy. (top row) The centers of mass, in two-dimensional electrode coordinate space, are plotted on the top right corner of the hdECoG grid for each feature type. Numbers 1 through 5 designate the first digit (thumb) through the fifth digit (pinky). (bottom row) The electrodes with the strongest response for a given finger for each feature type is plotted on the corresponding brain snippet. The placement of the postcentral snippet within the context of the larger hdECoG grid is depicted in Figure 4.1.

4.4.2 Timing of Activation

To ascertain the temporal representation of the vibration stimuli, we averaged the dynamic high gamma responses for each stimulation site across all electrodes with any time window of significant ($p < 0.05$, FDR-corrected for multiple comparisons across channel and time windows) power increase (see Figure 4.4).

These traces exhibited early peaks with subsequent attenuation in response magnitude. Peak activation ranged from approximately 170 ms (thumb and index finger) to 200 ms (middle and little fingers), with no clear somatotopic ordering to the differentially timed peaks between the finger stimulations. Aggregate activation for index, middle, and ring fingers returned to nearly baseline levels by approximately 200 ms after the cessation of stimulation, though pinky and thumb responses do not appear to fully return to baseline until approximately 400 ms post offset.

Event-related decreases in low-frequency power peaked later in the trial, ranging across fingers from 450-570 ms (theta), 450-570 ms (mu), and 320-450 ms (beta). Averages of the event-related potential magnitudes revealed a much more complex pattern of timing with many minor peaks. Furthermore, distinct deflections were apparent corresponding to the onset and offset of vibrational stimuli. Onset peaks, defined heuristically as the maximum average magnitude during the stimulation period, ranged from 90-220 ms. Peak magnitudes after vibration offset ranged from 130-320 ms post-offset (i.e., 630-820 ms post-onset).

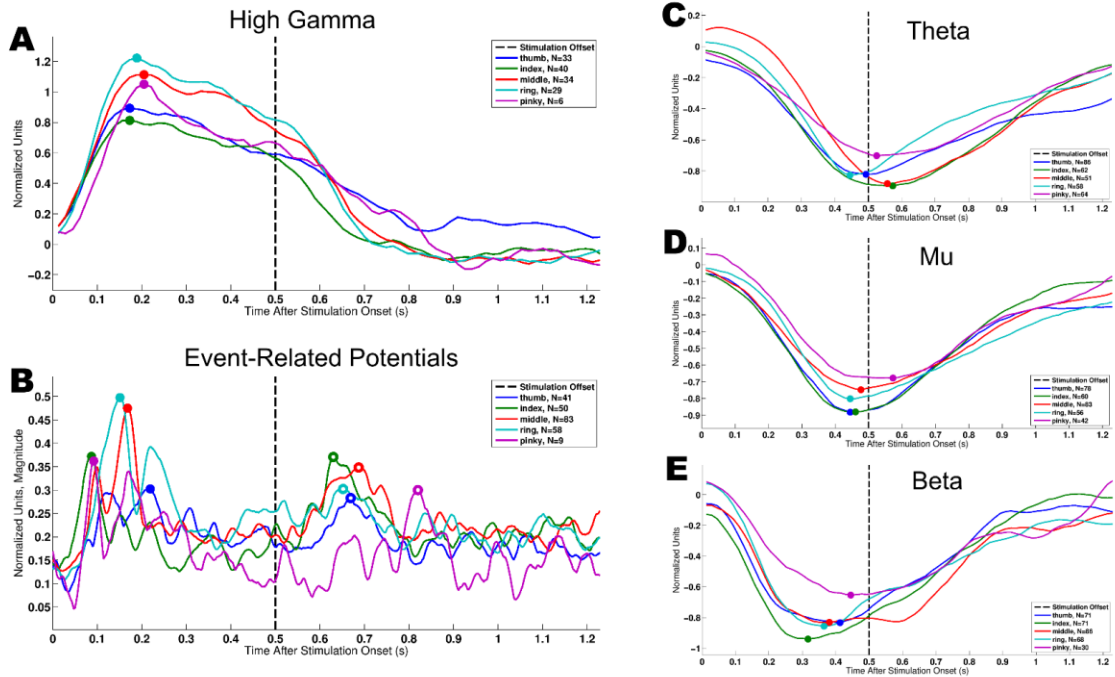


Figure 4.4. Temporal profiles of spectral and amplitude representations of finger vibrations. (A) The high gamma traces for all electrodes with any significant activation in any post-stimulus time window ($p < 0.05$, FDR-corrected) is averaged separately for each finger response. (B) The average magnitudes of all significant amplitude responses for each finger is shown. (C-E) The averages of all sites with significant task-related low frequency decreases are shown for theta, mu, and beta bands. Colored dots correspond to: (A) the largest increase, or (C-E) the largest decrease for a given averaged finger response. In (B), solid dots correspond to the peak magnitude during stimulation, while empty dots denote peak magnitude after stimulation offset. Legends in each plot detail how many sites were used to compose each averaged finger response.

4.4.3 Single Trial Responses

Finger vibrations elicited robust single-trial high gamma responses which were highly specific to which finger was stimulated. Figure 4.5 (top) shows single trial rasters of the high gamma responses, sorted by stimulation site, for seven adjacent electrodes. A clear progression is observable from superior to inferior electrodes, with selectivity shifting from ring finger to middle finger (by the third electrode) to thumb by the most inferior electrode. Similar patterns were

observable in each of the four columns of the high-density grid with substantial coverage of the postcentral gyrus. Low frequency features exhibited robust single-trial responses, though the selectivity of these responses was much lower. Figure 4.5 (bottom) shows beta responses, as a representative low frequency feature, for the same seven electrodes as the high gamma responses in Figure 4.5 (top). Responses are evident (and significant) for all five fingers in the two most superior electrodes, and for all fingers except pinky in the remaining five electrodes. Thumb activation shifts from least active in the most superior electrode to most active in the most inferior electrode.

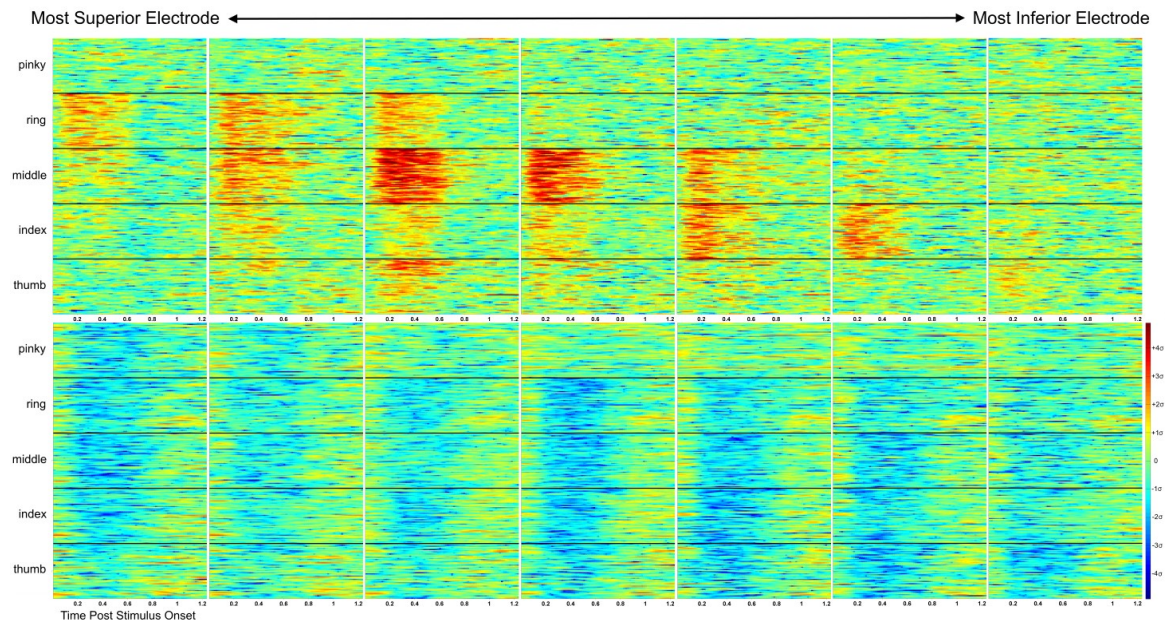


Figure 4.5. Single trial high gamma and beta responses for six adjacent electrodes. High gamma (top) and beta (bottom) responses are shown for the same six adjacent electrodes, arranged along the inferior-superior axis of the grid (depicted in Figure 4.1). Responses from the most superior electrode, from the top row of the grid, are depicted in the leftmost sub-plot. Each row within each sub-plot is a trial, and the horizontal axis represents time after the onset of the stimulus. Trials have been reordered so that all thumb trials appear together, followed by all index finger trials, etc., and the transitions between finger types are marked with black lines.

We observed an attenuation in the high gamma responses between early (i.e., first third) and late (i.e., last third) trials. This attenuation was observable in a majority of sites with significant post-stimulus activation (51 of 82, 62.2%). The degree of attenuation, averaged across significantly attenuated sites, for late trials ranged from approximately 29% (ring finger) to 41% (thumb) relative to peak activation for early trials. These values were obtained by fitting a linear regression model with no constant term to the relationship between the averaged early and late trials high gamma responses. Repetition effects were also observed in low-frequency features, with 95.0%, 91.2%, and 83.3% of significantly activated channels in theta, mu, and beta channels exhibiting significant response adaptation. Smoothed amplitude responses also exhibited significant repetition effects (in 93.3% of significantly activated sites), though no consistent pattern was evident in whether those effects constituted a net amplification or attenuation of the resulting ERP. A separate regression analysis revealed no significant effect of the latency of finger-specific repetition in the smoothed amplitude or any of the frequency bands ($p > 0.05$, FDR-corrected for multiple comparisons) when also accounting for the overall trial number. That is, no finger-specific repetition effects were observed, but rather a global adaptation to the overall task.

4.4.4 Temporally-Restricted Decoding Analyses

As a way to validate the robustness of the single trial responses and pinpoint the timing of peak finger somatotopy across the whole high-density grid, we performed a single-trial classification analysis in windows with fixed timing relative

to the onset of stimulation across trials. We also varied the degree of smoothing to approximate the longevity of these representations in the grid. We performed classification analysis on data that was smoothed (within trials) with window centers spanning 16 ms (i.e., no smoothing for spectral features, 16 ms smoothing for amplitude features), 112 ms, and 240 ms. Across all smoothing widths, high gamma features outperformed all other feature types, with peak accuracies ranging from 96.0% at 240 ms post-stimulus onset without smoothing to 98.8% (at 220 ms post-stimulus onset) with a smoothing width of 240 ms. Low frequency models performed much more poorly, peaking at roughly 50% accuracy with no smoothing and up to 60% with a smoothing width of 240 ms. Smoothed amplitude models exhibited two peaks in classification accuracy corresponding to stimulation onset and offset, consistent with the temporal profile of ERPs shown above. Within these peaks, smoothed amplitude models consistently outperformed the low frequency models. At higher smoothing widths, the offset period provided slightly better decoding than the onset peak. Smoothed amplitude model accuracies peaked at 83.2% (at onset peak, 220 ms) and 96.4% (at offset peak, 680 ms), respectively, for smoothing widths of 16 ms and 336 ms, respectively. For high gamma models, no secondary peak in classification was observed time-locked to the offset of vibratory stimulation, and thus smoothed amplitude models far outperformed high gamma models (and low frequency models) in the period following the cessation of the stimulation.

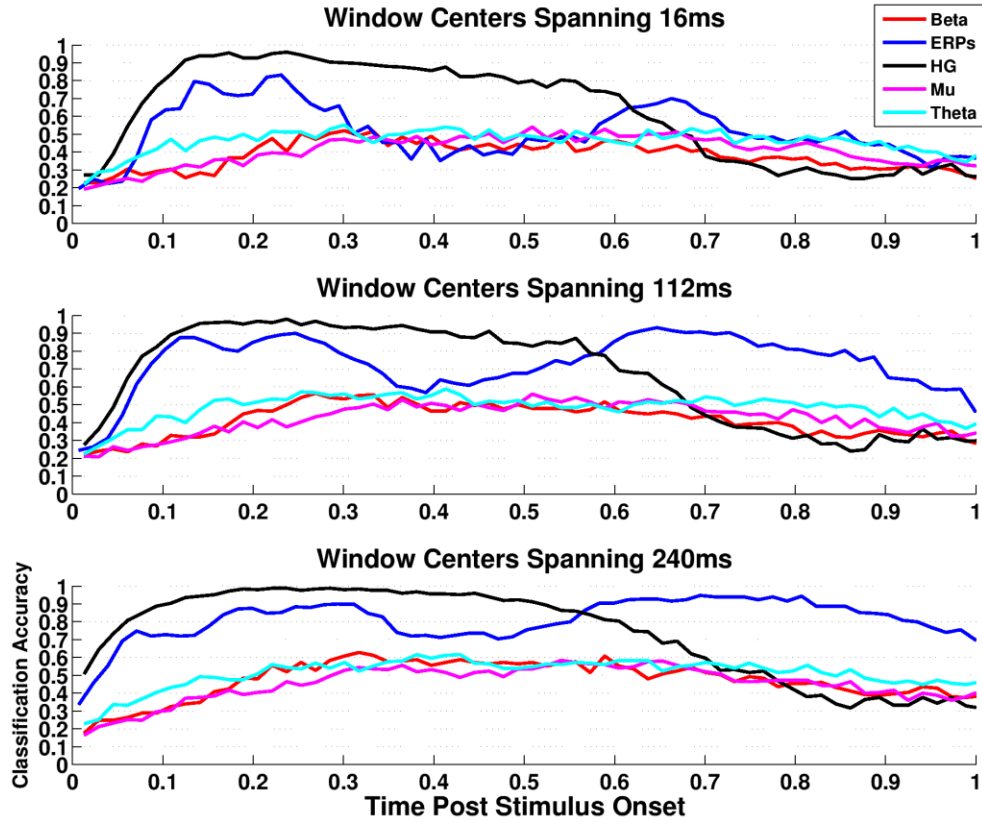


Figure 4.6. Time-restricted classification accuracy across feature types and smoothing kernel widths. The cross-validated classification accuracy in time windows time-locked to stimulus onset are plotted. Classification results are plotted for high gamma (black), smoothed amplitude (blue), theta (cyan), mu (magenta), and beta (red) features are shown at each smoothing kernel widths. Smoothing over window centers spanning 16 ms (no smoothing for spectral features, 16 ms smoothing for ERPs), 112 ms, and 240 ms are shown. A clear secondary peak in decoding accuracy emerges for smoothed amplitude feature models which is not apparent for the models with spectral feature inputs.

4.4.5 Comparing High Gamma Responses to Vibration and Movement-Related Sensation

The representations of finger vibration in the high gamma responses were also compared to the representations of sensory feedback during finger movement. To exclude motor activity to the extent possible, only data from the postcentral region of interest (ROI) highlighted in Figure 4.7 were considered for the comparison. Furthermore, only the first 25 trials of stimulation of each finger was

used in this comparison to remove the effects of repetition detailed above. Within this ROI, movement produced an ordered somatotopy in the postcentral gyrus, visible in the digit representation centers of mass. The representations of movement-related sensory feedback were not identical to those of vibration, however, which is expected due to the different sensory modalities implicated in the task (i.e., proprioceptive and cutaneous feedback vs. cutaneous stimulation alone). In particular, the centers of mass appeared to be more tightly clustered, reflecting greater overlap between the finger representations. The average spatial correlation between finger representations within the postcentral ROI was -0.08 for vibration responses vs. 0.56 for movement-related sensory responses. Motor-related feedback exhibited higher aggregate activation than vibrational stimulation. Of the 139 (channel, finger) pairs in the postcentral ROI which were significantly activated during either vibration or movement, 103 had significantly higher motor responses, compared to only 10 with significantly higher sensory responses ($p < 0.05$, FDR-corrected for multiple comparisons).

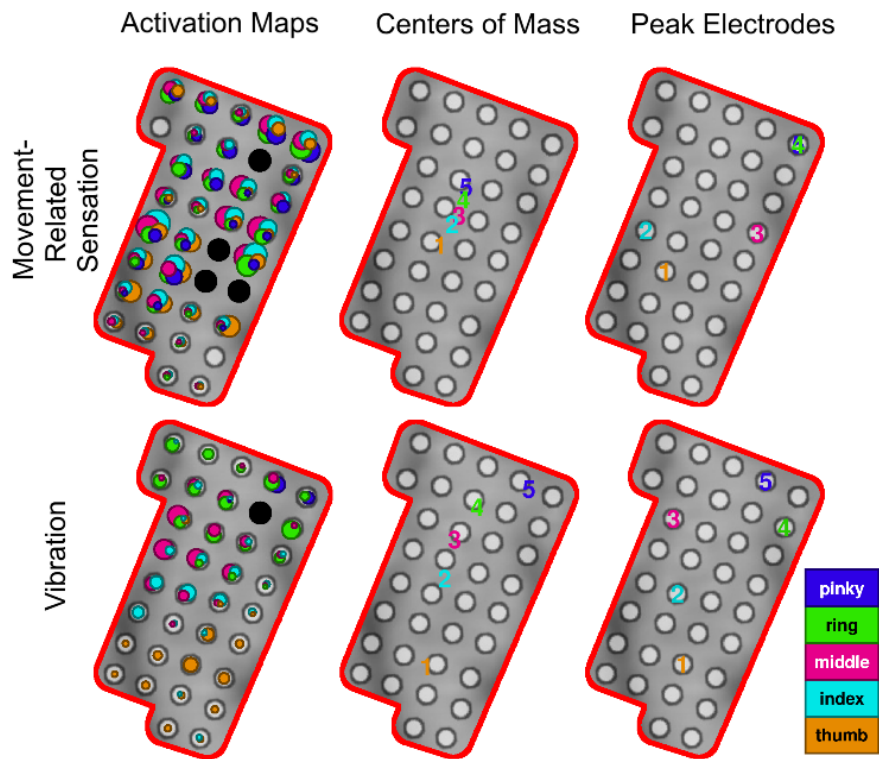


Figure 4.7. Comparison between vibration responses and movement-related sensory high gamma responses. Significant activation at 0.19 seconds post stimulus onset (top left) and 0.03 seconds prior to peak finger flexion in the motor task (top right) are depicted. The diameters of the circles depict high gamma power increases z-scored with respect to the baseline period. They are on identical scales, but a different scale from Figures 1 and 2. The placement of the postcentral snippet within the context of the larger hdECoG grid is depicted in Figure 4.1. The centers of mass (middle row) and representation peaks (bottom row) are depicted for both vibration (left) and motor (right) tasks.

4.5 Discussion

High-density electrocorticography (hdECoG) has been used in several studies to investigate the organization of speech-related networks in humans (Bouchard and Chang, 2014; Mesgarani et al., 2014; Mesgarani and Chang, 2012), but this is the first study to examine the somatotopy of postcentral gyrus finger sensory representations in hdECoG. The signal-to-noise ratio of hdECoG recordings is

sufficient to characterize and classify neural responses to vibrotactile stimuli in single trials. The spatial resolution of hdECoG used here (3 mm center-to-center vs. 1 cm for standard ECoG) was consistent with the previously reported spacing between digit representations in postcentral gyrus (1-5 mm, (Martuzzi et al., 2014)).

There are several strengths and weaknesses of characterizing finger representations with ECoG rather than more traditional functional magnetic resonance imaging (fMRI). The high temporal resolution of ECoG recordings relative to fMRI allows for the characterization of temporal and spectral dynamics of sensory responses within trials. The signal-to-noise ratio of ECoG signals permits characterization of single-trial responses, facilitating investigation of between-trial changes in neural responses (e.g., response adaptation) and classification of stimulation site. This high signal quality also permits the evaluation of spatial organization in individual subjects, reducing spatial blurring inherent to group analyses. Understandably, ECoG recordings are rare and restricted to patients with medically refractory epilepsy. The placement of grids is determined by clinical need and is limited to areas that could potentially contribute to seizures or to important brain functions. fMRI records from the whole brain (including voxels deep in sulci which are not generally accessible by surface ECoG grids) in normal subjects. Most commonly, the spatial resolution of ECoG recordings is 1 cm, inferior to that of fMRI. Because our patient's previous work up suggested ictal onset in primary or secondary somatosensory cortices, extra-operative monitoring included hdECoG recordings over primary sensorimotor hand area, offering an unprecedented

opportunity to map the electrophysiology of individual human finger representations

In this study, we characterized time- and frequency-domain neural responses to vibrotactile stimulation. We found that high gamma band responses most replicated the findings from the large body of literature on finger representations measured by cortical stimulation and fMRI. Event-related potentials also exhibited an ordered somatotopy with weak similarity to high gamma maps. The existence of somatotopy in the finger ERPs mirrors previous studies of evoked responses to peripheral nerve stimulation in ECoG arrays (Sutherling et al., 1992) and magnetoencephalography (Baumgartner et al., 1991), though we do not find totally distinct representations as inferred from the dipole models (Sutherling et al., 1992). Low frequency features, however, in the theta, mu, and beta bands contained more diffuse finger representations. In addition to having a larger degree of overlap between finger responses, the centers of mass for individual digit representations lacked the canonical inferior-to-superior ordering from first to fifth digits. This implies that low frequency responses to vibrotactile stimulation are not simply spatially blurred versions of high gamma representations. Together with poor classification accuracy by low frequency models, our study suggests that finger representations are simply not well characterized or differentiated by low frequency power. Their reliable task-related power changes point to a role in somatosensory processing, though that role likely corresponds to less stimulus-specific tuning of neuronal excitability and facilitating communication between brain areas (Miller et al., 2012; Neuper and Pfurtscheller, 2001).

The short cycle duration of neural fluctuations in the high gamma band allows their modulation to be temporally localized with relatively high precision relative to lower frequency signals. In this study, we observed that the high gamma responses to vibration peaked ~200 ms after stimulus onset and declined during the stimulus period. This is substantially longer than reported response latencies from the periphery to cortex, estimated to be approximately 10-20 ms (DiCarlo and Johnson, 1999; Mountcastle, 1957; Woolsey et al., 1979), but it is important to note that we are reporting the response peaks, rather than the onset of processing. Spectral methods are not ideal for determining the onset of activity, since filtering and power estimation techniques each smooth and downsample the underlying phenomena. The peak times of the high gamma responses corresponded strongly to the early peaks in ERP magnitude, though interestingly, ERPs associated with stimulus offset did not correspond to any observable peaks in the high gamma responses.

High gamma responses to movement in the postcentral gyrus, receiving cutaneous and proprioceptive sensory feedback from the fingers, generally exceeded high gamma responses to passive vibrotactile stimulation. In addition to being larger, movement-related sensory responses also covered more cortical area, yielding a much greater spatial correlation between finger representations in the postcentral gyrus (average $r = -0.08$ for vibrotactile responses, 0.56 for movements). While these differences make intuitive sense due to the multiple modalities of sensory feedback provided during a movement, it is possible that the differences arise from other differences between the two tasks. For example, the tracking glove

likely provided a small amount of somatosensory feedback to adjacent fingers, and the cued movements of individual fingers likely involved obligatory movements of adjacent fingers. These factors likely contributed to the observed overlap, but seem unlikely to fully explain it. For example, high gamma responses to vibrotactile stimulation of the fifth digit occurred in only two electrodes in the top right corner of the grid, but high gamma responses during cued movements of this digit extended to electrodes spanning ~21 mm (i.e., extending to the seventh row of the grid).

Consistent with studies in other sensory domains, particularly visual (Engell and McCarthy, 2014) and auditory (Eliades et al., 2014), we observed repetition suppression of the cortical responses to vibrotactile stimuli. The effects were present in the high gamma and low frequency responses, as well as in the event-related potentials. This effect appeared to be unrelated to the latency between repeated stimulations at individual fingers, indicating that it consisted of a global adaptation to the overall task. It is important to note that this effect, while significant, was insufficient to preclude high single trial decoding accuracy—over 98% accurate stimulation site classification was achieved with 240 ms smoothing.

This study provides electrophysiological evidence that somatotopic organization exists in the finger representations in human postcentral gyrus at 3 mm scale. Inferior to superior ordering of representations from first to fifth digits were most apparent in the high gamma responses. These responses had sufficient signal-to-noise ratio and robust spatial patterns to allow classification of the stimulation site in single trials. Despite the apparent order in the hdECoG finger

responses, they nonetheless overlapped. While it is important to replicate these findings in more patients, our study provides evidence that this overlap is present at the neuronal population scale in a single subject (i.e., the overlap is not an artifact of spatial blurring in group analyses). The spatial and temporal resolution of hdECoG make it well suited to characterizing the somatotopic organization and dynamics of finger vibration. As more subjects with hdECoG grids over sensorimotor cortex become available, it will be important to investigate how more naturalistic, complex, and/or time-varying somatosensory stimuli are represented in the postcentral gyrus.

4.6 Study Acknowledgements

Data analysis for this study was supported by the National Institute of Neurological Disorders and Stroke under Grant 5R01NS088606-02.

Chapter 5

Long-Term Outlook of Electrocorticography for Functional Mapping and Brain-Machine Interface

5.1 Abstract

Electrocorticography (ECoG) has been discussed at length in this thesis, but it is important to note that ECoG is one of many techniques for assessing cortical function. The optimal technique for a given application depends on the relative importance of factors including: spatial accuracy, temporal accuracy, extent of coverage, invasiveness, portability, etc. Stimulation, microelectrodes, fMRI, and EEG are all common techniques for characterizing task-related cortical processing that may be used as alternatives to ECoG recording. So, where does ECoG fit into this landscape? When is ECoG the appropriate technique to use, and what is still unknown about ECoG's relative utility? These issues are explored in this chapter.

5.2 Electrocorticography: An Evolving Modality

5.2.1 Different Types and Scales of ECoG Implants

ECoG is far from a homogeneous technique; in fact, it is closer to a family of recording modalities. In general, ECoG electrodes capture signals from populations

of neurons at millimeter to centimeter scale. ECoG electrodes can either be implanted as: (1) strips or grids of surface contacts, or (2) depth electrodes or stereotactic EEG (SEEG). Grids or strips may further be subdivided into subdural or epidural implants. Within each category, distinctions are often made between different categories of electrode size and spacing. Surface electrodes with 3-4 mm spacing (vs. 1 cm spacing for traditional ECoG arrays) are an emerging modality referred to within this thesis as high-density ECoG (hdECoG). Micro-ECoG recordings are smaller still, with common electrode spacings of approximately 1 mm and microwire widths less than 100 microns (Kellis et al., n.d.). Depth electrodes vary in their electrode spacing, and often incorporate arrays of microcontacts (Worrell et al., 2008) or project microelectrodes from the distal tip of the larger depth implant (i.e., Behnke-Fried depth electrodes, (Fried et al., 1999)). These high resolution depth contacts differ qualitatively from other ECoG implants due to their ability to record single unit activity. Single unit recordings in humans made with depth electrodes will not be discussed in further detail in this chapter, but are given comprehensive treatment in a recent review (Cash and Hochberg, 2015).

While depth electrodes are the preferred implant type for invasive seizure monitoring in many clinical centers, they are (in my opinion) not ideally suited to functional mapping or BMI applications. In general, the dominant axis of these implants is orthogonal to the brain's surface and thus the dominant plane of cortical motor and language representations. In practice, this means that many recording sites on the depth electrode reside in the white matter and subcortical structures.

On the other hand, depth electrodes are rarely (if ever) implanted with regular spacing. This makes depth electrodes poorly suited to cortical surface mapping, though they can be an important tool for probing representations of speech and language in structures which are typically overlooked by ECoG researchers (e.g., thalamus, basal ganglia, white matter, etc.). Additionally, depth electrodes may sample sulcal populations which are not accessible to traditional ECoG implants. While depth electrodes can certainly be used for BMI purposes or functional mapping (e.g., BMI signals and functional maps from Subject 2 of Chapter 3 were obtained from depth electrodes), surface ECoG provides better coverage of clinically relevant cortical language and motor representations. Throughout the remainder of this chapter, the term ECoG will be used almost exclusively to refer to surface electrodes rather than depth electrodes.

5.2.2 ECoG Technology Developments and hdECoG

A number of large technological advances loom on the horizon for cortical surface recordings with the potential to revolutionize functional mapping and ECoG-based brain-machine interfaces. As emphasized above, there is already a large variety in the scale of ECoG electrodes available for human implantation. Higher density (i.e., than even micro-ECoG arrays) are currently being explored in relatively large, flexible arrays. Two notable recent studies have demonstrated recordings from electrodes spaced by 30 microns (Khodagholy et al., 2015) and 500 microns, with active electronics at the electrode site (Viventi et al., 2011). At these scales, neural phenomena not previously accessible at the cortical surface are being

observed. NeuroGrid is capable of recording neuronal spikes (Khodagholy et al., 2015); Viventi et al. were able to observe spiraling propagation patterns of seizures in their array recordings (Viventi et al., 2011). By dramatically increasing channel counts with custom amplifiers, these arrays do not have to record from as limited an area as current micro-ECoG arrays. The array designed by Viventi et al. is 60 x 60, spanning roughly 3 cm x 3 cm. These arrays, if they can be translated to human use, likely represent the future of intraoperative and inpatient recordings for seizure mapping and thus ECoG-based functional mapping. Time will tell whether implants at this scale will be ideal for long-term BMI use. Obviously, movement of a grid with micron-scale spacing could cause signals of interest to move to different electrodes in the array. These devices will also necessitate a new wave of amplifiers to accommodate the high channel counts. Beyond simply increasing the scale of hardware, high channel counts will also tax software designed to perform signal processing and machine learning in real-time.

Simultaneous to improvements in scale, several companies, including Ripple (Guillory et al., 2011) and Clnatec (Charvet et al., 2011), are developing wireless ECoG recording systems. A functional wireless system for inpatient seizure and functional mapping would be initiate a paradigm shift in ECoG testing. Most obviously, wireless technology would allow patients to move more freely throughout their rooms and perhaps participate in slightly more movement-intensive activities during functional mapping. More importantly, however, a wireless grid might shift the balance of clinical risks and rewards in favor of at-home monitoring. The lack of an infection-prone transcutaneous connector would

enable clinicians to remotely monitor patients on a longer time scale. This would allow patients longer to remain on their seizure medications and wait long enough to experience several of their medically-resistant seizures. This would also create more time for functional mapping and research activities, and potentially make the subjects more likely to consent to testing in their home environment. Unfortunately, the regulatory hurdles for these systems have stagnated the proliferation of these systems into the marketplace. Clnatec appears to be the closest to clinical deployment, as they are currently in the process of starting a clinical trial of their system in France.

While wireless ECoG recording systems and arrays with dramatically smaller scales are being developed, arrays with 3-4 mm spacing (i.e., hdECoG arrays) represent a much more modest innovation, but one that has been fairly scientifically lucrative to date. hdECoG arrays are implanted relatively infrequently for seizure mapping, though their clinical use is increasing and can be extremely useful when the seizure focus is likely to neighbor or reside in eloquent cortex. Chapter 4 of this thesis describes the use of hdECoG in a preliminary somatosensory mapping study with a single subject. In addition to my thesis work, our group enabled the subject from Chapter 4 to control individual finger movements of the MPL using high gamma activity from the hdECoG implant (Hotson et al., 2015). Other groups have used hdECoG recordings to study the organization of language perception (Mesgarani et al., 2014) and production (Bouchard and Chang, 2014) near the Sylvian fissure.

In my opinion, hdECoG arrays are ideally spaced for functional mapping and BMI purposes. Three to four millimeter spacing not only allows gyri to be sampled by multiple electrodes, but also appears to be commensurate with the scale of finger and phonetic representations along the major axes of the postcentral gyrus and the Sylvian fissure, respectively. This presents a clear advantage over traditional ECoG arrays with centimeter spacing, which spatially alias these representations. hdECoG electrodes also enjoy a clear advantage over micro-ECoG implants in that their impedance (i.e., higher than ECoG but lower than micro-ECoG) allows them to be sampled using clinical neurophysiology systems, rather than with custom research hardware. In addition to reducing the barrier to entry of recording these signals, this distinction also allows these arrays to be implanted at the discretion of clinicians rather than solely for research purposes. Perhaps more nuanced are the advantages of hdECoG's intermediate scale relative to current micro-ECoG arrays. Micro-ECoG arrays sample the cortical surface on scales comparable to cortical columns (Mountcastle, 1997), but are currently so small that their surgical placement relative to patients' functional anatomy is extremely variable. In addition to decreasing the number of these implants which cover regions of interest, it also increases the difficulty of meaningfully aggregating results across multiple subjects.

5.2.3 Features of the ECoG Signal and the Emerging Dominance of the High Gamma Band

There are a number of frequency and time domain features that can be extracted from the ECoG signal. Time-domain features including event-related

potentials (ERPs) and slow-cortical potentials (or local motor potentials) have been used to infer function for decades, dating back to the pioneering evoked potential studies of Woolsey (Woolsey et al., 1979, 1942). ERPs are fast deflections in the raw voltage recorded from ECoG electrodes and emerge in trial-averages that cancel out zero-mean noise. ERPs are often thought to represent phase-aligned low frequency afferent information delivered via the thalamus (Pfurtscheller and Lopes da Silva, 1999b). The sign of ERP peaks is heavily dependent on electrode referencing—bipolar montages, distant electrode references, and common average references all produce different ERP shapes. Whereas ERPs are waveforms with complex temporal structure that emerge from trial-averaging, some information can be extracted from the time domain in single trials. The local motor potential (LMP) is simply the instantaneous value of the ECoG signal, which is typically extracted by smoothing the ECoG signal over hundreds of milliseconds [used in Chapter 4 and (Schalk et al., 2007)] to seconds (Acharya et al., 2010; Hotson et al., 2014). Similarly to ERPs, LMPs do not exhibit any consistent sign in their deflection above/below zero—their correlations with behavior can be positive or negative and are affected by referencing.

Though they have not yet seen much adoption in online applications, time-domain features of the ECoG signal are commonly used for functional mapping. Somatosensory evoked potentials (SEPs) are a common technique for mapping sensorimotor cortex (Wood et al., 1988; Woolsey et al., 1979), and for intraoperatively determining the boundary between pre- and postcentral gyrus,

which can often be difficult to localize via surface landmarks alone (Cedzich et al., 1996).

Spectral features are also commonly extracted from the ECoG signal. Low frequency signals historically extracted from EEG signals are also extracted from the ECoG signal, notably in the theta (4-8 Hz), mu (8-12 Hz), and beta (14-30 Hz) bands. Unlike ERPs, low frequency signals typically only decrease in power relative to baseline in response to a stimulus. Low frequency power modulations occur over wide areas, but exhibit relatively little selectivity to stimulus or behavioral features. It is becoming increasingly common to examine the phase of low frequency ECoG oscillations, especially in relation to the timing of high frequency activity. The phase of low frequency signals at single sites has been demonstrated to modulate the timing of population activity (Canolty et al., 2012, 2006; Miller et al., 2012). The degree of coupling between high and low frequencies has been shown to be responsive to task parameters (Canolty et al., 2012), but to my knowledge has not been used explicitly for mapping or BMI purposes.

This thesis includes extensive use of high gamma band (70+ Hz) activity increases as an index of cortical activation. Unlike low frequency features of the ECoG signal, high gamma activity exhibits very high selectivity to stimulus and behavioral variables (Lachaux et al., 2012). High gamma features are especially attractive for online applications, since accurately estimating the power requires much smaller windows than for lower frequencies; cycles of an 80 Hz sinusoid are one fourth as long as cycles of 20 Hz beta oscillations and one sixteenth as long as cycles of 5 Hz theta oscillations.

Many previous systems for functional mapping and BMI with ECoG have taken an agnostic approach to frequency bands. BrainTV (Lachaux et al., 2007b) and a recently demonstrated trial-based functional mapping (Cheung and Chang, 2012) both provide simultaneous visualization of low and high frequency modulations, while SIGFRIED (Schalk et al., 2008a) combines measures of low and high frequency signals into a single metric of task-relatedness at each site. Several past online ECoG BMI studies have pooled features from across low and high frequencies (Leuthardt et al., 2004; Schalk et al., 2008b; Yanagisawa et al., 2012). It is unclear why these studies cast such a wide net, especially in online systems where computational resources are at a premium. The development of the online functional mapping system (described in Chapter 2) has provided our team with a wealth of anecdotal experience of the superior specificity of high gamma increases. Although not shown, attempts to generate equivalent low frequency functional brain maps resulted in such wide areas of activation that they were essentially uninterpretable. Alas, it was not particularly surprising in Chapter 4 that high frequency power exhibited a much more somatotopic representation than its lower frequency counterparts.

While the neurophysiological role of low frequency power remains of scientific interest, it is arguably because of its poor selectivity (and thus applicability to functional mapping and BMIs). In other words, why do these signal features exhibit such robust task-related modulation (implying a role in task-related processing), but yet encode so few features of the task? Several theories have attempted to address this issue, including the communication through coherence

(CTC) hypothesis which proposes that coherent low frequency signals form a channel of communication between distant brain areas (Fries, 2005). The more recently proposed function through biased oscillations hypothesis posits that cortical inhibition—and thus the amount of high gamma activity—is governed by the raw potential, reflecting the summed influence of shifting signal bias (i.e., LMP) and peaks in low frequency oscillations (Schalk, 2015). While it is possible that the investigation of these theories or cross-frequency coupling will illuminate a role for low frequency signals in online applications, it seems that there is currently limited rationale for extracting these features and including them in BMI models. In addition to providing very little benefit in decoding accuracy, low frequency features require longer spectral estimation windows, adding a feedback delay and potentially (depending on the flexibility of the online system) sub-optimally extending the extraction window of high gamma features. While extraction of amplitude features is theoretically not subject to this limitation, in practice the amplitude achieves peak correlation with movement parameters after considerable smoothing (Acharya et al., 2010; Hotson et al., 2014). Furthermore, extracting 2-3 additional features per electrode increases the number of coefficients to be fit in online decoding models and/or needlessly inflates the number of statistical tests performed (and thus corrected for) in functional mapping systems.

5.3 Alternative Techniques for Recording Neural Activity for Mapping and Brain-Machine Interface

Electrocorticography (ECoG) occupies an intermediate or “mesoscopic” spatial resolution relative to other techniques for recording human neural activity. Microelectrodes provide the ability to record the spiking rates of single neurons or local field potentials, with a total coverage area on the order of millimeters. Functional magnetic resonance imaging (fMRI) estimates neural activity indirectly and noninvasively across the whole brain by measuring the oxygenation of neural tissue that correlates with local metabolic needs, with spatial resolutions of ranging from 2 to 125 mm³ depending on study parameters. Electroencephalography (EEG) is a noninvasive alternative to ECoG, measuring cortical electrical activity from the scalp, with a relatively poor ability to spatially localize neural activity. In this section, each of these technologies will be briefly compared to ECoG, with a specific focus on their use in functional mapping and brain-machine interface (BMI).

5.3.1 Microelectrodes: Spike Firing Rates and Local Field Potentials

Microelectrodes have been a favored tool of neuroscientists for decades for their ability to record the action potentials of individual neurons. Single unit animal studies arguably form the backbone of the neurophysiological knowledge base, as

studies have extensively (and painstakingly) recorded the behavioral and environmental correlates of neurons recorded across multiple electrode insertions across many animals and species. Single unit recording sessions generally involve the subject performing some task of interest while its skull is connected to a stereotactic frame for precise placement of the recording electrode. The microelectrode's placement may be performed coarsely at first to ensure that the recording element is in the study's region of interest; subsequent fine manipulations of the placement can be used to increase the quality of the recording. Given this level of precision, microelectrode recordings are the gold standard for temporal resolution and fidelity to the underlying neuronal circuitry. This precision comes at the expense of wide area coverage, however, and limits the ability to record from multiple neurons simultaneously.

As a slight compromise between precision and coverage area, implanted arrays of microelectrodes have become increasingly common. Microelectrode arrays (MEAs) allow neurons to be recorded from tens to hundreds of insertions (and thus, neurons) simultaneously. MEAs therefore provide researchers with the ability to differentiate task-related correlations (i.e., functional interactions) from task-unrelated noise in neuronal firing. These advantages are offset somewhat by the reduced ability to fine-tune electrode placements and the finite lifespan of long-term microelectrode implantations (Kelly et al., 2007). While some studies report array recordings from multi-year implantations (Gilja et al., 2012; Hochberg et al., 2012; Simeral et al., 2011) these studies are often no longer recording sorted neuronal spikes. Despite these published successes, one study observed that over

half of MEA implants in nonhuman primates failed within a year, for a variety of reasons ranging from mechanical failure to meningeal reaction (Barrese et al., 2013).

MEAs have not been used widely to record human neural activity, though they are beginning to be used in select instances for recording of epileptiform activity (Keller et al., 2010; Schevon et al., 2008) and as a source of neural signals for motor brain-machine interfaces (Collinger et al., 2013; Hochberg et al., 2012, 2006). While seizure recordings are still predominantly performed for research purposes (i.e., rather than clinical seizure mapping), MEAs currently represent the gold standard for providing paralyzed individuals with neural control over prosthetic limbs. BrainGate, a landmark clinical trial of human neuroprosthetic control with an MEA, began in 2004 and was led by Brown University, Massachusetts General Hospital, and the Department of Veterans Affairs. BrainGate provided the first demonstration that a quadriplegic human patient could control of a computer cursor and a robotic with neuronal firing rates (Hochberg et al., 2006). The second phase of this trial, BrainGate2, has grown to include Stanford University and Case Western Reserve University as additional sites. The BrainGate2 team published in 2012 an update of their progress, which included a demonstration of neural control over reach and grasp control by two quadriplegic individuals (Hochberg et al., 2012).

A parallel DARPA-funded initiative, called Revolutionizing Prosthetics, has provided massive gains in both prosthetic upper limb functionality and neural control of those limbs. Revolutionizing Prosthetics has yielded the FDA-approved DEKA Arm (Resnik et al., 2014) and the more advanced, research-grade Modular Prosthetic Limb (MPL) designed by the JHU Applied Physics Laboratory (Bridges et

al., 2011; Johannes et al., 2011). Using training and neural activity modeling techniques developed in nonhuman primates, researchers at the University of Pittsburgh were able to demonstrate seven (Collinger et al., 2013) and then ten (Wodlinger et al., 2015) degree of freedom neural control over the MPL using neural signals derived from MEAs implanted in motor cortex. The latter study showcased the ability of the quadriplegic user to simultaneously control three dimensional reach, three dimensional wrist orientation, three dimensional hand conformation, and grasp aperture. A team at the California Institute of Technology demonstrated an alternative strategy, whereby firing rates from posterior parietal cortex were observed to correlate with movement goals and complete movements in addition to movement trajectories (Aflalo et al., 2015). This study provides a glimpse into a higher-level role for neural control of neuroprosthetic devices, where neural signals merely supervise the implementation of complex movements rather than directly controlling low-level joint angle trajectories. This strategy is one that our team is actively exploring in collaboration with JHU/APL via the development of the Hybrid Augmented Reality and Multimodal Operation Neural Integration Environment (HARMONIE) (Katy et al., 2013; McMullen et al., 2014).

The measurement of spike firing rates has traditionally required daily manual identification and differentiation of spike waveforms (i.e., “spike sorting”). There is a growing body of evidence in nonhuman primates, however, that unsorted spikes (“threshold crossings”), may be used as a surrogate measure of neuronal activity as chronic implantation degrades spike waveforms (Chestek et al., 2013; Fraser et al., 2009; Gilja et al., 2012). The 2012 BrainGate2 study used threshold

crossings rather than sorted spikes, including one subject who was more than five years post implantation (Hochberg et al., 2012). This study provides the strongest example to date of how MEAs may be used for long-term neuroprosthetic control. Doing so, however, requires the extraction of nontraditional features from the recorded signals, with a more indirect relationship to the firing of individual neurons.

In addition to neuronal spiking, microelectrodes can also be used to record low frequency signals (i.e., relative to spiking components) signals called local field potentials (LFPs). LFPs are fairly similar in spectral content to ECoG recordings, but are obtained from much smaller recordings sites which penetrate the cortex. LFPs and spiking rates appear to be highly correlated, making LFPs a common alternative modality to spikes for BMI applications (Andersen et al., 2004; Flint et al., 2013). LFPs encode motor parameters of interest with comparable accuracy to spiking rates (Bansal et al., 2011; Flint et al., 2012a; Mehring et al., 2003; Mollazadeh et al., 2011; Pesaran et al., 2002; Zhuang et al., 2010). Interestingly, LFP signals appear to be more robust and stable during long-term recording than multiunit activity (Flint et al., 2013), and can be used as a control signal for BMIs even in the absence of spiking activity in the same electrode(s) (Flint et al., 2012b). Decoding of LFP activity from motor cortex has consequently been receiving more attention from the BMI community as quadriplegic participants in the BrainGate trials have had their MEA implants in for several years.

Currently, the major barriers to microelectrode array use in humans are regulatory. BlackRock manufactures the only MEA which is permitted for human

implantation, and only under an Investigational Device Exemption (IDE) from the FDA. The lack of more FDA-approved MEAs is an unfortunate byproduct of the small size of the cortical BMI market and their inability to serve the clinical needs of the larger epileptic seizure mapping market. Pre-surgical mapping for epileptic resection requires implants with much wider coverage, as the existing clinical tools for noninvasive seizure localization are extremely inaccurate. Seizure semiology and noninvasive pre-surgical seizure mapping with EEG recordings can be extremely imprecise—it is not uncommon to be unsure which hemisphere a patient’s seizures originate from—such that implants must often span lobes rather than millimeters. Although seizure mapping is not a focus of this thesis, it is worth highlighting as an example where ECoG recordings do not merely occupy an arbitrary “mesoscopic” niche, but rather uniquely enable the spatiotemporal characterization of wide-scale cortical networks.

5.3.2 Functional Magnetic Resonance Imaging

Where microelectrode recordings enable the recording of single neurons with high temporal resolution, fMRI is currently the gold standard for whole-brain recordings. Since fMRI is noninvasive and can be used to record from high numbers of healthy human subjects, it is ideal for localizing neural activity for novel tasks or behavioral variables to a given brain region or network. Although poor temporal resolution makes it difficult to decompose dynamic neural recruitment during complex natural tasks, behaviors can be isolated using block-based experimental

designs or experimental manipulations which carefully vary one attribute of a behavior over two more tasks.

Much of the body of literature on fMRI correlates with behavior has been performed at 1.5T or 3T, with effective resolutions on the order of 8-125 mm³. Relative to ECoG recordings, fMRI studies traditionally suffer from low signal-to-noise ratio (SNR)—requiring aggregation of results from multiple subjects—and low temporal resolution. The prevalence of higher field strength fMRI studies, recorded at 7T, has been increasing recently and provides higher spatial resolution (on the order of 1-2 mm³) and a sufficiently robust signal to map the functional anatomy of single subjects (Martuzzi et al., 2014; Siero et al., 2014). It is important to note that fMRI measures blood oxygenation rather than neural activity. In general, the correlation between neural activity and the fMRI BOLD signal (i.e., “neurovascular coupling”) is robust. The coupling between neural activity and fMRI BOLD is not strictly linear (Ances et al., 2000; Devor et al., 2003), and the strength of coupling can severely break down in disease conditions like hypertension, diabetes, and Alzheimer’s or in the presence of vasoactive drugs or chronic stimulation (Pasley and Freeman, 2008).

While fMRI is a powerful tool for neuroscience researchers, there are a number of structural issues that make fMRI difficult for use in seizure mapping and brain-machine interface. Most obviously, the bulk and cost of fMRI machines make them an impossible technology to deploy for everyday brain-machine interface use. In the case of functional mapping, the noninvasive nature of fMRI makes it a nontrivial to apply study findings to surgical plans. Even if a sufficiently high-

resolution fMRI study is available, the cortical areas with relevant BOLD increases must be co-registered to the surgical entry point. A functional map generated from fMRI (or any noninvasive technique) is only as useful to a surgeon as his or her ability to contextualize the findings within visible landmarks or neuronavigation displays. In cases where functional cortex neighbors or is commingled with epileptogenic tissue, ECoG maps have the advantage of being trivially co-registered to the surgical landmarks: electrodes are in contact with the cortex at the start of the resection procedure. Most importantly, fMRI is not a feasible candidate for mapping seizures. fMRI is extremely sensitive to movement artifact and its low temporal resolution would blur the distinction between the focus and secondary seizure zones. Furthermore, it simply would not be feasible for patients to be scanned for long enough for their seizures to be mapped. While these limitations apply to seizure mapping rather than functional mapping, the inpatient mapping period performed by ECoG provides ample opportunity for functional mapping between ictal events.

5.3.3 Electroencephalography

Since electroencephalography (EEG) provides electrophysiological measurements of cortical activity noninvasively, it has been widely used for both functional mapping and brain-machine interface. EEG has good temporal resolution but extremely poor spatial resolution due to volume conduction. This poor spatial resolution makes it a poor modality for functional mapping applications. EEG is useful for determining the dynamics of recruitment of large brain areas during time-

varying naturalistic tasks, but alternative modalities (e.g., fMRI) are much better candidates for drawing the boundaries of those brain areas.

Relative to ECoG, EEG has low signal-to-noise ratio and low bandwidth that limits the ability of EEG to record activity in the high gamma (>70 Hz) range. Some recent studies have reported high gamma responses in EEG (Ball et al., 2008; Darvas et al., 2010) with atypical recording procedures, though these findings are not always significant in single subjects (Ball et al., 2008). This low signal quality in the high gamma band is in stark contrast to the measurements obtained for this thesis and throughout the large body of ECoG literature, where high gamma increases are widely observed to be significant and robust in single channels (and single trials) in single subjects. EEG recordings are also extremely sensitive to facial muscle and ocular movement artifacts. Offline studies must either use source localization (e.g., ICA, inverse modeling) to isolate and remove these sources of noise or diligently remove trials with clear contamination from non-neural sources. For online EEG systems, linear source localization techniques which require trivial real-time processing or algorithmic bad trial removal would be required and present an additional challenge to implementation relative to invasive modalities.

Despite its limitations, EEG has been used widely for BMI applications. Single trial estimates of event-related synchronization (ERS) and desynchronization (ERD) in alpha and beta frequencies have been used to control computer cursors in one, two, and three dimensions (McFarland et al., 2010; Wolpaw et al., 1991; Wolpaw and McFarland, 2004). Slow cortical potentials (SCPs), or the negativity/positivity of EEG signals can also be used to control computer cursors (Birbaumer et al., 1999).

These studies usually require users to train for tens to hundreds of hours until their neural signals robustly correlate with their attempted cursor movements. While these studies serve as demonstrations of the information content of the EEG signal, noisy control of 1-3 continuous degrees of freedom is seldom sufficient to reliably complete a task. As such, other modalities of the EEG signal are more common sources of BMI control signals.

In particular, evoked potentials have been adapted in clever ways to provide users with a choice between multiple options on a computer screen. For example, P300 Spellers strobe a grid of letters randomly and select the letter whose strobe timings over multiple trials correlate best with the timing of evoked EEG activity (Farwell and Donchin, 1988; Krusienski et al., 2008). Other studies have strobed several choices on a screen at distinct frequencies, and used the dominant frequency of the steady-state visually evoked potential (SSVEP) in occipital EEG electrodes to determine which choice the user is attending to (Cheng et al., 2002; Guger et al., 2012; Kuś et al., 2013). These systems can be extremely robust and achieve high information transfer rates (especially relative to EEG systems using ERD/ERS), but they require the user to saccade to the target (Brunner et al., 2010), so it is unclear long-term if they will provide any increased performance over high-fidelity eye-tracking. Eye-tracking in particular is undergoing a renaissance associated with the increased prevalence of augmented reality and virtual reality systems.

5.4 Functional Mapping via ECoG Recordings vs. Electrocortical Stimulation Mapping

The biggest barrier to adoption of passive ECoG mapping of brain function for epilepsy surgery planning is not another neural *recording* modality, but rather mapping via *stimulation* of ECoG electrodes. Electrocortical stimulation mapping (ESM) has been employed for over a century, and has been used to provide fundamental insights into the organization of human cortex (Penfield and Boldrey, 1937; others?). This long history has led to an entrenchment of the technique—the availability of FDA-approved commercial electrical stimulators is extremely high relative to mapping systems. Furthermore, ESM often requires less conscious participation by the subject; this is especially true for mapping motor function, as the patient need not be awake for movements to be elicited via stimulation.

Stimulation mapping also benefits from a relative intuitiveness when compared to the signal processing and statistical testing required to passively characterize the functional recruitment of ECoG sites. If the electrical current through a pair of electrodes is high enough and the stimulation site is involved in task processing, behavior can be elicited or interrupted. There is effectively only one parameter to tune at a pair of sites (i.e., the current) and the results of stimulation can be easily scored—either stimulation did or did not affect the behavior of interest. This ease of interpretation makes ESM a strongly favored technique among neurosurgeons and neurologists who have to make difficult and irreversible decisions about which brain regions to spare (risking seizure recurrence) or resect (risking functional deficits) during epilepsy surgery.

Despite its advantages, stimulation mapping is riddled with implementational difficulties ranging from patient safety issues to the fact that it

simply takes too long. ESM can cause pain, afterdischarges, or full-blown seizures, all of which are uncomfortable or dangerous to the patient. The risk of stimulating seizures in particular is problematic since these seizures exhaust and endanger the patient without providing any diagnostic information about the target seizure focus. A more practical consideration is that the tuning of the current passed through each electrode pair (which must be done for each electrode pair and task separately) is extremely time-consuming, and doomed to get worse with the increasing resolution of ECoG grids. Additionally, in higher resolution grids, it is still unclear what effect the higher current density over smaller cortical surface areas will have on ESM findings.

Beyond the aforementioned difficulties of ESM is the central question of whether stimulation mapping is truly measuring local cortical function. For example, does interrupting speech at one pair of sites imply that the pair itself is involved in language production? Or rather, might it imply that the current propagated to one or more sites involved in language production? There is a growing body of evidence that stimulation mapping and passive ECoG mapping often disagree (Bauer et al., 2013; Cervenka et al., 2013, 2011; Ruescher et al., 2013), particularly for functional mapping of language, which likely implies that stimulation is not acting as locally as is generally assumed.

Even though many clinicians agree that passive ECoG mapping should be investigated as an alternative to ESM, it has been and remains very difficult to challenge ESM as the gold standard for functional mapping. In addition to the entrenched status of stimulation mapping and general discomfort with changes in

the clinical standard of care, a trusted third technique is lacking for objective comparisons of stimulation and ECoG mapping. Substantial evidence exists that ECoG (particularly in high gamma frequencies) is well correlated with functional measures of neural activity obtained from fMRI and microelectrode arrays, but few studies have compared the relative correspondence of both ECoG and stimulation with these techniques. In the absence of such an independent assessment, ECoG mapping results are often compared to ESM by simply assuming ESM is the gold standard (Bauer et al., 2013; Brunner et al., 2009; Cheung and Chang, 2012; Ruescher et al., 2013; Wu et al., 2010). It would obviously be impossible to query the relative accuracy of the two techniques (i.e., and thus ever potentially prove the superiority of ECoG mapping) with this assumption intact.

Our team has begun an admittedly coarse approach to finding an independent identification of functional cortex via identification of regions of interest (ROIs), which conservatively demarcate functional anatomy. Using this technique, we were able to make a preliminary case that ECoG functional mapping outperforms stimulation mapping. Ultimately, however, ECoG will need to show superior performance in predicting post-operative deficits to truly replace ESM. In addition to being an independent standard, predicting post-operative deficits is the ultimate goal of epilepsy surgery planning.

The use of post-operative deficits as a gold standard is certainly not without its own challenges. Aggregating databases of post-operative deficits and their relationships with functional mapping results is difficult since putative eloquent cortex as identified is preferentially spared. This means that there would be an

underrepresentation of ESM-positive sites in such a database. The net effect of such a sampling bias would be an overestimation of ECoG's relative sensitivity and an overestimation of ESM's relative specificity (see Table 5.1). This could, of course, be overcome by simply including enough patients in the database that these factors could be balanced appropriately. Beyond the issue of sampling bias is the complication that deficits are not truly binary: they may be incomplete or vary in duration (e.g., deficits may be chronic or resolve several months after surgery). Segmenting the database into sub-categories provides opportunities to highlight a role for ECoG mapping but further increases the size requirements of the cohort.

Deficit?	Truth	ESM	ECoG	Information Gained
Yes	+	+	+	None
Yes	+	+	-	ECoG Sensitivity Decrease
Yes	+	-	+	ESM Sensitivity Decrease
Yes	+	-	-	None
Yes	-	+	+	None
Yes	-	+	-	ESM Sensitivity Increase (incorrect)
Yes	-	-	+	ECoG Sensitivity Increase (incorrect)
Yes	-	-	-	None
No	-	+	+	None
No	-	+	-	ESM Specificity Decrease
No	-	-	+	ECoG Specificity Decrease
No	-	-	-	None

Table 5.1. Information gained from resections, ESM, and ECoG results for resected sites. Grayed out rows are ESM-positive and would thus be underrepresented in a database of resected sites. Each row corresponds to a specific set of attributes of a single resected site: (1) Did the resection cause a deficit in the task of interest?, (2) Is this site truly functionally related to the task of interest?, (3) Did ESM identify this site as task-related?, and (4) Did ECoG identify this site as task-related? The last column highlights information gained (sometimes incorrectly) about a site with the specified set of attributes. Note: this table assumes that a lesion could result from the resection of another site, which is why the first and second columns are different.

5.5 The Near Future of ECoG for Functional Mapping and Brain-Machine Interface

5.5.1 Extensions of this Thesis

The online functional mapping system detailed in Chapter 2 is an extremely powerful tool with the potential to replace ESM or serve as a complementary technique for functional mapping associated with epilepsy surgery planning. As detailed in section 5.4, any long-term efforts to justify the use of ECoG passive mapping will require evidence from studies of post-operative deficit studies. Another key factor will be to make the use of our team's system as easy as possible. Several simple usability additions would be extremely helpful, including the addition of online trial-averaging with respect to response times; this is currently functional but rarely used for motor mapping, though not implemented for speech mapping. Adding the ability to generate stimulus- or response-specific maps online would also be extremely useful, such that cortical representations of finger stimulations, finger movements, phonemes, etc. could be simultaneously displayed. Especially in patients whose functional anatomy may be displaced or convoluted by pathological epileptogenic networks, patient-specific functional landmarks like the location of postcentral digit representations or phonetic representations in Wernicke's area may help inform placement of grids intraoperatively. Another important challenge will be finding a compelling way to *intraoperatively* visualize task-related activations on the brain. Functional mapping in inpatient settings can

be performed with the benefit of assuming static grid placement localized by post-operative CT. Intraoperative functional maps will often need to be generated for temporary grid placements, and will likely even spur grid movement. In these conditions, the software will likely need to facilitate quick import of an intraoperative brain photo or interface with neuronavigation software to acquire an anatomical scan as a template for displaying activity. Finally, the long-term adoption of our system will require the software to become easier to distribute and, ideally, extensible to multiple different types of recording hardware. To solve these issues, it would be useful to either adapt our software to a framework like BCI2000 or grow our own community of user-developers via GitHub or a similar code-sharing site.

Chapter 3 describes our lab's efforts to control reaching and grasping simultaneously in two patients with epilepsy. There are many ways to extend this effort, several of which our team has begun already. The most straightforward improvements to our BMI control scheme involve enriching the complexity of reach and/or grasp control by the user. Our team has recently demonstrated online control of individual finger movements using an hdECoG array (Hotson et al., 2015). If this degree of control could be combined with multi-axial reach decoding (Anderson et al., 2012; Pistohl et al., 2008), it would be an impressive piece of evidence supporting the viability of ECoG-based neuroprosthetics. Additionally, as mentioned above, our team has recently designed and tested a framework called HARMONIE for integrating ECoG as a source of high-level control signals in cooperation with machine intelligence and non-neural control signals (e.g., eye

tracking) [(Katyal et al., 2013; McMullen et al., 2014)]. While initial efforts involved simply using ECoG signals to trigger complex autonomous movements, HARMONIE could surely integrate independent reaching and grasping control signals to provide additional low-level control to the user. For example, context menus could be used to choose between grasp configurations via decoded grasp aperture and/or between manipulation types via decoded reach extent. Improvements in low-level direct neural control via ECoG could also allow HARMONIE to release low-level control to the user if the preprogrammed library of movement types was insufficient for a given task. Ultimately, all of these strategies need to be tested and validated with quadriplegic patients. Steps toward implementation of an ECoG-based BMI in paralyzed populations will be discussed more fully below.

Finally, Chapter 4 details a preliminary study of using hdECoG to map digit representations in the postcentral gyrus. Interesting next topics to be investigated include: (1) how finger stimulations affect the phase of low frequency oscillations in postcentral gyrus, (2) how high gamma activity represents different intensities of stimulation, (3) how high gamma activity represents different dynamic patterns of vibration, (4) how representations of activity from multiple fingers interact during multi-finger vibration, and (5) how the degree of somatotopy detected in pre- and post-central gyri for motor and sensory finger representations, respectively, compare in hdECoG recordings. Beyond these basic questions about the representation of fingertip vibration at hdECoG scale is a question of central importance to BMI—can knowledge of these representations be used to provide sensory feedback via cortical stimulation? Somatosensory percepts can be elicited

via ECoG-scale stimulation (Johnson et al., 2013; Penfield and Boldrey, 1937), but it is unclear if they could ever be perceived as natural stimuli rather than paresthesias. The initial answers to this question will likely come from clinical ESM sessions with hdECoG or micro-ECoG implants placed over postcentral gyrus, and hopefully expanded upon if additional research stimulation sessions can be performed.

5.5.2 Next Steps for Clinical ECoG-Based BMIs

A huge goal of the ECoG-based BMI field is to begin to test whether ECoG is a viable alternative to MEAs for BMI control by quadriplegics. The barriers to starting this work at any one center are immense (e.g., cost, regulatory approvals, personnel effort, etc.), but there are additional barriers to be overcome by the field at large. The first barrier is regulatory approval of ECoG implantation for long-term BMI use. One study in the United States to date (Wang et al., 2013) has successfully demonstrated the efficacy of a short-term (i.e., 30-day) ECoG implant enabling neuroprosthetic control by a quadriplegic individual. Progressing from short- to long-term implantations is not trivial, however. ECoG implants are designed for inpatient seizure mapping where there is usually no need to record for longer than 2-3 weeks. Some companies (e.g., NeuroPace and NeuroVista) have developed fully implantable ECoG systems with lower channel counts than would be ideal for BMI use (Davis et al., 2011; Sun et al., 2008). Fully implantable systems pose much lower infection risk, however, than trans-cutaneous ECoG implants, and thus are not suitable regulatory predicates. Some of this risk could be mitigated via wireless ECoG implants which telemeter recorded signals across the scalp. Several

companies, including Ripple (Guillory et al., 2011) and Clnatec (Charvet et al., 2011), are developing wireless ECoG systems, though none is currently approved for human implantation in the United States. While wireless implants (of both ECoG arrays and MEAs) would be hugely beneficial to the quadriplegic BMI field, the market size is so small that it may be difficult for companies to justify the costs of pursuing regulatory approval. A more likely avenue is that a company will pursue FDA approval of a wireless ECoG system for long-term seizure monitoring. Such a company would be an ideal candidate to work with BMI researchers to extend the FDA-approved indication of the device to neuroprosthetic control. These industry-university partnerships are increasingly being encouraged by funding agencies, including the most recent round of NIH BRAIN Initiative Funding Opportunity Announcements. This is an acknowledgment of the relative regulatory and manufacturing expertise (and resources) concentrated in industry that have generally been under-utilized by university researchers.

If ECoG implants can achieve regulatory approval for long-term implantation, the obvious question is whether they can outperform MEAs for neuroprosthetic control or become a better candidate for long-term implantation than MEAs. ECoG implants have larger recording surfaces and do not penetrate the cortex, and so may be more resilient to degradation via biological processes over long-term implantations. To my knowledge, University of Pittsburgh has performed the only published voluntary implantation of an ECoG grid for BMI control (Wang et al., 2013). While this was an important first step for the field, this study did not achieve control that compared favorably with that from microelectrodes at the same center

(Collinger et al., 2013). This discrepancy is possibly due to the differences in recording modality, but it is worth noting the marked discrepancies in study duration (30 days vs. 13 weeks) and that the ECoG array was (presumably) mistakenly implanted over postcentral gyrus.

In my opinion, the pieces are in place for another center to markedly improve upon the preliminary ECoG BMI demonstrated by the University of Pittsburgh. An hdECoG array with 3 mm spacing centered on the hand knob of the precentral gyrus would likely provide the resolution necessary to differentiate finger representations (as in Chapter 4, but targeting motor cortex) for individual finger actuation simultaneous to reach control (as in Chapter 3). Intraoperative functional mapping of attempted movements during an awake craniotomy would be the best way to ensure that the ECoG implant(s) end up in the desired location. Wireless technology does not seem strictly necessary for long-term implantations, given the success of the BrainGate and Revolutionizing Prosthetics trials. Nevertheless, large multi-patient multi-site clinical studies are likely to highlight a dramatic reduction in surgical infection risk by eliminating the transcutaneous connector from the brain-machine interface.

It is still unclear what the optimal resolution is for sampling sensorimotor representations in the cortex. While MEAs provide sub-millimeter precision, redundantly sampling cortical representations unnecessarily sacrifices coverage area. Only time will tell what electrode spacing will provide the most efficient coverage of cortical areas containing the BMI control signals of the future. Nevertheless, the unfortunate truth for ECoG is that MEAs continue to set an

impressive standard for neuroprosthetic control, and that BMI control with MEAs has a decades-long head start over similar efforts with ECoG. This timing disadvantage, though, is also a reason for hope. ECoG BMI research is progressing at an extremely rapid pace, and should not necessarily be judged in its current state against current achievements by the MEA neuroprosthetics community.

Bibliography

Acharya, S., Fifer, M.S., Benz, H.L., Crone, N.E., Thakor, N.V., 2010.

Electrocorticographic amplitude predicts finger positions during slow grasping motions of the hand. *J. Neural Eng.* 7, 046002. doi:10.1088/1741-2560/7/4/046002

Aflalo, T., Kellis, S., Klaes, C., Lee, B., Shi, Y., Pejsa, K., Shanfield, K., Hayes-Jackson, S.,

Aisen, M., Heck, C., Liu, C., Andersen, R.A., 2015. Decoding motor imagery from the posterior parietal cortex of a tetraplegic human. *Science* 348, 906–910. doi:10.1126/science.aaa5417

Aggarwal, V., Acharya, S., Tenore, F., Shin, H.-C., Etienne-Cummings, R., Schieber,

M.H., Thakor, N.V., 2008. Asynchronous Decoding of Dexterous Finger Movements Using M1 Neurons. *IEEE Trans. Neural Syst. Rehabil. Eng.* 16, 3–14. doi:10.1109/TNSRE.2007.916289

Ances, B.M., Zarahn, E., Greenberg, J.H., Detre, J.A., 2000. Coupling of neural

activation to blood flow in the somatosensory cortex of rats is time-intensity separable, but not linear. *J. Cereb. Blood Flow Metab. Off. J. Int. Soc. Cereb.*

Blood Flow Metab. 20, 921–930. doi:10.1097/00004647-200006000-00004

Andersen, R.A., Musallam, S., Pesaran, B., 2004. Selecting the signals for a brain–

machine interface. *Curr. Opin. Neurobiol.* 14, 720–726.

doi:10.1016/j.conb.2004.10.005

- Anderson, N.R., Blakely, T., Schalk, G., Leuthardt, E.C., Moran, D.W., 2012. Electrographic (ECoG) correlates of human arm movements. *Exp. Brain Res.* 223, 1–10. doi:10.1007/s00221-012-3226-1
- Ball, T., Demandt, E., Mutschler, I., Neitzel, E., Mehring, C., Vogt, K., Aertsen, A., Schulze-Bonhage, A., 2008. Movement related activity in the high gamma range of the human EEG. *Neuroimage* 41, 302–10. doi:10.1016/j.neuroimage.2008.02.032
- Ball, T., Kern, M., Mutschler, I., Aertsen, A., Schulze-Bonhage, A., 2009. Signal quality of simultaneously recorded invasive and non-invasive EEG. *Neuroimage* 46, 708–16. doi:10.1016/j.neuroimage.2009.02.028
- Ball, T., Schulze-Bonhage, A., Aertsen, A., Mehring, C., 2009. Differential representation of arm movement direction in relation to cortical anatomy and function. *J. Neural Eng.* 6, 016006. doi:10.1088/1741-2560/6/1/016006
- Bansal, A.K., Vargas-Irwin, C.E., Truccolo, W., Donoghue, J.P., 2011. Relationships among low-frequency local field potentials, spiking activity, and three-dimensional reach and grasp kinematics in primary motor and ventral premotor cortices. *J. Neurophysiol.* 105, 1603–1619. doi:10.1152/jn.00532.2010
- Barrese, J.C., Rao, N., Paroo, K., Triebwasser, C., Vargas-Irwin, C., Franquemont, L., Donoghue, J.P., 2013. Failure mode analysis of silicon-based intracortical microelectrode arrays in non-human primates. *J. Neural Eng.* 10, 066014. doi:10.1088/1741-2560/10/6/066014

- Bauer, P.R., Vansteensel, M.J., Bleichner, M.G., Hermes, D., Ferrier, C.H., Aarnoutse, E.J., Ramsey, N.F., 2013. Mismatch between electrocortical stimulation and electrocorticography frequency mapping of language. *Brain Stimul* 6, 524–31. doi:10.1016/j.brs.2013.01.001
- Baumgartner, C., Doppelbauer, A., Deecke, L., Barth, D., Zeitlhofer, J., Lindinger, G., Sutherling, W., 1991. Neuromagnetic investigation of somatotopy of human hand somatosensory cortex. *Exp. Brain Res.* 8, 641–648.
- Beisteiner, R., Höllinger, P., Lindinger, G., Lang, W., Berthoz, A., 1995. Mental representations of movements. Brain potentials associated with imagination of hand movements. *Electroencephalogr. Clin. Neurophysiol.* 96, 183–193.
- Benjamini, Y., Hochberg, Y., 1995. Controlling the False Discovery Rate: A Practical and Powerful Approach to Multiple Testing. *J. R. Stat. Soc. Ser. B Methodol.* 57, 289–300.
- Berger, T.W., Hampson, R.E., Song, D., Goonawardena, A., Marmarelis, V.Z., Deadwyler, S.A., 2011. A cortical neural prosthesis for restoring and enhancing memory. *J. Neural Eng.* 8, 046017. doi:10.1088/1741-2560/8/4/046017
- Birbaumer, N., Ghanayim, N., Hinterberger, T., Iversen, I., Kotchoubey, B., Kübler, A., Perelmouter, J., Taub, E., Flor, H., 1999. A spelling device for the paralysed. *Nature* 398, 297–298. doi:10.1038/18581
- Blume, W.T., Jones, D.C., Pathak, P., 2004. Properties of after-discharges from cortical electrical stimulation in focal epilepsies. *Clin. Neurophysiol. Off. J. Int. Fed. Clin. Neurophysiol.* 115, 982–989. doi:10.1016/j.clinph.2003.11.023

- Boatman, D., Hall, C., Goldstein, M.H., Lesser, R., Gordon, B., 1997. Neuroperceptual differences in consonant and vowel discrimination: as revealed by direct cortical electrical interference. *Cortex* 33, 83–98.
- Bokil, H., Andrews, P., Kulkarni, J.E., Mehta, S., Mitra, P.P., 2010. Chronux: A platform for analyzing neural signals. *J. Neurosci. Methods* 192, 146–151.
doi:10.1016/j.jneumeth.2010.06.020
- Bouchard, K.E., Chang, E.F., 2014. Neural decoding of spoken vowels from human sensory-motor cortex with high-density electrocorticography. *Conf. Proc. Annu. Int. Conf. IEEE Eng. Med. Biol. Soc. IEEE Eng. Med. Biol. Soc. Annu. Conf. 2014*, 6782–6785. doi:10.1109/EMBC.2014.6945185
- Bradberry, T.J., Gentili, R.J., Contreras-Vidal, J.L., 2010. Reconstructing Three-Dimensional Hand Movements from Noninvasive Electroencephalographic Signals. *J. Neurosci.* 30, 3432–3437. doi:10.1523/JNEUROSCI.6107-09.2010
- Bridges, M.M., Para, M.P., Mashner, M.J., 2011. Control System Architecture for the Modular Prosthetic Limb. *Johns Hopkins APL Tech. Dig.* 30, 217–222.
- Brunner, P., Joshi, S., Briskin, S., Wolpaw, J.R., Bischof, H., Schalk, G., 2010. Does the “P300” speller depend on eye gaze? *J. Neural Eng.* 7, 056013.
doi:10.1088/1741-2560/7/5/056013
- Brunner, P., Ritaccio, A.L., Lynch, T.M., Emrich, J.F., Wilson, J.A., Williams, J.C., Aarnoutse, E.J., Ramsey, N.F., Leuthardt, E.C., Bischof, H., Schalk, G., 2009. A practical procedure for real-time functional mapping of eloquent cortex using electrocorticographic signals in humans. *Epilepsy Behav* 15, 278–86.
doi:10.1016/j.yebeh.2009.04.001

- Bruns, A., 2004. Fourier-, Hilbert- and wavelet-based signal analysis: are they really different approaches? *J. Neurosci. Methods* 137, 321–332.
doi:10.1016/j.jneumeth.2004.03.002
- Buchsbaum, B.R., Hickok, G., Humphries, C., 2001. Role of left posterior superior temporal gyrus in phonological processing for speech perception and production. *Cogn. Sci.* 25, 663–678.
- Canolty, R.T., Edwards, E., Dalal, S.S., Soltani, M., Nagarajan, S.S., Kirsch, H.E., Berger, M.S., Barbaro, N.M., Knight, R.T., 2006. High gamma power is phase-locked to theta oscillations in human neocortex. *Science* 313, 1626–8.
- Canolty, R.T., Ganguly, K., Carmena, J.M., 2012. Task-Dependent Changes in Cross-Level Coupling between Single Neurons and Oscillatory Activity in Multiscale Networks. *PLoS Comput Biol* 8, e1002809.
doi:10.1371/journal.pcbi.1002809
- Canolty, R.T., Soltani, M., Dalal, S.S., Edwards, E., Dronkers, N.F., Nagarajan, S.S., Kirsch, H.E., Barbaro, N.M., Knight, R.T., 2007. Spatiotemporal dynamics of word processing in the human brain. *Front Neurosci* 1, 185–96.
- Cash, S.S., Hochberg, L.R., 2015. The Emergence of Single Neurons in Clinical Neurology. *Neuron* 86, 79–91. doi:10.1016/j.neuron.2015.03.058
- Cedzich, C., Taniguchi, M., Schafer, S., Schramm, J., 1996. Somatosensory evoked potential phase reversal and direct motor cortex stimulation during surgery in and around the central region. *Neurosurgery* 38, 962–70.
- Cervenka, M.C., Boatman-Reich, D.F., Ward, J., Franaszczuk, P.J., Crone, N.E., 2011. Language mapping in multilingual patients: electrocorticography and cortical

- stimulation during naming. *Front Hum Neurosci* 5, 13.
doi:10.3389/fnhum.2011.00013
- Cervenka, M.C., Corines, J., Boatman-Reich, D.F., Eloyan, A., Sheng, X., Franaszczuk, P.J., Crone, N.E., 2013. Electrocorticographic functional mapping identifies human cortex critical for auditory and visual naming. *Neuroimage* 69, 267–76. doi:10.1016/j.neuroimage.2012.12.037
- Chao, Z.C., Nagasaka, Y., Fujii, N., 2010. Long-Term Asynchronous Decoding of Arm Motion Using Electrocorticographic Signals in Monkeys. *Front. Neuroengineering* 3. doi:10.3389/fneng.2010.00003
- Chapin, J.K., Moxon, K.A., Markowitz, R.S., Nicolelis, M.A., 1999. Real-time control of a robot arm using simultaneously recorded neurons in the motor cortex. *Nat. Neurosci.* 2, 664–670. doi:10.1038/10223
- Charvet, G., Foerster, M., Filipe, S., Porcherot, J., Beche, J.F., Guillemaud, R., Audebert, P., Regis, G., Zongo, B., Robinet, S., Condemine, C., Tetu, Y., Sauter, F., Mestais, C., Benabid, A.L., 2011. WIMAGINE: A wireless, low power, 64-channel ECoG recording platform for implantable BCI applications, in: 2011 5th International IEEE/EMBS Conference on Neural Engineering (NER). Presented at the 2011 5th International IEEE/EMBS Conference on Neural Engineering (NER), pp. 356–359. doi:10.1109/NER.2011.5910560
- Cheng, M., Gao, X., Gao, S., Xu, D., 2002. Design and implementation of a brain-computer interface with high transfer rates. *IEEE Trans. Biomed. Eng.* 49, 1181–1186. doi:10.1109/TBME.2002.803536

- Chestek, C.A., Gilja, V., Blabe, C.H., Foster, B.L., Shenoy, K.V., Parvizi, J., Henderson, J.M., 2013. Hand posture classification using electrocorticography signals in the gamma band over human sensorimotor brain areas. *J. Neural Eng.* 10, 026002. doi:10.1088/1741-2560/10/2/026002
- Cheung, C., Chang, E.F., 2012. Real-time, time-frequency mapping of event-related cortical activation. *J. Neural Eng.* 9, 046018. doi:10.1088/1741-2560/9/4/046018
- Chronux [WWW Document], 2015. URL <http://www.chronux.org/> (accessed 8.28.15).
- Collinger, J.L., Wodlinger, B., Downey, J.E., Wang, W., Tyler-Kabara, E.C., Weber, D.J., McMorland, A.J.C., Velliste, M., Boninger, M.L., Schwartz, A.B., 2013. High-performance neuroprosthetic control by an individual with tetraplegia. *Lancet* 381, 557–564. doi:10.1016/S0140-6736(12)61816-9
- Crone, N.E., Boatman, D., Gordon, B., Hao, L., 2001a. Induced electrocorticographic gamma activity during auditory perception. Brazier Award-winning article, 2001. *Clin. Neurophysiol.* 112, 565–82.
- Crone, N.E., Hao, L., Hart, J., Jr., Boatman, D., Lesser, R.P., Irizarry, R., Gordon, B., 2001b. Electrocorticographic gamma activity during word production in spoken and sign language. *Neurology* 57, 2045–53.
- Crone, N.E., Korzeniewska, A., Franaszczuk, P.J., 2011. Cortical gamma responses: searching high and low. *Int J Psychophysiol* 79, 9–15. doi:10.1016/j.ijpsycho.2010.10.013

- Crone, N.E., Miglioretti, D.L., Gordon, B., Lesser, R.P., 1998. Functional mapping of human sensorimotor cortex with electrocorticographic spectral analysis. II. Event-related synchronization in the gamma band. *Brain* 121, 2301–15.
- Crone, N.E., Sinai, A.S., Korzeniewska, A., 2006. High-frequency gamma oscillations and human brain mapping with electrocorticography. *Prog Brain Res* 159, 279–302.
- Cunningham, J.P., Nuyujukian, P., Gilja, V., Chestek, C.A., Ryu, S.I., Shenoy, K.V., 2011. A closed-loop human simulator for investigating the role of feedback control in brain-machine interfaces. *J. Neurophysiol.* 105, 1932–1949.
doi:10.1152/jn.00503.2010
- Cushing, H., 1908. A NOTE UPON THE FARADIC STIMULATION OF THE POSTCENTRAL GYRUS IN CONSCIOUS PATIENTS.
- Damasio, A.R., Geschwind, N., 1984. The neural basis of language. *Annu Rev Neurosci* 7, 127–47.
- Damasio, H., 1991. Neuroanatomical correlates of the aphasias. *Acquir. Aphasia* 2, 45–71.
- Darvas, F., Scherer, R., Ojemann, J.G., Rao, R.P., Miller, K.J., Sorensen, L.B., 2010. High gamma mapping using EEG. *Neuroimage* 49, 930–8.
- Datta, A.N., Oser, N., Bauder, F., Maier, O., Martin, F., Ramelli, G.P., Steinlin, M., Weber, P., Penner, I.-K., 2013. Cognitive impairment and cortical reorganization in children with benign epilepsy with centrotemporal spikes. *Epilepsia* 54, 487–494. doi:10.1111/epi.12067

- Davis, A.E., Wada, J.A., 1978. Speech dominance and handedness in the normal human. *Brain Lang.* 5, 42–55.
- Davis, K.A., Sturges, B.K., Vite, C.H., Ruedebusch, V., Worrell, G., Gardner, A.B., Leyde, K., Sheffield, W.D., Litt, B., 2011. A novel implanted device to wirelessly record and analyze continuous intracranial canine EEG. *Epilepsy Res.* 96, 116–122. doi:10.1016/j.eplepsyres.2011.05.011
- Davoodi, R., Urata, C., Todorov, E., Loeb, G.E., 2004. Development of clinician-friendly software for musculoskeletal modeling and control. *Conf. Proc. Annu. Int. Conf. IEEE Eng. Med. Biol. Soc. IEEE Eng. Med. Biol. Soc. Annu. Conf.* 6, 4622–4625. doi:10.1109/IEMBS.2004.1404281
- Devor, A., Dunn, A.K., Andermann, M.L., Ulbert, I., Boas, D.A., Dale, A.M., 2003. Coupling of total hemoglobin concentration, oxygenation, and neural activity in rat somatosensory cortex. *Neuron* 39, 353–359.
- DiCarlo, J.J., Johnson, K.O., 1999. Velocity Invariance of Receptive Field Structure in Somatosensory Cortical Area 3b of the Alert Monkey. *J. Neurosci.* 19, 401–419.
- Dillingham, T.R., Pezzin, L.E., MacKenzie, E.J., 2002. Limb amputation and limb deficiency: epidemiology and recent trends in the United States. *South. Med. J.* 95, 875–883.
- Duncan, J.S., Papademetris, X., Yang, J., Jackowski, M., Zeng, X., Staib, L.H., 2004. Geometric strategies for neuroanatomic analysis from MRI. *NeuroImage* 23 Suppl 1, S34–45. doi:10.1016/j.neuroimage.2004.07.027

- Edwards, E., Nagarajan, S.S., Dalal, S.S., Canolty, R.T., Kirsch, H.E., Barbaro, N.M., Knight, R.T., 2010. Spatiotemporal imaging of cortical activation during verb generation and picture naming. *Neuroimage* 50, 291–301.
- Eliades, S.J., Crone, N.E., Anderson, W.S., Ramadoss, D., Lenz, F.A., Boatman-Reich, D., 2014. Adaptation of High-Gamma Responses in Human Auditory Association Cortex. *J. Neurophysiol.* jn.00207.2014. doi:10.1152/jn.00207.2014
- Engell, A.D., McCarthy, G., 2014. Repetition suppression of face-selective evoked and induced EEG recorded from human cortex. *Hum. Brain Mapp.* 35, 4155–4162. doi:10.1002/hbm.22467
- Farwell, L.A., Donchin, E., 1988. Talking off the top of your head: toward a mental prosthesis utilizing event-related brain potentials. *Electroencephalogr. Clin. Neurophysiol.* 70, 510–523.
- Fifer, M.S., Acharya, S., Benz, H.L., Mollazadeh, M., Crone, N.E., Thakor, N.V., 2012. Toward electrocorticographic control of a dexterous upper limb prosthesis: building brain-machine interfaces. *IEEE Pulse* 3, 38–42. doi:10.1109/MPUL.2011.2175636
- Fifer, M.S., Hotson, G., Wester, B., McMullen, D.P., Wang, Y., Johannes, M.S., Katyal, K.D., Helder, J.B., Para, M.P., Vogelstein, R.J., Anderson, W.S., Thakor, N.V., Crone, N.E., 2014. Simultaneous Neural Control of Simple Reaching and Grasping With the Modular Prosthetic Limb Using Intracranial EEG. *IEEE Trans. Neural Syst. Rehabil. Eng.* 22, 695–705. doi:10.1109/TNSRE.2013.2286955

- Fifer, M.S., Mollazadeh, M., Acharya, S., Thakor, N.V., Crone, N.E., 2011. Asynchronous decoding of grasp aperture from human ECoG during a reach-to-grasp task. Conf. Proc. IEEE Eng. Med. Biol. Soc. 2011, 4584–7. doi:10.1109/IEMBS.2011.6091135
- Filimon, F., 2010. Human cortical control of hand movements: parietofrontal networks for reaching, grasping, and pointing. Neurosci. Rev. J. Bringing Neurobiol. Neurol. Psychiatry 16, 388–407. doi:10.1177/1073858410375468
- Flinker, A., Chang, E.F., Barbaro, N.M., Berger, M.S., Knight, R.T., 2010a. Sub-centimeter language organization in the human temporal lobe. Brain Lang. doi:10.1016/j.bandl.2010.09.009
- Flinker, A., Chang, E.F., Kirsch, H.E., Barbaro, N.M., Crone, N.E., Knight, R.T., 2010b. Single-trial speech suppression of auditory cortex activity in humans. J. Neurosci. 30, 16643–50. doi:10.1523/JNEUROSCI.1809-10.2010
- Flint, R.D., Ethier, C., Oby, E.R., Miller, L.E., Slutzky, M.W., 2012a. Local field potentials allow accurate decoding of muscle activity. J. Neurophysiol. 108, 18–24. doi:10.1152/jn.00832.2011
- Flint, R.D., Lindberg, E.W., Jordan, L.R., Miller, L.E., Slutzky, M.W., 2012b. Accurate decoding of reaching movements from field potentials in the absence of spikes. J. Neural Eng. 9, 046006. doi:10.1088/1741-2560/9/4/046006
- Flint, R.D., Wright, Z.A., Scheid, M.R., Slutzky, M.W., 2013. Long term, stable brain machine interface performance using local field potentials and multiunit spikes. J. Neural Eng. 10, 056005. doi:10.1088/1741-2560/10/5/056005

- Franaszczuk, P.J., Jouny, C.C., 2004. Software system for data management and distributed processing of multichannel biomedical signals. Conf. Proc. Annu. Int. Conf. IEEE Eng. Med. Biol. Soc. IEEE Eng. Med. Biol. Soc. Annu. Conf. 2, 983–985. doi:10.1109/IEMBS.2004.1403326
- Fraser, G.W., Chase, S.M., Whitford, A., Schwartz, A.B., 2009. Control of a brain-computer interface without spike sorting. J. Neural Eng. 6, 055004. doi:10.1088/1741-2560/6/5/055004
- Freeman, W.J., Rogers, L.J., Holmes, M.D., Silbergeld, D.L., 2000. Spatial spectral analysis of human electrocorticograms including the alpha and gamma bands. J Neurosci Methods 95, 111–21.
- Fried, I., Wilson, C.L., Maidment, N.T., Engel, J., Behnke, E., Fields, T.A., Macdonald, K.A., Morrow, J.W., Ackerson, L., 1999. Cerebral microdialysis combined with single-neuron and electroencephalographic recording in neurosurgical patients. J. Neurosurg. 91, 697–705. doi:10.3171/jns.1999.91.4.0697
- Fries, P., 2005. A mechanism for cognitive dynamics: neuronal communication through neuronal coherence. Trends Cogn Sci 9, 474–80. doi:10.1016/j.tics.2005.08.011
- Galán, F., Nuttin, M., Lew, E., Ferrez, P.W., Vanacker, G., Philips, J., Millán, J. del R., 2008. A brain-actuated wheelchair: Asynchronous and non-invasive Brain-computer interfaces for continuous control of robots. Clin. Neurophysiol. 119, 2159–2169. doi:10.1016/j.clinph.2008.06.001
- Genetti, M., Tyrand, R., Grouiller, F., Lascano, A.M., Vulliemoz, S., Spinelli, L., Seeck, M., Schaller, K., Michel, C.M., 2014. Comparison of high gamma

- electrocorticography and fMRI with electrocortical stimulation for localization of somatosensory and language cortex. Clin. Neurophysiol. Off. J. Int. Fed. Clin. Neurophysiol. doi:10.1016/j.clinph.2014.04.007
- Geyer, S., Schleicher, A., Zilles, K., 1999. Areas 3a, 3b, and 1 of Human Primary Somatosensory Cortex: 1. Microstructural Organization and Interindividual Variability. NeuroImage 10, 63–83. doi:10.1006/nimg.1999.0440
- Geyer, S., Schormann, T., Mohlberg, H., Zilles, K., 2000. Areas 3a, 3b, and 1 of Human Primary Somatosensory Cortex: 2. Spatial Normalization to Standard Anatomical Space. NeuroImage 11, 684–696. doi:10.1006/nimg.2000.0548
- Gilja, V., Nuyujukian, P., Chestek, C.A., Cunningham, J.P., Yu, B.M., Fan, J.M., Churchland, M.M., Kaufman, M.T., Kao, J.C., Ryu, S.I., Shenoy, K.V., 2012. A high-performance neural prosthesis enabled by control algorithm design. Nat. Neurosci. 15, 1752–1757. doi:10.1038/nn.3265
- Grefkes, C., Geyer, S., Schormann, T., Roland, P., Zilles, K., 2001. Human Somatosensory Area 2: Observer-Independent Cytoarchitectonic Mapping, Interindividual Variability, and Population Map. NeuroImage 14, 617–631. doi:10.1006/nimg.2001.0858
- Grossman, M., Gotman, J., 2001. As time goes by: high temporal and spatial resolution in cognitively related cortical function. Neurology 57, 1947–8.
- Guger, C., Allison, B.Z., Großwindhager, B., Prückl, R., Hintermüller, C., Kapeller, C., Bruckner, M., Krausz, G., Edlinger, G., 2012. How Many People Could Use an SSVEP BCI? Front. Neurosci. 6. doi:10.3389/fnins.2012.00169

- Guillory, K.S., Askin, R.E., Smith, C.F., McDonnall, D., Hiatt, S., Wilder, A.M., 2011. Wireless electrocortigraph (ECoG) recording system, in: 2011 5th International IEEE/EMBS Conference on Neural Engineering (NER). Presented at the 2011 5th International IEEE/EMBS Conference on Neural Engineering (NER), pp. 196–197. doi:10.1109/NER.2011.5910521
- Halgren, E., Baudena, P., Heit, G., Clarke, J.M., Marinkovic, K., Clarke, M., 1994. Spatio-temporal stages in face and word processing. I. Depth-recorded potentials in the human occipital, temporal and parietal lobes [corrected]. *J Physiol Paris* 88, 1–50.
- Hamberger, M.J., 2007. Cortical language mapping in epilepsy: a critical review. *Neuropsychol Rev* 17, 477–89. doi:10.1007/s11065-007-9046-6
- Harris, A., Katyal, K., Para, M., Thomas, J., 2011. Revolutionizing Prosthetics software technology, in: Systems, Man, and Cybernetics (SMC), 2011 IEEE International Conference on. IEEE, pp. 2877–2884.
- Hickok, G., Poeppel, D., 2007. The cortical organization of speech processing. *Nat Rev Neurosci* 8, 393–402. doi:10.1038/nrn2113
- Hlušítk, P., Solodkin, A., Gullapalli, R.P., Noll, D.C., Small, S.L., 2001. Somatotopy in Human Primary Motor and Somatosensory Hand Representations Revisited. *Cereb. Cortex* 11, 312–321. doi:10.1093/cercor/11.4.312
- Hochberg, L.R., Bacher, D., Jarosiewicz, B., Masse, N.Y., Simeral, J.D., Vogel, J., Haddadin, S., Liu, J., Cash, S.S., van der Smagt, P., Donoghue, J.P., 2012. Reach and grasp by people with tetraplegia using a neurally controlled robotic arm. *Nature* 485, 372–375. doi:10.1038/nature11076

- Hochberg, L.R., Serruya, M.D., Friehs, G.M., Mukand, J.A., Saleh, M., Caplan, A.H., Branner, A., Chen, D., Penn, R.D., Donoghue, J.P., 2006. Neuronal ensemble control of prosthetic devices by a human with tetraplegia. *Nature* 442, 164–71.
- Hotson, G., Fifer, M.S., Acharya, S., Benz, H.L., Anderson, W.S., Thakor, N.V., Crone, N.E., 2014. Coarse Electrocorticographic Decoding of Ipsilateral Reach in Patients with Brain Lesions. *PLoS ONE* 9, e115236.
doi:10.1371/journal.pone.0115236
- Hotson, G., McMullen, D., Fifer, M., Johannes, M., Para, M., Armiger, R., Anderson, W., Thakor, N., Wester, B., Crone, N., 2015. Individual Finger Control of the Modular Prosthetic Limb using High-Density Electrocorticography in a Human Subject. *Rev.*
- Iacoboni, M., Woods, R.P., Brass, M., Bekkering, H., Mazziotta, J.C., Rizzolatti, G., 1999. Cortical Mechanisms of Human Imitation. *Science* 286, 2526–2528.
doi:10.1126/science.286.5449.2526
- Ishitobi, M., Nakasato, N., Suzuki, K., Nagamatsu, K., Shamoto, H., Yoshimoto, T., 2000. Remote discharges in the posterior language area during basal temporal stimulation. *Neuroreport* 11, 2997–3000.
- Jacobs, J., Kahana, M.J., 2009. Neural representations of individual stimuli in humans revealed by gamma-band electrocorticographic activity. *J Neurosci* 29, 10203–14.
- Jerbi, K., Ossandon, T., Hamame, C.M., Senova, S., Dalal, S.S., Jung, J., Minotti, L., Bertrand, O., Berthoz, A., Kahane, P., Lachaux, J.P., 2009. Task-related gamma-

band dynamics from an intracerebral perspective: review and implications for surface EEG and MEG. *Hum Brain Mapp* 30, 1758–71.

doi:10.1002/hbm.20750

Johannes, M.S., Bigelow, J.D., Burck, J.M., Harshbarger, S.D., Kozlowski, M.V., Van Doren, T., 2011. An overview of the developmental process for the modular prosthetic limb. *Johns Hopkins APL Tech. Dig.* 30, 207–216.

Johnson, L.A., Wander, J.D., Sarma, D., Su, D.K., Fetz, E.E., Ojemann, J.G., 2013. Direct electrical stimulation of the somatosensory cortex in humans using electrocorticography electrodes: a qualitative and quantitative report. *J. Neural Eng.* 10, 036021. doi:10.1088/1741-2560/10/3/036021

Kaas, J.H., Nelson, R.J., Sur, M., Lin, C.S., Merzenich, M.M., 1979. Multiple representations of the body within the primary somatosensory cortex of primates. *Science* 204, 521–523. doi:10.1126/science.107591

Karakis, I., Leeman-Markowski, B.A., Leveroni, C.L., Kilbride, R.D., Cash, S.S., Eskandar, E.N., Simon, M.V., 2015. Intra-stimulation discharges: An overlooked cortical electrographic entity triggered by direct electrical stimulation. *Clin. Neurophysiol.* 126, 882–888. doi:10.1016/j.clinph.2014.08.011

Katyal, K.D., Johannes, M.S., McGee, T.G., Harris, A.J., Armiger, R.S., Firpi, A.H., McMullen, D., Hotson, G., Fifer, M.S., Crone, N.E., Vogelstein, R.J., Wester, B.A., 2013. HARMONIE: A multimodal control framework for human assistive robotics, in: 2013 6th International IEEE/EMBS Conference on Neural Engineering (NER). Presented at the 2013 6th International IEEE/EMBS

- Conference on Neural Engineering (NER), pp. 1274–1278.
doi:10.1109/NER.2013.6696173
- Keller, C.J., Truccolo, W., Gale, J.T., Eskandar, E., Thesen, T., Carlson, C., Devinsky, O., Kuzniecky, R., Doyle, W.K., Madsen, J.R., Schomer, D.L., Mehta, A.D., Brown, E.N., Hochberg, L.R., Ulbert, I., Halgren, E., Cash, S.S., 2010. Heterogeneous neuronal firing patterns during interictal epileptiform discharges in the human cortex. *Brain J. Neurol.* 133, 1668–1681. doi:10.1093/brain/awq112
- Kellis, S., Miller, K., Thomson, K., Brown, R., House, P., Greger, B., 2010. Decoding spoken words using local field potentials recorded from the cortical surface. *J. Neural Eng.* 7, 056007. doi:10.1088/1741-2560/7/5/056007
- Kellis, S., Sorensen, L., Darvas, F., Sayres, C., O'Neill III, K., Brown, R.B., House, P., Ojemann, J., Greger, B., n.d. Multi-scale analysis of neural activity in humans: Implications for micro-scale electrocorticography. *Clin. Neurophysiol.* doi:10.1016/j.clinph.2015.06.002
- Kelly, R.C., Smith, M.A., Samonds, J.M., Kohn, A., Bonds, A.B., Movshon, J.A., Lee, T.S., 2007. Comparison of Recordings from Microelectrode Arrays and Single Electrodes in the Visual Cortex. *J. Neurosci.* 27, 261–264.
doi:10.1523/JNEUROSCI.4906-06.2007
- Khodagholy, D., Gelinas, J.N., Thesen, T., Doyle, W., Devinsky, O., Malliaras, G.G., Buzsáki, G., 2015. NeuroGrid: recording action potentials from the surface of the brain. *Nat. Neurosci.* 18, 310–315. doi:10.1038/nn.3905
- Khursheed, F., Tandon, N., Tertel, K., Pieters, T.A., Disano, M.A., Ellmore, T.M., 2011. Frequency-specific electrocorticographic correlates of working memory

- delay period fMRI activity. *Neuroimage* 56, 1773–82.
doi:10.1016/j.neuroimage.2011.02.062
- Krauss, G.L., Fisher, R., Plate, C., Hart, J., Uematsu, S., Gordon, B., Lesser, R.P., 1996. Cognitive effects of resecting basal temporal language areas. *Epilepsia* 37, 476–83.
- Krusienski, D.J., Sellers, E.W., McFarland, D.J., Vaughan, T.M., Wolpaw, J.R., 2008. Toward enhanced P300 speller performance. *J. Neurosci. Methods, Brain-Computer Interfaces (BCIs)* 167, 15–21. doi:10.1016/j.jneumeth.2007.07.017
- Kubaneck, J., Miller, K.J., Ojemann, J.G., Wolpaw, J.R., Schalk, G., 2009. Decoding flexion of individual fingers using electrocorticographic signals in humans. *J Neural Eng* 6, 66001. doi:10.1088/1741-2560/6/6/066001
- Kuiken, T.A., Dumanian, G.A., Lipschutz, R.D., Miller, L.A., Stubblefield, K.A., 2004. The use of targeted muscle reinnervation for improved myoelectric prosthesis control in a bilateral shoulder disarticulation amputee. *Prosthet. Orthot. Int.* 28, 245–253. doi:10.3109/03093640409167756
- Kuś, R., Duszyk, A., Milanowski, P., Łabęcki, M., Bierzyńska, M., Radzikowska, Z., Michalska, M., Żygierewicz, J., Suffczyński, P., Durka, P.J., 2013. On the Quantification of SSVEP Frequency Responses in Human EEG in Realistic BCI Conditions. *PLoS ONE* 8, e77536. doi:10.1371/journal.pone.0077536
- Lachaux, J.P., Axmacher, N., Mormann, F., Halgren, E., Crone, N.E., 2012. High-frequency neural activity and human cognition: past, present and possible future of intracranial EEG research. *Prog. Neurobiol.* 98, 279–301.
doi:10.1016/j.pneurobio.2012.06.008

- Lachaux, J.P., Fonlupt, P., Kahane, P., Minotti, L., Hoffmann, D., Bertrand, O., Baciau, M., 2007a. Relationship between task-related gamma oscillations and BOLD signal: New insights from combined fMRI and intracranial EEG. *Hum Brain Mapp.* doi:10.1002/hbm.20352
- Lachaux, J.P., Jerbi, K., Bertrand, O., Minotti, L., Hoffmann, D., Schoendorff, B., Kahane, P., 2007b. A Blueprint for Real-Time Functional Mapping via Human Intracranial Recordings. *PLoS ONE* 2, e1094.
- Lesser, R., Gordon, B., Uematsu, S., 1994. Electrical stimulation and language. *J. Clin. Neurophysiol.* 11, 191–204.
- Lesser, R.P., Luders, H., Klem, G., Dinner, D.S., Morris, H.H., Hahn, J., 1985. Ipsilateral trigeminal sensory responses to cortical stimulation by subdural electrodes. *Neurology* 35, 1760–1763.
- Lesser, R.P., Lüders, H., Klem, G., Dinner, D.S., Morris, H.H., Hahn, J., 1984. Cortical afterdischarge and functional response thresholds: results of extraoperative testing. *Epilepsia* 25, 615–621.
- Leuthardt, E.C., Schalk, G., Moran, D., Ojemann, J.G., 2006. The emerging world of motor neuroprosthetics: a neurosurgical perspective. *Neurosurgery* 59, 1–14; discussion 1–14. doi:10.1227/01.NEU.0000221506.06947.AC
- Leuthardt, E.C., Schalk, G., Wolpaw, J.R., Ojemann, J.G., Moran, D.W., 2004. A brain-computer interface using electrocorticographic signals in humans. *J Neural Eng* 1, 63–71. doi:10.1088/1741-2560/1/2/001
- Liu, J., Newsome, W.T., 2006. Local field potential in cortical area MT: stimulus tuning and behavioral correlations. *J Neurosci* 26, 7779–90.

- London, B.M., Jordan, L.R., Jackson, C.R., Miller, L.E., 2008. Electrical Stimulation of the Proprioceptive Cortex (Area 3a) Used to Instruct a Behaving Monkey. *IEEE Trans. Neural Syst. Rehabil. Eng. Publ. IEEE Eng. Med. Biol. Soc.* 16, 32–36. doi:10.1109/TNSRE.2007.907544
- Luders, H., Lesser, R.P., Hahn, J., Dinner, D.S., Morris, H., Resor, S., Harrison, M., 1986. Basal temporal language area demonstrated by electrical stimulation. *Neurology* 36, 505–10.
- Maldjian, J.A., Gottschalk, A., Patel, R.S., Detre, J.A., Alsop, D.C., 1999. The Sensory Somatotopic Map of the Human Hand Demonstrated at 4 Tesla. *NeuroImage* 10, 55–62. doi:10.1006/nimg.1999.0448
- Manning, J.R., Jacobs, J., Fried, I., Kahana, M.J., 2009. Broadband shifts in local field potential power spectra are correlated with single-neuron spiking in humans. *J Neurosci* 29, 13613–20.
- Martuzzi, R., van der Zwaag, W., Farthouat, J., Gruetter, R., Blanke, O., 2014. Human finger somatotopy in areas 3b, 1, and 2: a 7T fMRI study using a natural stimulus. *Hum. Brain Mapp.* 35, 213–226. doi:10.1002/hbm.22172
- Matsumoto, R., Nair, D.R., LaPresto, E., Bingaman, W., Shibasaki, H., Luders, H.O., 2007. Functional connectivity in human cortical motor system: a cortico-cortical evoked potential study. *Brain* 130, 181–97. doi:10.1093/brain/awl257
- Matsumoto, R., Nair, D.R., LaPresto, E., Najm, I., Bingaman, W., Shibasaki, H., Luders, H.O., 2004. Functional connectivity in the human language system: a cortico-cortical evoked potential study. *Brain* 127, 2316–30.

- Matsuzaki, N., Juhász, C., Asano, E., 2013. Cortico-cortical evoked potentials and stimulation-elicited gamma activity preferentially propagate from lower- to higher-order visual areas. *Clin. Neurophysiol.* 124, 1290–1296.
doi:10.1016/j.clinph.2013.02.007
- McFarland, D.J., McCane, L.M., David, S.V., Wolpaw, J.R., 1997. Spatial filter selection for EEG-based communication. *Electroencephalogr Clin Neurophysiol* 103, 386–94.
- McFarland, D.J., Sarnacki, W.A., Wolpaw, J.R., 2010. Electroencephalographic (EEG) control of three-dimensional movement. *J. Neural Eng.* 7, 036007.
doi:10.1088/1741-2560/7/3/036007
- McMullen, D., Hotson, G., Katyal, K., Wester, B., Fifer, M., McGee, T., Harris, A., Johannes, M., Vogelstein, R.J., Ravitz, A., Anderson, W., Thakor, N., Crone, N., 2014. Demonstration of a Semi-Autonomous Hybrid Brain-Machine Interface using Human Intracranial EEG, Eye Tracking, and Computer Vision to Control a Robotic Upper Limb Prosthetic. *IEEE Trans. Neural Syst. Rehabil. Eng.* Early Access Online. doi:10.1109/TNSRE.2013.2294685
- McNemar, Q., 1947. Note on the sampling error of the difference between correlated proportions or percentages. *Psychometrika* 12, 153–157.
doi:10.1007/BF02295996
- Mehring, C., Rickert, J., Vaadia, E., de Oliveira, S.C., Aertsen, A., Rotter, S., 2003. Inference of hand movements from local field potentials in monkey motor cortex. *Nat. Neurosci.* 6, 1253–1254. doi:10.1038/nn1158

- Mercanzini, A., Colin, P., Bensadoun, J.-C., Bertsch, A., Renaud, P., 2009. In vivo electrical impedance spectroscopy of tissue reaction to microelectrode arrays. *IEEE Trans. Biomed. Eng.* 56, 1909–1918.
doi:10.1109/TBME.2009.2018457
- Mesgarani, N., Chang, E.F., 2012. Selective cortical representation of attended speaker in multi-talker speech perception. *Nature* 485, 233–236.
doi:10.1038/nature11020
- Mesgarani, N., Cheung, C., Johnson, K., Chang, E.F., 2014. Phonetic Feature Encoding in Human Superior Temporal Gyrus. *Science* 343, 1006–1010.
doi:10.1126/science.1245994
- Meshulam, M., Ramot, M., Harel, M., Kipervasser, S., Andelman, F., Neufeld, M.Y., Kramer, U., Fried, I., Malach, R., 2013. Selectivity of audiovisual ECoG responses revealed under naturalistic stimuli in the human cortex. *J. Neurophysiol.* 109, 2272–2281. doi:10.1152/jn.00474.2012
- Mesulam, M.M., 1990. Large-scale neurocognitive networks and distributed processing for attention, language, and memory. *Ann. Neurol.* 28, 597–613.
- Miller, K.J., denNijs, M., Shenoy, P., Miller, J.W., Rao, R.P., Ojemann, J.G., 2007a. Real-time functional brain mapping using electrocorticography. *Neuroimage* 37, 504–7. doi:10.1016/j.neuroimage.2007.05.029
- Miller, K.J., Hermes, D., Honey, C.J., Hebb, A.O., Ramsey, N.F., Knight, R.T., Ojemann, J.G., Fetz, E.E., 2012. Human Motor Cortical Activity Is Selectively Phase-Entrained on Underlying Rhythms. *PLoS Comput Biol* 8, e1002655.
doi:10.1371/journal.pcbi.1002655

- Miller, K.J., Leuthardt, E.C., Schalk, G., Rao, R.P., Anderson, N.R., Moran, D.W., Miller, J.W., Ojemann, J.G., 2007b. Spectral changes in cortical surface potentials during motor movement. *J Neurosci* 27, 2424–32.
doi:10.1523/JNEUROSCI.3886-06.2007
- Miller, K.J., Schalk, G., Fetz, E.E., Nijs, M. den, Ojemann, J.G., Rao, R.P.N., 2010. Cortical activity during motor execution, motor imagery, and imagery-based online feedback. *Proc. Natl. Acad. Sci.* 200913697. doi:10.1073/pnas.0913697107
- Miller, K.J., Zanos, S., Fetz, E.E., den Nijs, M., Ojemann, J.G., 2009. Decoupling the cortical power spectrum reveals real-time representation of individual finger movements in humans. *J Neurosci* 29, 3132–7.
- Mollazadeh, M., Aggarwal, V., Davidson, A.G., Law, A.J., Thakor, N.V., Schieber, M.H., 2011. Spatiotemporal Variation of Multiple Neurophysiological Signals in the Primary Motor Cortex during Dexterous Reach-to-Grasp Movements. *J. Neurosci.* 31, 15531–15543. doi:10.1523/JNEUROSCI.2999-11.2011
- Mountcastle, V.B., 1997. The columnar organization of the neocortex. *Brain J. Neurol.* 120 (Pt 4), 701–722.
- Mountcastle, V.B., 1957. Modality and topographic properties of single neurons of cat's somatic sensory cortex. *J. Neurophysiol.* 20, 408–434.
- Narayanan, N.S., Kimchi, E.Y., Laubach, M., 2005. Redundancy and synergy of neuronal ensembles in motor cortex. *J. Neurosci. Off. J. Soc. Neurosci.* 25, 4207–4216. doi:10.1523/JNEUROSCI.4697-04.2005

- Nelson, A.J., Chen, R., 2008. Digit Somatotopy within Cortical Areas of the Postcentral Gyrus in Humans. *Cereb. Cortex* 18, 2341–2351.
doi:10.1093/cercor/bhm257
- Neuper, C., Pfurtscheller, G., 2001. Event-related dynamics of cortical rhythms: frequency-specific features and functional correlates. *Int. J. Psychophysiol., Thalamo-Cortical Relationships* 43, 41–58. doi:10.1016/S0167-8760(01)00178-7
- Nii, Y., Uematsu, S., Lesser, R.P., Gordon, B., 1996. Does the central sulcus divide motor and sensory functions? Cortical mapping of human hand areas as revealed by electrical stimulation through subdural grid electrodes. *Neurology* 46, 360–367.
- Nobre, A.C., Allison, T., McCarthy, G., 1994. Word recognition in the human inferior temporal lobe. *Nature* 372, 260–263.
- Nourski, K.V., Howard III, M.A., 2015. Chapter 13 - Invasive recordings in the human auditory cortex, in: Michael J. Aminoff, F.B. and D.F.S. (Ed.), *Handbook of Clinical Neurology, The Human Auditory System Fundamental Organization and Clinical Disorders*. Elsevier, pp. 225–244.
- O'Doherty, J.E., Lebedev, M.A., Ifft, P.J., Zhuang, K.Z., Shokur, S., Bleuler, H., Nicolelis, M.A.L., 2011. Active tactile exploration using a brain-machine-brain interface. *Nature* 479, 228–231. doi:10.1038/nature10489
- Ojemann, G., Ojemann, J., Lettich, E., Berger, M., 1989. Cortical language localization in left, dominant hemisphere. An electrical stimulation mapping investigation in 117 patients. *J Neurosurg* 71, 316–26. doi:10.3171/jns.1989.71.3.0316

- Pasley, B., Freeman, R., 2008. Neurovascular coupling. *Scholarpedia* 3, 5340.
doi:10.4249/scholarpedia.5340
- Pasley, B.N., David, S.V., Mesgarani, N., Flinker, A., Shamma, S.A., Crone, N.E., Knight, R.T., Chang, E.F., 2012. Reconstructing speech from human auditory cortex. *PLoS Biol.* 10, e1001251. doi:10.1371/journal.pbio.1001251
- Penfield, W., Boldrey, E., 1937. Somatic Motor and Sensory Representation in the Cerebral Cortex of Man as Studied by Electrical Stimulation. *Brain* 60, 389–443. doi:10.1093/brain/60.4.389
- Penfield, W., Jasper, H., 1954. *Epilepsy and the functional anatomy of the human brain*, 1st ed. Little, Brown, and Company, Boston.
- Pesaran, B., Pezaris, J.S., Sahani, M., Mitra, P.P., Andersen, R.A., 2002. Temporal structure in neuronal activity during working memory in macaque parietal cortex. *Nat Neurosci* 5, 805–11.
- Pfurtscheller, G., Cooper, R., 1975. Frequency dependence of the transmission of the EEG from cortex to scalp. *Electroencephalogr. Clin. Neurophysiol.* 38, 93–96.
- Pfurtscheller, G., Lopes da Silva, F.H., 1999a. Event-related EEG/MEG synchronization and desynchronization: basic principles. *Clin. Neurophysiol.* 110, 1842–1857. doi:10.1016/S1388-2457(99)00141-8
- Pfurtscheller, G., Lopes da Silva, F.H., 1999b. Functional meaning of event-related desynchronization (ERD) and synchronization (ERS), in: Pfurtscheller, G., Lopes da Silva, F.H. (Eds.), *Event-Related Desynchronization, Handbook of Electroencephalography and Clinical Neurophysiology*. Elsevier Science, pp. 51–65.

- Pistohl, T., Ball, T., Schulze-Bonhage, A., Aertsen, A., Mehring, C., 2008. Prediction of arm movement trajectories from ECoG-recordings in humans. *J. Neurosci. Methods, Brain-Computer Interfaces (BCIs)* 167, 105–114.
doi:10.1016/j.jneumeth.2007.10.001
- Pistohl, T., Schmidt, T.S.B., Ball, T., Schulze-Bonhage, A., Aertsen, A., Mehring, C., 2013. Grasp Detection from Human ECoG during Natural Reach-to-Grasp Movements. *PLoS ONE* 8, e54658. doi:10.1371/journal.pone.0054658
- Pistohl, T., Schulze-Bonhage, A., Aertsen, A., Mehring, C., Ball, T., 2012. Decoding natural grasp types from human ECoG. *NeuroImage* 59, 248–260.
doi:10.1016/j.neuroimage.2011.06.084
- Pouratian, N., Cannestra, A.F., Bookheimer, S.Y., Martin, N.A., Toga, A.W., 2004. Variability of intraoperative electrocortical stimulation mapping parameters across and within individuals. *J. Neurosurg.* 101, 458–466.
doi:10.3171/jns.2004.101.3.0458
- Powell, T.P., Mountcastle, V.B., 1959. Some aspects of the functional organization of the cortex of the postcentral gyrus of the monkey: a correlation of findings obtained in a single unit analysis with cytoarchitecture. *Bull. Johns Hopkins Hosp.* 105, 133–162.
- Price, C.J., 2000. The anatomy of language: contributions from functional neuroimaging. *J Anat* 197 Pt 3, 335–59.
- Rangarajan, V., Hermes, D., Foster, B.L., Weiner, K.S., Jacques, C., Grill-Spector, K., Parvizi, J., 2014. Electrical stimulation of the left and right human fusiform

- gyrus causes different effects in conscious face perception. *J. Neurosci. Off. J. Soc. Neurosci.* 34, 12828–12836. doi:10.1523/JNEUROSCI.0527-14.2014
- Rasmussen, T., Milner, B., 1977. The role of early left brain injury in determining lateralization of cerebral functions. *Ann. N. Y. Acad. Sci.* 299, 355–369.
- Ray, S., Crone, N.E., Niebur, E., Franaszczuk, P.J., Hsiao, S.S., 2008a. Neural correlates of high-gamma oscillations (60-200 Hz) in macaque local field potentials and their potential implications in electrocorticography. *J Neurosci* 28, 11526–11536.
- Ray, S., Maunsell, J.H., 2011. Different origins of gamma rhythm and high-gamma activity in macaque visual cortex. *PLoS Biol* 9, e1000610. doi:10.1371/journal.pbio.1000610
- Ray, S., Niebur, E., Hsiao, S.S., Sinai, A., Crone, N.E., 2008b. High-frequency gamma activity (80-150Hz) is increased in human cortex during selective attention. *Clin Neurophysiol* 119, 116–33.
- Resnik, L., Klinger, S.L., Etter, K., 2014. The DEKA Arm: Its features, functionality, and evolution during the Veterans Affairs Study to optimize the DEKA Arm. *Prosthet. Orthot. Int.* 38, 492–504. doi:10.1177/0309364613506913
- Rizzolatti, G., Luppino, G., Matelli, M., 1998. The organization of the cortical motor system: new concepts. *Electroencephalogr. Clin. Neurophysiol.* 106, 283–296. doi:10.1016/S0013-4694(98)00022-4
- Rouse, A.G., Williams, J.J., Wheeler, J.J., Moran, D.W., 2013. Cortical Adaptation to a Chronic Micro-Electrocorticographic Brain Computer Interface. *J. Neurosci.* 33, 1326–1330. doi:10.1523/JNEUROSCI.0271-12.2013

- Ruescher, J., Iljina, O., Altenmüller, D.-M., Aertsen, A., Schulze-Bonhage, A., Ball, T., 2013. Somatotopic mapping of natural upper- and lower-extremity movements and speech production with high gamma electrocorticography. *NeuroImage* 81, 164–177. doi:10.1016/j.neuroimage.2013.04.102
- Sanai, N., Mirzadeh, Z., Berger, M.S., 2008. Functional outcome after language mapping for glioma resection. *N Engl J Med* 358, 18–27. doi:10.1056/NEJMoa067819
- Schäffler, L., Lüders, H.O., Dinner, D.S., Lesser, R.P., Chelune, G.J., 1993. Comprehension deficits elicited by electrical stimulation of Broca's area. *Brain J. Neurol.* 116 (Pt 3), 695–715.
- Schalk, G., 2015. A general framework for dynamic cortical function: the function-through-biased-oscillations (FBO) hypothesis. *Front. Hum. Neurosci.* 9. doi:10.3389/fnhum.2015.00352
- Schalk, G., Kubanek, J., Miller, K.J., Anderson, N.R., Leuthardt, E.C., Ojemann, J.G., Limbrick, D., Moran, D., Gerhardt, L.A., Wolpaw, J.R., 2007. Decoding two-dimensional movement trajectories using electrocorticographic signals in humans. *J Neural Eng* 4, 264–75. doi:10.1088/1741-2560/4/3/012
- Schalk, G., Leuthardt, E.C., 2011. Brain-computer interfaces using electrocorticographic signals. *IEEE Rev. Biomed. Eng.* 4, 140–154. doi:10.1109/RBME.2011.2172408
- Schalk, G., Leuthardt, E.C., Brunner, P., Ojemann, J.G., Gerhardt, L.A., Wolpaw, J.R., 2008a. Real-time detection of event-related brain activity. *Neuroimage* 43, 245–9. doi:10.1016/j.neuroimage.2008.07.037

- Schalk, G., McFarland, D.J., Hinterberger, T., Birbaumer, N., Wolpaw, J.R., 2004. BCI2000: a general-purpose brain-computer interface (BCI) system. *IEEE Trans. Biomed. Eng.* 51, 1034–1043. doi:10.1109/TBME.2004.827072
- Schalk, G., Miller, K.J., Anderson, N.R., Wilson, J.A., Smyth, M.D., Ojemann, J.G., Moran, D.W., Wolpaw, J.R., Leuthardt, E.C., 2008b. Two-dimensional movement control using electrocorticographic signals in humans. *J Neural Eng* 5, 75–84. doi:10.1088/1741-2560/5/1/008
- Schevon, C.A., Ng, S.K., Cappell, J., Goodman, R.R., McKhann, G., Waziri, A., Branner, A., Sosunov, A., Schroeder, C.E., Emerson, R.G., 2008. Microphysiology of Epileptiform Activity in Human Neocortex. *J. Clin. Neurophysiol. Off. Publ. Am. Electroencephalogr. Soc.* 25, 321–330. doi:10.1097/WNP.0b013e31818e8010
- Schweizer, R., Voit, D., Frahm, J., 2008. Finger representations in human primary somatosensory cortex as revealed by high-resolution functional MRI of tactile stimulation. *NeuroImage* 42, 28–35. doi:10.1016/j.neuroimage.2008.04.184
- Shoham, D., Grinvald, A., 2001. The Cortical Representation of the Hand in Macaque and Human Area S-I: High Resolution Optical Imaging. *J. Neurosci.* 21, 6820–6835.
- Siero, J.C.W., Hermes, D., Hoogduin, H., Luijten, P.R., Ramsey, N.F., Petridou, N., 2014. BOLD matches neuronal activity at the mm scale: A combined 7 T fMRI and ECoG study in human sensorimotor cortex. *NeuroImage* 101, 177–184. doi:10.1016/j.neuroimage.2014.07.002

- Simeral, J.D., Kim, S.-P., Black, M.J., Donoghue, J.P., Hochberg, L.R., 2011. Neural control of cursor trajectory and click by a human with tetraplegia 1000 days after implant of an intracortical microelectrode array. *J. Neural Eng.* 8, 025027. doi:10.1088/1741-2560/8/2/025027
- Sinai, A., Bowers, C.W., Crainiceanu, C.M., Boatman, D., Gordon, B., Lesser, R.P., Lenz, F.A., Crone, N.E., 2005. Electrocorticographic high gamma activity versus electrical cortical stimulation mapping of naming. *Brain* 128, 1556–70. doi:10.1093/brain/awh491
- Slutzky, M.W., Jordan, L.R., Krieg, T., Chen, M., Mogul, D.J., Miller, L.E., 2010. Optimal spacing of surface electrode arrays for brain-machine interface applications. *J. Neural Eng.* 7, 26004. doi:10.1088/1741-2560/7/2/026004
- Suminski, A.J., Tkach, D.C., Fagg, A.H., Hatsopoulos, N.G., 2010. Incorporating Feedback from Multiple Sensory Modalities Enhances Brain–Machine Interface Control. *J. Neurosci.* 30, 16777–16787. doi:10.1523/JNEUROSCI.3967-10.2010
- Sun, F.T., Morrell, M.J., Wharen, R.E., Jr., 2008. Responsive cortical stimulation for the treatment of epilepsy. *Neurotherapeutics* 5, 68–74. doi:10.1016/j.nurt.2007.10.069
- Sutherling, W.W., Levesque, M.F., Baumgartner, C., 1992. Cortical sensory representation of the human hand Size of finger regions and nonoverlapping digit somatotopy. *Neurology* 42, 1020–1020. doi:10.1212/WNL.42.5.1020

- Tanji, K., Suzuki, K., Delorme, A., Shamoto, H., Nakasato, N., 2005. High-frequency gamma-band activity in the basal temporal cortex during picture-naming and lexical-decision tasks. *J Neurosci* 25, 3287–93.
- Tenore, F.V.G., Ramos, A., Fahmy, A., Acharya, S., Etienne-Cummings, R., Thakor, N.V., 2009. Decoding of Individuated Finger Movements Using Surface Electromyography. *IEEE Trans. Biomed. Eng.* 56, 1427–1434.
doi:10.1109/TBME.2008.2005485
- Thongpang, S., Richner, T.J., Brodnick, S.K., Schendel, A., Kim, J., Wilson, J.A., Hippensteel, J., Krugner-Higby, L., Moran, D., Ahmed, A.S., Neimann, D., Sillay, K., Williams, J.C., 2011. A micro-electrocorticography platform and deployment strategies for chronic BCI applications. *Clin. EEG Neurosci.* 42, 259–265.
- Trujillo-Ortiz, A., Hernandez-Walls, R., Castro-Perez, A., 2004. McNemarextest: McNemar's Exact Probability Test. [WWW Document]. URL http://www.mathworks.com/matlabcentral/fileexchange/file_infos/6297-mcnemarextest (accessed 4.16.15).
- Vansteensel, M.J., Bleichner, M.G., Dintzner, L.T., Aarnoutse, E.J., Leijten, F.S.S., Hermes, D., Ramsey, N.F., 2013. Task-free electrocorticography frequency mapping of the motor cortex. *Clin. Neurophysiol. Off. J. Int. Fed. Clin. Neurophysiol.* 124, 1169–1174. doi:10.1016/j.clinph.2012.08.048
- Van Westen, D., Fransson, P., Olsrud, J., Rosen, B., Lundborg, G., Larsson, E.M., 2004. Fingersomatotopy in area 3b: an fMRI-study. *BMC Neurosci* 5, 28.

- Velliste, M., Perel, S., Spalding, M.C., Whitford, A.S., Schwartz, A.B., 2008. Cortical control of a prosthetic arm for self-feeding. *Nature* 453, 1098–1101. doi:10.1038/nature06996
- Vinjamuri, R., Weber, D.J., Mao, Z.-H., Collinger, J.L., Degenhart, A.D., Kelly, J.W., Boninger, M.L., Tyler-Kabara, E.C., Wang, W., 2011. Toward synergy-based brain-machine interfaces. *IEEE Trans. Inf. Technol. Biomed. Publ. IEEE Eng. Med. Biol. Soc.* 15, 726–736. doi:10.1109/TITB.2011.2160272
- Viventi, J., Kim, D.H., Vigeland, L., Frechette, E.S., Blanco, J.A., Kim, Y.S., Avrin, A.E., Tiruvadi, V.R., Hwang, S.W., Vanleer, A.C., Wulsin, D.F., Davis, K., Gelber, C.E., Palmer, L., Van der Spiegel, J., Wu, J., Xiao, J., Huang, Y., Contreras, D., Rogers, J.A., Litt, B., 2011. Flexible, foldable, actively multiplexed, high-density electrode array for mapping brain activity in vivo. *Nat Neurosci* 14, 1599–605. doi:10.1038/nn.2973
- Wang, W., Collinger, J.L., Degenhart, A.D., Tyler-Kabara, E.C., Schwartz, A.B., Moran, D.W., Weber, D.J., Wodlinger, B., Vinjamuri, R.K., Ashmore, R.C., Kelly, J.W., Boninger, M.L., 2013. An Electrocorticographic Brain Interface in an Individual with Tetraplegia. *PLoS ONE* 8, e55344. doi:10.1371/journal.pone.0055344
- Williams, J.C., Rennaker, R.L., Kipke, D.R., 1999. Long-term neural recording characteristics of wire microelectrode arrays implanted in cerebral cortex. *Brain Res. Brain Res. Protoc.* 4, 303–313.
- Wodlinger, B., Downey, J.E., Tyler-Kabara, E.C., Schwartz, A.B., Boninger, M.L., Collinger, J.L., 2015. Ten-dimensional anthropomorphic arm control in a

- human brain-machine interface: difficulties, solutions, and limitations. *J. Neural Eng.* 12, 016011. doi:10.1088/1741-2560/12/1/016011
- Wolpaw, J.R., McFarland, D.J., 2004. Control of a two-dimensional movement signal by a noninvasive brain-computer interface in humans. *Proc. Natl. Acad. Sci. U. S. A.* 101, 17849–54.
- Wolpaw, J.R., McFarland, D.J., Neat, G.W., Forneris, C.A., 1991. An EEG-based brain-computer interface for cursor control. *Electroencephalogr. Clin. Neurophysiol.* 78, 252–259. doi:10.1016/0013-4694(91)90040-B
- Wood, C.C., Spencer, D.D., Allison, T., McCarthy, G., Williamson, P.D., Goff, W.R., 1988. Localization of human sensorimotor cortex during surgery by cortical surface recording of somatosensory evoked potentials. *J. Neurosurg.* 68, 99–111. doi:10.3171/jns.1988.68.1.0099
- Woolsey, C.N., Erickson, T.C., Gilson, W.E., 1979. Localization in somatic sensory and motor areas of human cerebral cortex as determined by direct recording of evoked potentials and electrical stimulation. *J. Neurosurg.* 51, 476–506. doi:10.3171/jns.1979.51.4.0476
- Woolsey, C.N., Marshall, W., Bard, P., 1942. Representation of cutaneous tactile sensibility in the cerebral cortex of the monkey as indicated by evoked potentials. *Bull Johns Hopkins Hosp* 70, 399–441.
- Worrell, G.A., Gardner, A.B., Stead, S.M., Hu, S., Goerss, S., Cascino, G.J., Meyer, F.B., Marsh, R., Litt, B., 2008. High-frequency oscillations in human temporal lobe: simultaneous microwire and clinical macroelectrode recordings. *Brain* 131, 928–37. doi:10.1093/brain/awn006

- Wu, M., Wisneski, K., Schalk, G., Sharma, M., Roland, J., Breshears, J., Gaona, C.,
Leuthardt, E.C., 2010. Electrocorticographic frequency alteration mapping for
extraoperative localization of speech cortex. *Neurosurgery* 66, E407–9.
doi:10.1227/01.NEU.0000345352.13696.6F
- Yanagisawa, T., Hirata, M., Saitoh, Y., Goto, T., Kishima, H., Fukuma, R., Yokoi, H.,
Kamitani, Y., Yoshimine, T., 2011. Real-time control of a prosthetic hand
using human electrocorticography signals. *J. Neurosurg.* 114, 1715–1722.
doi:10.3171/2011.1.JNS101421
- Yanagisawa, T., Hirata, M., Saitoh, Y., Kishima, H., Matsushita, K., Goto, T., Fukuma, R.,
Yokoi, H., Kamitani, Y., Yoshimine, T., 2012. Electrocorticographic control of a
prosthetic arm in paralyzed patients. *Ann. Neurol.* 71, 353–361.
doi:10.1002/ana.22613
- Zhuang, J., Truccolo, W., Vargas-Irwin, C., Donoghue, J.P., 2010. Decoding 3-D reach
and grasp kinematics from high-frequency local field potentials in primate
primary motor cortex. *IEEE Trans. Biomed. Eng.* 57, 1774–1784.
doi:10.1109/TBME.2010.2047015
- Ziegler-Graham, K., MacKenzie, E.J., Ephraim, P.L., Travison, T.G., Brookmeyer, R.,
2008. Estimating the Prevalence of Limb Loss in the United States: 2005 to
2050. *Arch. Phys. Med. Rehabil.* 89, 422–429.
doi:10.1016/j.apmr.2007.11.005

© 2012 IEEE. Reprinted, with permission, from Fifer, M.S., Acharya, S., Benz, H.L., Mollazadeh, M., Crone, N.E., Thakor, N.V., "Towards electrocorticographic control of a dexterous upper limb prosthesis." IEEE Pulse, vol. 3, no. 1, pp. 38-42, Jan. 2012.

© 2014 IEEE. Reprinted, with permission, from Fifer, M.S.*, Hotson, G.*, Wester, B., McMullen, D.P., Wang, Y., Johannes, M.S., Katyal, K.D., Helder, J.B., Para, M.P., Vogelstein, R.J., Anderson, W.S., Thakor, N.V., Crone, N.E., "Simultaneous neural control of simple reaching and grasping with the modular prosthetic limb using intracranial EEG." IEEE Transactions on Neural Systems and Rehabilitation Engineering, vol. 22, no. 3, pp. 695-705, May 2014.

In reference to IEEE copyrighted material which is used with permission in this thesis, the IEEE does not endorse any of Johns Hopkins University's products or services. Internal or personal use of this material is permitted. If interested in reprinting/republishing IEEE copyrighted material for advertising or promotional purposes or for creating new collective works for resale or redistribution, please go to http://www.ieee.org/publications_standards/publications/rights/rights_link.html to learn how to obtain a License from RightsLink.

Vita



Matthew Stephen Fifer was born in 1987 in Fairfax, Virginia. He went to high school at Thomas Jefferson High School for Science and Technology, where he began his studies in computer science and cultivated an interest in biomedical engineering. He received a National Merit Scholarship and a Rodman Scholarship to attend the University of Virginia, where he graduated in 2009 as a Bachelor of Science with High Distinction in biomedical engineering. During his time at the University of Virginia, he was selected as one of fifty four undergraduate students to live on the Lawn and was inducted to the Raven Society for exemplary academic achievement, leadership, and service to the University. Matthew matriculated into the Johns Hopkins University Biomedical Engineering Ph.D. program in 2009, where he began his research into brain-machine interface and functional mapping with human electrocorticography. He has been selected for Honorable Mention as a National Science Foundation Graduate Research Fellow in 2011. Additionally, he has twice been a member of a collaborative team spanning JHU and JHU/APL whose projects on (1) hybrid neural control of neuroprosthetics with electrocorticography, and (2) neural control of individual fingers of a neuroprosthetics have been selected as Finalists for the annual Brain-Computer Interface Research Award. At the time of this dissertation's submission, Matthew has been an author on five peer-reviewed journal publications, one book chapter,

eight conference papers, and over fifteen conference abstracts. He is also a co-inventor on one patent and one provisional patent.

In October 2015, Matthew will join the JHU Applied Physics Laboratory in the Research and Exploratory Development sector as a Senior Professional Staff researcher on the Applied Neuroscience team.